VISCOUS STREAMING-ENHANCED INERTIAL PARTICLE TRANSPORT

BY

TEJASWIN PARTHASARATHY

THESIS

Submitted in partial fulfillment of the requirements
for the degree of Master of Science in Mechanical Engineering
in the Graduate College of the
University of Illinois at Urbana-Champaign, 2018

Urbana, Illinois

Adviser:

Assistant Professor Mattia Gazzola

Abstract

Fluidic devices operating at the micro- and milli-meter scales employ several fundamental tasks involving pumping, mixing, separation, sorting, storing and transport of different fluids (or) species. An attractive fluid mechanism that can be leveraged to fulfill these wide range of tasks is viscous streaming, a non-linear effect characteristic of the scales above. In this thesis, we first show that numerical simulations based on the Remeshed Vortex Method (RVM) can accurately and efficiently capture viscous streaming dynamics. We test this algorithm on a wide variety of settings while simultaneously exhibiting the resultant streaming flow–structures, demonstrating both streaming's capability of effecting flow control and our solver's robustness in capturing these structures. We then consider the problem of an idealized two-dimensional inertial particle transport and prove that transport can be augmented by sensibly utilizing the streaming mechanism. We then successfully perform a forward–design study to devise shapes capable of enhanced transport using this mechanism, capitalizing on the insights gained from our demonstrations above. We envison such transport applications in the emergent technology of miniature robots, capable of traversing our blood stream to deliver payloads of therapeutical drugs.

Table of Contents

Chapter 1

Introduction

1.1 Micro-scale flows

Biologically relevant flows occur at a wide range of scales—from blood flowing in our body (μ to *milli* meter scales) [1] to warm ocean currents replenishing plankton population, thus driving food chains (*macro* scales) [2]. In recent years, the former has received considerable attention, attributed to our near-singular focus on understanding and subsequently mastering the human body. Indeed we employ micro-devices (tissues) to synthesize, analyze, pump and mix essential fluids and chemicals, which are housed within and transported via micro-channels (blood vessels and capillaries). It is then not surprising that researchers working in biology, bio–medicine and allied fields are looking for new pathways to engineer contraptions capable of mimicking and even enhancing the function of naturally occurring fluidic-devices, with equal emphasis placed on comprehending the underlying flow-physics.

The field of microfluidics (including micro- and milli- meter scales) has lent itself to the comprehension of such flows, as they provide an experimental platform to validate and extend theoretical analysis [3–7]. This has enabled better functional element designs for targeted biomedical applications, which in turn facilitates physical understanding. These applications range from chemical analysis and synthesis [8, 9]; assays for chemical, physical and biological testing [10] to understanding low Re bio-hydrodynamics [11–13] among many others. A crucial component in enabling such applications is our ability to perform certain fundamental, mechanical operations in an uncertain fluid environment. These include, but are not restricted to, transport, pumping, isolating, mixing and separating different fluids (e.g., water and air) or different species (e.g., reactive chemicals) [3, 4].

As it turns out, performing these operations is a difficult labor– and knowledge–intensive task. An inspection of literature [14, 15] reveals several works devoted to effecting and studying these operations, including pumping [16–19], mixing [20–22] and inertial particle manipulation [23–25] to name a few. The physics of scales, physics–dependent design and associated control contributes to this difficulty. Indeed at micrometer scales (e.g., in blood capillaries, with typical $l \sim 10^{-5}$m, $\nu \sim 10^{-6}$m^2/s, $U \sim 10^{-3}$m/s

[1]), the Reynolds number $Re \sim 0$, indicating viscosity-dominated creeping (Stokes)-flow regime. While characteristic linearity simplifies design, it also inhibits routes to chaos in this regime, which is quintessential to problems of transport and mixing [26, 27]. At millimeter scales (e.g., in blood vessels, with typical $l \sim 10^{-4} - 10^{-2}\text{m}$, $\nu \sim 10^{-6}\text{m}^2/\text{s}$, $U \sim 10^{-2} - 10^{-1}\text{m/s}$ [1]), finite Re ($\mathcal{O}(1) - \mathcal{O}(100)$) with '*weak*' non-linearity enables many applications, but the nexus between physics, design and control is now unknown, with the latter being especially difficult. In addition, the connected questions of device thoroughput, scalability and construction adds to this uncertainty. While there has been proofs of concept concerning multiple technologies for the aforementioned operations, it remains unclear whether one '*universal*' technique exists, let alone emerge. Exacerbating this problem is the widespread monolithic integrated systems approach of experimental micro-fluidic device prototyping which involves few or no modular components [28–30], leading to higher turnaround times for unit (module) and integrated (lab-on-a-chip) testing of these technologies.

The need then emerges for a consistent, accessible and scalable technology for such operations, which remains effective across orders of Re magnitude. A concomitant need is a computational framework for testing this technology, which can be embedded in an Analyze, Design, Optimize, Verify cycle quite akin to an experimental setup (an in-silico *lab* of sorts).

1.2 Challenges

1. To demonstrate such a fluid mechanism that is *effective* (performs the desired operations), *scalable* (both in operation and across physical scales), *accessible* (straightforward to setup and use), *integrable* in a given environment (potentially with other fluid effects) yet *controllable* and *robust*.

2. To establish a computational framework that can efficiently and accurately predict the dynamics of such fluid systems, including flow–structure and scalar transport effects, while possessing modularity to change and potentially *evolve* designs.

3. To adopt/co-develop another framework for interpreting and analyzing such flows, which can be integrated in the aforementioned design process.

1.3 This thesis

1. Establishes viscous streaming [20, 31–62] as a viable technique to achieve transport, mixing, etc. in a complicated, uncertain fluid–structure environment, with almost all the desirable properties highlighted earlier. As a proof of concept, we demonstrate that by utilizing streaming, we can carry and drop

passive inertial objects in the flow (*effective*) quite *precisely* and *robustly* across $Re \in \mathcal{O}(1) - \mathcal{O}(100)$ (*scalable*), despite the presence of other flow effects (*integrable*). This is enabled by ...

2. ... first substantiating Fluid–Structure Interaction (FSI) simulations based on Remeshed Vortex Method (RVM) as an effective and useful tool to simulate streaming dynamics. To this extent, we exhibit its *utility* by replicating and validating against standard viscous streaming single cylinder setups across different dynamical regimes (corresponding to low (Stokes–like) [48], intermediate [41, 46, 63] and high [39, 42] Re), against cases with multiple cylinders (*scaling up*) [49], against different shapes [53–55] and actuations [35, 37, 47, 64] (*designs*) and lastly across varied kinematic regimes (categorized as Keulegan-Carpenter (KC) flows [31, 65–71], closely related to streaming flows). We comprehend these flows by ...

3. ... a combination of physics- and data-based tools. These include relating the observations back to asymptotic theory, correlating and contrasting simulations of different dynamical setups, analyzing flow properties (velocity, streamfunction and particle trace fields), topology and finally mode decompositions of flow data.

Chapter 2

Viscous Streaming

Disclaimer : Parts of the text and figures in this chapter are taken, with permission, from private communications written by Prof. Mattia Gazzola, who retains credits and sole ownership.

In this chapter, we motivate the choice of viscous streaming for microfluidic flow control and detail the conclusions of prior works done in the field, while highlighting open questions. We also briefly review the literature for the closely–related KC flows, as it enables intriguing, yet potentially controllable dynamics for the parameter ranges that we are typically interested in.

2.1 Definition

A TL;DR definition of viscous streaming is "a fluid mechanism that takes place when an immersed body oscillates within specific size–frequency ratios, which is responsible for the emergence of characteristic rectified flows via non-linear fluid responses". More technically, it is a consequence of the non-linearity of Navier–Stokes (NS) equations and arises when a fluid of viscosity ν is driven periodically with frequency ω by a vibrating boundary of characteristic length R. The millimeter scale system of figure 2.1(h) demonstrates such a setup. It represents the flow pattern created by a cylinder of $R = 500\,\mu\text{m}$ oscillating at a frequency $f \sim 80\,\text{Hz}$ ($\omega \sim 500\,\text{rad}\,\text{s}^{-1}$) and scaled amplitude $\epsilon = A/R \sim 10^{-2}$, with characteristic velocity $U_\text{o} = \epsilon\omega R$. The induced velocity gradients largely occur within the Stokes layer of thickness $\delta \sim \sqrt{\nu/\omega} \sim 45\,\mu\text{m}$, so that δ is $\sim 10\%$ of R. Fluid momentum fluctuations within δ induce stresses that drive the flow well beyond this region. In this example, they give rise to two steady flow regions with characteristic eddies: inner '*cells*' (called the DC boundary layer) next to the cylinder and larger outer lobes (called the '*driven*' fluid). These eddies lie outside the Stokes layer and exhibit slow timescales (relative to oscillations) and closed streamlines. Thus, they partition the flow into *sealed* domains suitable for particle manipulations, mixing, etc.

Seeking descriptive dynamical parameters for this setup, one can deduce $R_\text{o} = U_\text{o}R/\nu = \epsilon\omega R^2/\nu$, termed the oscillatory Reynolds number and $R_\text{s} = U_\text{o}^2/\omega\nu = \epsilon^2\omega R^2/\nu$, the streaming Reynolds number. While the

former represents oscillatory–flow dynamics, the latter signifies streaming–flow dynamics, i.e. R_s is a proxy for the measure of inertial and viscous forces in the *streaming* field. Only if both these parameters are held constant, the flow behavior is preserved. These parameters are coupled via the relation $R_s = \epsilon R_o$ and retains meaning only for small ϵ. This is attributed to the discriminatory nature of the ϵ parameter—low amplitude ($\epsilon \lessapprox 0.2$) flows are categorized as streaming flows (for which $R_o - R_s$ meaningfully acts as a scaling parameter pair) while KC flows have high ($\epsilon \gtrapprox 0.2$) amplitudes (for which a different KC $- \beta$ [72] scaling parameter pair is used, elaborated at the end of this section). The smallness of ϵ also gives streaming its characteristic features—it is a second-order effect (with typical velocities $\sim \epsilon^2 \omega R$ being an order of magnitude smaller than the corresponding oscillatory flow), with no flow separation and thus amenable to analytical treatment and better flow controllability (at least from a dynamics perspective).

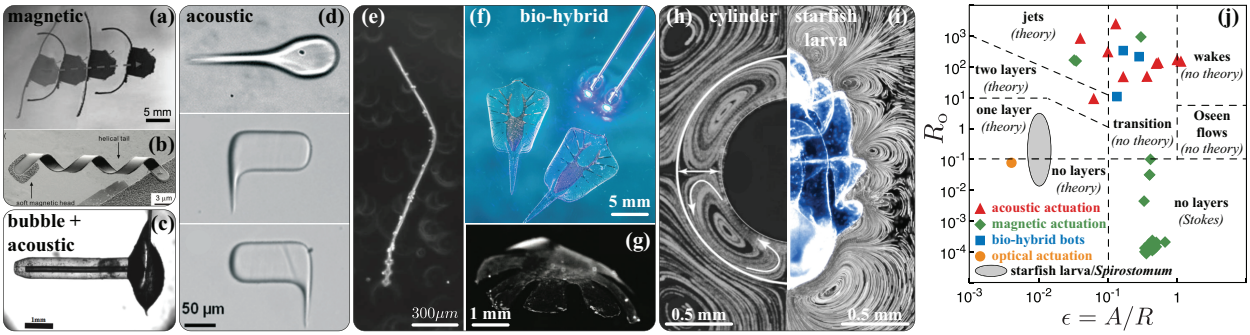

Figure 2.1: *(a,b)* Magnetically [73, 74], *(c)* bubble [75], *(d)* acoustically [76] powered bots; *(e,f,g)* Swimming biobots [77–79]: flagella, ray, jellyfish; *(h)* Oscillating cylinder steady streaming [46]; *(i)* Starfish larva flow [80, 81]; *(j)* Swimming robots represented on the cylinder-streaming phase space, as adapted from [38, 50]. The regimes (bolded) are named after its most distinguishing flow–feature.

2.2 Motivation

The choice of utilizing viscous streaming for flow manipulation stems for a variety of considerations. In some sense, streaming is a result of a *fundamental* kinematic component involving a body immersed in a fluid—*oscillations*. This reflects in all its desirable (and even undesirable) features. Firstly, it has been proven *effective* in the past for problems of micropumping [19, 82], micromixing [83, 84], particle sorting and cytometry [25, 61], particle transport [47, 57, 59, 85–88] among others. Furthermore, as seen earlier, if R_o and R_s are held constant, the flow behavior is preserved. This implies that a streaming system can be miniaturized by increasing ω. Since engineering devices can access high frequencies (10^6 Hz), the system of figure 2.1(h) can be scaled down to microns, offering compelling micro-flow control options. It can then be effectively used in systems ranging from microns to millimeters, across a wide frequency range of

$\sim 10\,\text{Hz} - 10^6\,\text{Hz}$, transcending various dynamical regimes [32–37, 39–43, 45–48, 50, 51, 89–92].

Apart from this *dynamic scalability*, the scalability in terms of *multitudes* of streaming devices have been demonstrated in the past, theoretically (albeit in a limited sense) [32, 41, 93–96], computationally [51, 97, 98] and experimentally [20, 49, 58, 62, 84, 99]. The scalability in such experiments rely on the *accessible* nature of streaming—the presence of some oscillatory kinematics (be it a minimal setup involving an oscillatory flow past a static object [46–49] or bodies oscillating in a quiscient flow [35, 37, 40, 51]) guarantees streaming. We note that oscillations need not be restricted to translations alone—torsions and even squirming (a locomotory pathway of small organisms involving prescribed slip on the organism surface) can generate streaming (we expand on this in a later section). A plausible *biological* example are ciliated squirming organisms, such as Spirostomum [56] or starfish larvae [80] (figure 2.1(i)), which have been shown to be able to switch between different functions [80] (propulsion/feeding) by modulating surrounding fluid. Their length/time scales are compatible with streaming and it is not farfetched to think that they might harness these flows to locomote or entrain nutrients. One can then think of a biologically-inspired engineered-swimmer (figure 2.1(a-g)), similar in scales to these micro-organisms, that can potentially utilize similar streaming flows for enhancing applications such as drug-delivery, in-situ analysis and surgery or enabling new ones. Indeed, in the past few years there has been an accelerated pace of development of artificial and bio–hybrid [77–79, 100] mini-robots that operate in a streaming regime (seen in the phase diagram figure 2.1(h)), bringing within reach such high-impact applications in medicine and manufacturing.

Viscous streaming is then a sensible choice for flow and particle control. Thus, it is not surprising that considerable work has been done till date in understanding streaming flows, both from a physical and applied perspective.

2.3 Literature for two–dimensional viscous streaming flows

We start by reviewing prior works on viscous streaming from a linearly oscillating circular cylinder; from a circular cylinder undergoing other actuations (translational/torsional oscillations, squirming or a combination thereof); from a cylinder of different shape (triangle, square, etc.); and systems comprising multiple cylinders. Before this discussion, a clarification on the different definitions (viscous, acoustic and microbubble streaming) seen in literature proves useful for avoiding confusion. *Viscous streaming* (the focus of this work) is set up by vorticity generated from a solid body in an oscillatory flow field. *Acoustic streaming* is setup by acoustic waves (isentropic pressure waves) either undergoing finite damping due to fluid viscosity (quartz wind) or interacting with a solid body, quite akin to viscous streaming. *Microbubble streaming* is

generated by oscillating a bubble (with forces/stress balanced on its contact surface with the fluid, rather than the velocity) inside a fluid, usually by acoustic means. It is imperative to state that all of them manifest as a *similar* non-linear effect in the fluid, over long length and time scales.

2.3.1 Viscous streaming from a single, isolated, oscillating circular cylinder

Viscous streaming was reportedly discovered by Faraday [101] almost 200 years ago, in 1831. The first reasonable explanation for this phenomenon was given 50 years later in 1883 by Rayleigh [102], who demonstrated streaming of dust particles due to Kundt-tube oscillations. It was re-investigated almost 50 years later using experiments and theory by Schlichting [103] (who used an asymptotic theory in the Stokes limit) and Andrade [104], among some others. They noticed a discrepancy in the direction of streaming close to the cylinder which was later attributed to the differences in the dynamical range corresponding to their respective experiments (at this point of time, the $R_o - R_s$ set was not discovered). This prompted the first serious (and almost complete) theoretical investigation by Holtsmark et al. [32] (and later improved by Raney et al. [33], Skavlem and Tjötta [34], and Bertelsen et al. [41], who included additional terms in the asymptotic expansion as well as the Stokes drift correction for obtaining steady Lagrangian streamlines—see section 3.1.3). They treated the entire flow (unsteady & steady, across all *layers*, seen in figure 2.2, which will be made clear in the next paragraph) progressively at all orders via an asymptotic expansion in ϵ, using the method of *successive approximations* (also known as Picard iterations), with their results valid for Stokes–like flows (formally only for $R_o \ll 1$, but also works for $R_s \lessapprox 1$ as proved later [37, 41]). The interpretation of streaming as being driven by *Reynolds–stress like* terms within the Stokes layer (also called AC boundary layer) can be first attributed to this seminal work.

This interpretation was made more rigorous when the R_s parameter (streaming Reynolds number) was introduced by Stuart [36] who also suggested the existence of a *double boundary layer* structure for $R_s \gg 1$. That is, while the oscillatory–flow adjusts itself to match the solid body velocity in the AC boundary layer, so does the steady streaming flow over what is called the *DC boundary layer*, which is the second layer in Stuart's theory. He also suggested the importance of shape curvature in streaming, across specific dynamical regimes; and of a *local* Reynolds number in the dynamics and analysis of such flows using laminar theory. He hinted that an increase in R_s will eventually lead to the *collision* of double boundary layers, necessitated by the physicality of flow fields. His double boundary layer proposal was corroborated independently by Riley [35], who used a method of matched asymptotic analysis, where the *inner* (AC boundary layer, figure 2.2) and *outer* (the complementary region, figure 2.2) solutions are treated separately (with respective scaling and asymptotic expansion parameters) and are only coupled via the boundary conditions. We add that an

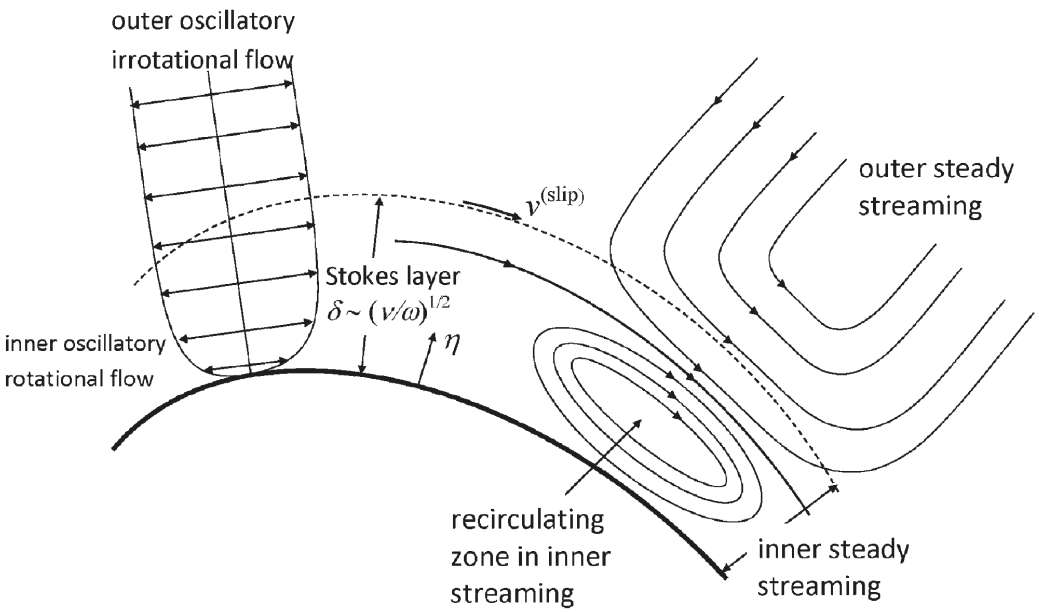

Figure 2.2: An illustration describing viscous streaming initiation. Within the Stokes layer, the leading order oscillatory flow generates vorticity. The body oscillations generating this vorticity set in motion a non-linear fluid response (the motion in the first half *pushes* the fluid in one direction, while in the second half the same fluid is *sucked* in to occupy space, leading to asymmetries), which generates (via vorticity) a recirculation residing over long time scales in this Stokes layer, called *inner* streaming. This recirculation constrains (via a slip velocity $v^{(\mathrm{slip})}$ kinematically, and a Reynolds–stress like term dynamically) the fluid outside the Stokes layer to undergo a circulatory motion, which is called *outer* streaming. Based on the dynamic $R_\mathrm{o} - R_\mathrm{s}$ regime, we perceive the *inner* and *outer* streaming in different ways, shown in figure 2.3. Figure adapted from Sadhal [105].

important scaling/asymptotic expansion parameter that Riley (and many others) employs is the Womerseley number $\alpha = R\sqrt{\omega/\nu}$ which indicates the extent of the AC layer compared to the dimensions of the body. In [37] he extended this analysis to all dynamical regimes, to what we now call *no-layer* ($R_\mathrm{o} \ll 1$), *one-layer* ($R_\mathrm{s} \ll 1$) and *two-layer* ($R_\mathrm{s} > \mathcal{O}(1)$) limits, as explained in figure 2.3. He concluded that $R_\mathrm{s} \ll 1$ is a necessary and sufficient condition for the *outer* flow to exhibit Stokes–like behavior. This grouped the no-layer and one-layer approximations together, extending the region of applicability of the Holtsmark et al. [32] theory. Another conclusion of [37] is that for $R_\mathrm{s} \sim \mathcal{O}(1)$, the non-linear dynamics necessitate that the complete Navier–Stokes equations be solved. Almost immediately after, Wang [38] used a similar matched asymptotic analysis and reworked the Holtsmark theory. He confirmed Riley's regime of validity of the Holtsmark solution and Riley's conclusion that the complete Navier–Stokes equation needs to be solved in the $R_\mathrm{s} \sim \mathcal{O}(1)$ regime. He also draws attention to the potential importance of curvature terms in certain dynamical regimes, although it was (and still remains) irresolvable by lower-order boundary layer theory.

Davidson and Riley [39] then came up with a semi–numerical theory addressing the $R_\mathrm{s} \gg \mathcal{O}(1)$ regime

and confirmed Stuart's prior analysis on boundary layer collision. The collision results in a *jet* erupting along the oscillation axis, which they showed numerically and experimentally to match a planar Bickley [106] jet solution. Bertelsen et al. [41] corrected Holtsmark's theory and showed that the region of validity of the corrected Holtsmark theory can be extended to $R_s \lessapprox 1$. They also exhibited the non-linear dependence of the DC boundary layer thickness δ_{dc} on the AC boundary layer thickness δ_{ac}, which we later use as a means of validation of our numerical solver. They extended their investigations to the jetting regime in [42], wherein they noticed wide discrepancies between their experiments and the theory of [39]. Riley [40] then proposed an matched asymptotic solution based on second-order boundary layer theory to include finite Reynolds number effects in an attempt to substantiate theory with Bertelsen's experimental observations. But discrepancies were still observed, quoted as being finite boundary effects. Haddon and Riley [107] discretized and numerically solved the analytical equation of [40] in a venture to corroborate this fact. While the difference between experiments and analytics/numerics was reduced, they did not completely agree with one another, probably due to experimental measurement errors and finite boundary effects. For the next 10 years the origin and nature of this jet was the subject of much scrutiny [43, 108], along with cylinders undergoing other actuations, which we discuss next.

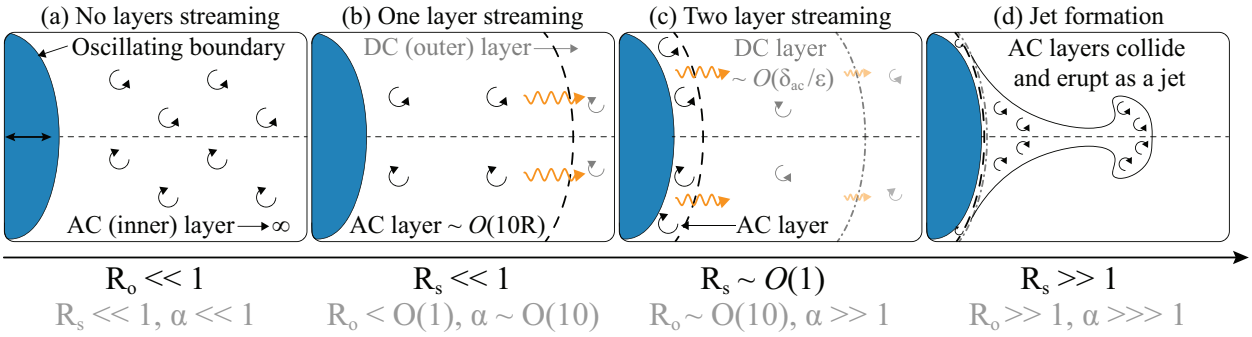

Figure 2.3: Illustration of the manifestation of streaming in different dynamical parameter regimes (the necessary parameter constraint is indicated by black text, using which we derive the parameters in grey text). For *(a)* $R_o \ll 1$, the leading order oscillatory flow is Stokesian and the effect of the body (via the AC/inner layer) is felt at long (infinite) distances. This is called *no-layer* streaming as no distinct regions are perceivable. *(b)* represents the case of $R_s \ll 1$, with a Stokesian streaming, but with the oscillatory flow having finite inertia effects. In this case, the AC boundary layer thickness is comparable to the body dimensions and hence is finite/perceivable. The outer layer, being Stokesian, is infinite for practical purposes. This is the *one-layer* regime. Upon increasing R_s further to $\sim \mathcal{O}(1)$ as shown in *(c)*, both the oscillatory and streaming flows have finite inertial and viscosity effects. Then we see a boundary layer adjustment for both these flows close to the wall, with the latter's boundary layer called the DC layer (analogous to a steady, direct current), typically ϵ^{-1} times larger than its AC counterpart. The DC layer further drives the fluid in the bulk, owing to finite velocity at its edges. This regime is aptly named *two-layer* streaming regime. A further increase in R_s decreases the thickness of both AC and DC layers until eventually at $R_s \gg 1$, they collide and form a *jet* along the oscillation axis.

2.3.2 Viscous streaming from a single, isolated circular cylinder with other actuations

Interest in different actuation modes was instigated by Davidson and Riley [39], who investigated the case of a single circular cylinder with $R_s \gg 1$ undergoing *non-harmonic actuations* of the form $x_{\text{COM}} = \sum_{i=1}^{n} \epsilon_i R \sin(\omega_i t + \phi_i)$, where n is the total number of *sinusoidal modes*. In their calculations, the streaming fields in the combined actuation case was seen to closely resemble the linear superposition of the streaming fields arising from an oscillating cylinder with i^{th} mode actuation, despite the non-linearity of the engendering mechanism. Miyagi and Nakahasi [109]'s theoretical analysis for a cylinder oscillating with a profile composed of two sinusoidal actuation modes ($n = 2$) revealed the existence of asymmetry in the streaming pattern because of the existence of a uniform flow component in the second order, in the oscillation direction. Tatsuno [110] conducted experiments with a cylinder oscillating with a sawtooth profile ($n \to \infty$) and reported a similar observation—while the total streaming field is a linear combination of the streaming from individual modes, a strong drift exists in the direction of oscillation, leading to asymmetry. Kubo and Kitano [111]'s analytical work considered cylinders oscillating in x and y directions with different frequencies, their COM coordinates tracing a Lissajous pattern. They observe that while qualitatively the structure of the streaming flow is retained according to the dynamical regime (no, one and two boundary layers), a similar uniform flow is induced at long distances from the cylinder.

In fact, Kubo and Kitano [111]'s cylinder trajectories resemble those undergoing small amplitude *rotary oscillations around an axis* that has non-zero offset from the center. Other works also investigated this type of motion, one among which is Kusukawa et al. [112]'s. They studied the same problem using a different theoretical approach and corroborated Kubo and Kitano [111]'s findings. We note that both these works fell within the one and two layer streaming limits. Around the same time, Taneda [52] analyzed the problem experimentally and found more striking patterns across the one layer, two layer and jetting regimes. The work of Riley and Watson [91] uncovered the fundamental mechanism involved in originating the patterns of the aforesaid regimes and provided quantitative arguments for the streaming visualization of Taneda [52]'s. A particularly interesting case occurs at the jetting limit—by controlling the axis-COM distance, we can focus the resulting jet to emanate from one side of the cylinder surface.

Another actuation mechanism involves *torsional and radial oscillations* of the cylinder. From asymptotic boundary layer theory, we know that streaming is only generated when there is a spatial gradient of amplitude (different parts of the body move with different speeds normal to its surface, such as an oscillatory flow over a circular cylinder) or phase (different parts move synchronously but with different phases, like oscillatory flow over a wavy wall) [31]. Both torsional and radial oscillations of a circular cylinder have neither and

hence does not generate a streaming field. In the former case, the unsteady shear waves in the AC layer decay exponentially into the bulk. In the latter, no shear (vorticity) is generated.

However, we observe interesting phenomenon when these actuations are *coupled* and thus allowed to interact with linear translational oscillations. Coupling torsional with translational oscillations, Riley [90]'s analytical work in the double boundary layer/jetting regime indicates that the boundary layer structures can be completely altered (and their characteristic velocity enhanced) by changing the amplitudes and relative phase of the modes, as long as their frequencies are commensurate. These changes are drastic in the limit of jetting, wherein we can, in a controlled fashion, alter the direction of the boundary layer-induced jet. If instead the frequencies are unequal, there is no interaction between the torsional and translational modes. A direct application of these streaming jets are in propulsion, investigated in part by several authors [92, 113–116]. Extension of Riley's work to other regimes were also performed [117]. Work on steady streaming from a combination of radial and translational oscillations has been sparse. The most notable among them is the work of Longuet-Higgins [118] and Longuet-Higgins [119] where a breathing bubble (undergoing radial monopolar oscillation) also experiences translational motion. Compared to the streaming field from linear oscillations [44], the resulting field has a changed structure (from quadrupolar to dipolar) and enhanced magnitude (slow rate of decay). Additionally, streaming generated from a breathing sphere/cylinder in the presence of a background slow (creeping) flow has also been resolved analytically [25, 61, 62, 120].

Another mode of actuation is the surface *squirming* motion [121, 122], used to mimic the surface velocities of ciliated micro-organisms. No two dimensional (cylinder) results are presented in literature yet, but striking squirming-generated streaming patterns have been shown analytically for three-dimensional spheres in the Stokes limit [123], which are hypothesized to be useful in individual and collective locomotion at low Reynolds numbers [56]. Squirming usually induces shape changes, which we discuss next.

2.3.3 Viscous streaming from other shapes

Literature on streaming from generic oscillating shapes have been few and far between. Moreover, we disregard cases such as a flow over a wavy wall where streaming arises due to phase–difference of velocities over the arc length of the solid. Thus much is still unknown in this particular aspect of streaming, in spite of many analytical works highlighting the importance of curvature and shape.

Davidson and Riley [39] were the first to seriously consider non-circular bodies when they analytically dissected the mechanism and discussed the characteristics of the jet emanating from an oscillating ellipse. Experimental works performed around the same time concentrated on shapes ranging from the usual (squares [54], triangles [55] and flat plate [124] with edges) to more esoteric ones (Joukowski airfoil [125]). The streaming

flow was seen to be very different in its form as compared to its circular counterpart, and so these works mapped the parametric space (comprising an appropriately selected $R_o - R_s$) to the streaming patterns seen. However no explanation was given as to what causes such differences. Riley [126] attempted a solution for the small amplitude circular motion of an elliptical and circular cylinder, with the focus on these differences between the physical mechanism (and thus the solution approach) in both the cases. Duck [127]'s computational work focused on oscillatory flow within a square cavity and noted the presence of four contra-rotating eddies with unequal circulations inside the cavity. The work of Pattani and Olson [128] numerically replicated the square, cylinder and airfoil experiments mentioned above [53, 54] and focused on the stability of the leading order oscillatory solution. The semi-infinite flat plate [129, 130] and streaming from sharp tips [99, 131] too have come under scrutiny, but without too much insight. The only other notable theoretical efforts were by Riley and Wybrow [132] for the torsional oscillations of an ellipse and Wybrow et al. [93] for an oscillating cylinder near a flat plate. The former carries over all the interesting observations seen for a coupled translation-torsional oscillating cylinder and hence displays a variety of streaming patterns. Recently, the problem of streaming from non-circular shapes and cavities has been revisited by Lieu et al. [48] in the one boundary layer limit in the context of predicting positions of inertial particle trapping.

2.3.4 Viscous streaming from multitudes

The first works to study viscous streaming from multiple oscillating bodies were all computational in nature. Yan et al. [133] investigated streaming from a cascade of circular cylinders placed in an unbounded fluid media and performed concomitant experiments. They noted that computationally predicted top-down/fore-aft symmetric streaming patterns were not observed experimentally beyond a certain R_s, which they estimated using bifurcation diagrams based on symmetric integral quantities. The next year, they performed computations and experiments on oscillating cascades of both circular and square cylinders [98] and analyzed the stability of the streaming solution with R_s. Both the works above demonstrate dramatic changes when multiple bodies are introduced. Theoretical works on two cylinder streaming also exist, with Coenen and Riley [94] predicting the direction and momentum flux of the jets when the distance between the cylinders change. Coenen extended this theory to include cylinders of different radii [95] and later on, accommodated other dynamical regimes ($R_s \lessapprox 1$) [96] (numerically), with a broad focus on streaming-field topology. Experiments conducted by House et al. [49] were aimed at a lattice of cylinders in the one boundary layer regime and predicted inertial particle trapping dynamics using a streaming flow model derived from associated computations. Chong et al. [51] also describes particle dynamics, but with a focus on inertial particle transport between streaming cylinders.

2.3.5 Three dimensional effects

For the sake of completeness, we briefly review theoretical, experimental and numerical works on three dimensional streaming effects. Analytical work has revolved around the dynamics and structure of the streaming field in the case of spheres [134–139] and spheroids [140]. With a focus on applications, experiments have also uncovered a wealth of information on streaming from a sphere [104, 141–144], multiple spheres [57, 145], spheroids [146, 147] and other complicated shapes [146]. Numerical works have also been performed [148–152], but mainly for complementing the discoveries made in experiments. Three-dimensional effects arising from the finiteness of physical cylinders have also been studied [46].

2.3.6 Applications

Adding to the those already presented in section 2.2, we present some more applications that viscous streaming has enabled over the past two decades. Pumping in the microscale has been achieved by arranging several oscillating bubbles in a favorable configuration [19, 82]. Streaming from multiple active objects can achieve a high degree of micromixing [20, 58], which has subsequently been used in a chemical micro-reactor [83] and for DNA hybridization [84]. Directed particle transport [85], assembly [57] and controlled particle trajectory manipulation, both with [86] and without other technologies [59, 87] have been made possible via streaming. This can be extended to micro-trapping of particles [47] and chemicals [88]. Additionally, it is ideal for use in biofluidics when compared to other methods of processing cells/micro-organisms. While these methods lead to detrimental effects on the manipulated biological material, streaming—being a second order effect—has less of an impact. Thus microorganism and cell trapping for lysis and subsequent gene transfection [23], drug delivery [153], cell homogenization [85] and enrichment [154] are applications in which the use of streaming flows proves beneficial. Inertial particle sorting (and by extension, cytometry) also take advantage of these flows [25, 61]. Streaming has also been utilised to drive a rotor for small scale power generation [60]. Other potential applications recognized in literature include microfabrication [155], cell patterning [156], as microscale switches [157], bed–scouring [93] and for cargo delivery. While microbubbles have been used for propulsion before [75, 158, 159], streaming was not the primary driving mechanism. However it is now being increasingly recognised that viscous streaming is an important phenomena in biological propulsion, especially in collectives [56].

2.4 Open questions

Armed with an holistic survey of extant literature, we can now identify unanswered questions on viscous streaming. We enumerate, but do not expand on, them below:

1. The exact occurrence of the first/second order asymptotic boundary layer theory breakdown in predicting the streaming field is unknown and so direct numerical simulations or experimental techniques are required for prognosis and subsequent analysis.

2. Streaming generated from complex actuations (coupled modes, squirming) are only now being resolved, but still in asymptotic limits (small R_o).

3. Streaming generated in the presence of other fluid effects (boundary layers, wakes, jets) have not been investigated.

4. The effect of *body curvature/shape* on the streaming field is not well established.

5. Only limited configurations (geometric, kinematic and dynamic) of multiple body streaming have investigated, with fundamental questions only partially answered.

6. No conclusive applications of streaming have yet been shown in an inertial environment, which is dynamically more complex and uncertain.

7. No attempts have yet been made to bring these different (multiple actuations, curvatures and bodies) streaming categories into one broad umbrella.

The last statement also holds when the length and time scales of the problem changes. An example of these are the high amplitude ($\epsilon > 0.2$) Keulegan–Carpenter (KC) flows. Even in cases when the amplitude is only moderately high, non-linear unsteady inertial effects are expected to dominate. Thus an entirely different set of parameters is used for scaling purposes in this regime—KC $= \pi\epsilon$ and $\beta = \frac{2\omega a^2}{\pi\nu}$, called the Keulegan Carpenter number and Stokes number respectively. Such a scaling is quite natural in this regime as the KC parameter represents the ratio of convective ($\boldsymbol{u}\cdot\boldsymbol{\nabla u}$) versus viscous forces, while the β parameter represents the ratio of accelerative $\left(\dfrac{\partial \boldsymbol{u}}{\partial t}\right)$ versus viscous forces. How these connect to the other natural scaling set $R_\mathrm{o} - R_\mathrm{s}$ still remains an unanswered question. Nevertheless, ignoring the scaling details, KC flows while conventionally studied from the perspective of macro length ($\sim \mathcal{O}(1)\,\mathrm{m}$) scales can potentially open up interesting flow control options in the scales of our interest—hence our fascination with them.

We proceed to review what has been researched in this particular topic, only touching upon the more important results. The predominant observations with increase in ϵ (and correspondingly R_o) is a number of

different vortex shedding mechanisms/regimes [65, 67–69, 160–163]. Many others have attempted to come up with qualitative yet intuitive explanations for the visualized vortex/streak-line patterns seen in the above experiments, and their effect of the generating cylinders' lift and drag coefficients [67, 164–168]. Interest in the transition between different regimes also lead to the study of instability mechanisms using Floquet analysis [66, 70, 71, 169]. These instabilities quickly develop and lead to three-dimensional effects [65, 163, 170–173] and eventually turbulence [72, 173–176]. Currently, the focus is on better understanding the oscillatory flow-generated instabilities [177, 178], KC flows from multitudes [179–182] and shapes [178, 183, 184]. We note that prior works have focused extensively on the high R_o limit and as such little is known about the complementary range of Reynolds numbers.

Thus, in spite of the wealth and diversity of literature pertaining to streaming and KC flows, we still understand surprisingly little. Consequently, high impact applications such as those concerning microscale flows mentioned earlier still remain out of reach. For example, streaming flows are not accounted for in the design of artificial mini-robots due to the lack of physical understanding of these phenomena in the case of complex, active shapes and multiple objects. As we have already seen, analytical treatments of streaming have been insightful but are restricted to cylindrical shapes. Experimental studies are physically constrained, expensive and have long turnaround times. We then look for insights through *simulations*.

Chapter 3

Simulation of streaming dynamics

In the context of simulating streaming, we recognize that its nature lends to several numerical difficulties—it is a relatively weak second-order effect and operates across significantly different time scales when compared to the body oscillations. This demands accurate and fast flow–structure interaction algorithms that can efficiently simulate long time periods, spanning many ($\gtrsim 100$) oscillation cycles. Such stringent requirements explain the existence of only a handful of numerical studies on streaming. In this context, our demonstration that numerical flow–structure simulations based on Remeshed Vortex Methods (RVM) [185] can accurately, quickly and robustly capture viscous streaming dynamics is significant.

We start this demonstration with simulations of a single oscillating circular cylinder in an unbounded, quiescent fluid, wherein our calculations show agreement with prior theory and experiments done across orders of magnitude in R_o, spanning three dynamic regimes (the single and double boundary layer regimes, as well as the jetting limit). We then extend this validation to a system of multiple cylinders. Thereafter objects with different actuations and shapes are considered. We also show that the RVM algorithm can capture the dynamics of KC flows as well, and map out a phase space of possible vortex and streakline patterns.

3.1 Fluid–structure interaction

3.1.1 Governing equations for two-dimensional FSI

We consider incompressible viscous flows in a domain (Σ) in which m moving rigid bodies are immersed. We denote by Ω^i & $\partial\Omega^i$ ($i = 1, \cdots m$) the support and boundaries of these solids. The flow is then described by the isothermal, incompressible (3.1) Navier–Stokes equation (3.2) for an isotropic Newtonian fluid with uniform density and viscosity, wherein the field dependence on the Eulerian coordinate $\boldsymbol{x}$ and time t is implicit.

$$\boldsymbol{\nabla} \cdot \boldsymbol{u} = 0 \quad , \quad \boldsymbol{x} \in \Sigma \setminus \Omega^i \tag{3.1}$$

$$\frac{\partial \boldsymbol{u}}{\partial t} + (\boldsymbol{u} \cdot \boldsymbol{\nabla})\, \boldsymbol{u} = -\frac{1}{\rho}\nabla P + \boldsymbol{g} + \nu \boldsymbol{\nabla}^2 \boldsymbol{u} \quad , \quad \boldsymbol{x} \in \Sigma \setminus \Omega^i \tag{3.2}$$

where $\boldsymbol{u}$ is the flow velocity, P is the mechanical fluid pressure, $\boldsymbol{g}$ represents the action of conservative body forces (such as gravity), ρ is the fluid density and ν is the kinematic viscosity. These equations are solved with appropriate initial and boundary conditions, all of which are problem–specific. We first delineate the solution strategy for the fluid component only and then consider the inclusion of solid objects in the flow.

In two-dimensions, to enforce mass conservation equation (3.1) in a differential volume identically (leading to numerical accuracy on the order of machine precision), we pick $\boldsymbol{u}$ to lie in the null-space of the divergence $\boldsymbol{\nabla}\cdot$ operator. We can then represent $\boldsymbol{u} = \boldsymbol{\nabla} \times (\psi \hat{e}_z)$, where $\psi(\boldsymbol{x}, t)$ is the instantaneous scalar streamfunction. To understand ψ's relation with the momentum equation, we convert it from its velocity ($\boldsymbol{u}$)–pressure (P) form 3.2, to the equivalent velocity ($\boldsymbol{u}$)–vorticity ($\omega \hat{e_z} = \boldsymbol{\nabla} \times \boldsymbol{u}$) form in the $\hat{e}_z$ direction, by taking its curl:

$$\frac{\partial \omega}{\partial t} + (\boldsymbol{u} \cdot \nabla)\, \omega = \nu \nabla^2 \omega + \frac{1}{\rho^2}\left(\nabla \rho \times \nabla P\right) \quad , \quad \boldsymbol{x} \in \Sigma \setminus \Omega^i \tag{3.3}$$

where the vortex stretching term $\omega \cdot \boldsymbol{\nabla} \boldsymbol{u}$ is ignored as it identically vanishes in two-dimensions, and $\boldsymbol{\nabla} \times \boldsymbol{g} = \boldsymbol{0}$ owing to body forces being conservative. Substituting for the pressure in the baroclinic terms from equation (3.2), we then get

$$\frac{\partial \omega}{\partial t} + (\boldsymbol{u} \cdot \nabla)\, \omega = \nu \nabla^2 \omega - \frac{\nabla \rho}{\rho} \times \left(\frac{\partial \boldsymbol{u}}{\partial t} + (\boldsymbol{u} \cdot \boldsymbol{\nabla})\, \boldsymbol{u} - \boldsymbol{g} - \nu \boldsymbol{\nabla}^2 \boldsymbol{u} \right) \quad , \quad \boldsymbol{x} \in \Sigma \setminus \Omega^i \tag{3.4}$$

which we solve for ω. The recovery of velocity is made possible via a Poisson equation between ω and ψ, stated as

$$\begin{aligned} \omega \hat{e}_z = \boldsymbol{\nabla} \times \boldsymbol{u} = \boldsymbol{\nabla} \times \boldsymbol{\nabla} \times (\psi \hat{e}_z) = -\boldsymbol{\nabla}^2 (\psi \hat{e}_z) + \nabla \boldsymbol{\nabla} \cdot (\psi \hat{e}_z) \\ \Rightarrow \omega = -\nabla^2 \psi \end{aligned} \tag{3.5}$$

coupled with appropriate boundary conditions. We mention in passing that the velocity–vorticity formulation has several computational advantages over its velocity–pressure counterpart [186].

We now consider the action of solid bodies immersed in the fluid. Let a solid boundary with velocity $\boldsymbol{u}_s$ move within the fluid. The boundary affects the fluid purely via the viscous no-slip (Dirichlet) velocity boundary condition $\boldsymbol{u}_f = \boldsymbol{u}_s$ at the fluid–solid interface where f and s represent the fluid and solid phase

respectively. The governing partial differential equations now read

$$\begin{aligned} \boldsymbol{\nabla}\cdot\boldsymbol{u} &= 0 \quad , \quad \boldsymbol{x}\in\Sigma\setminus\Omega^i \\ \frac{\partial \boldsymbol{u}}{\partial t} + (\boldsymbol{u}\cdot\boldsymbol{\nabla})\,\boldsymbol{u} &= -\frac{1}{\rho}\nabla P + \boldsymbol{g} + \nu\boldsymbol{\nabla}^2\boldsymbol{u} \quad , \quad \boldsymbol{x}\in\Sigma\setminus\Omega^i \\ \boldsymbol{u}_f &= \boldsymbol{u}_s^i \quad , \quad \boldsymbol{x}\in\partial\Omega^i \end{aligned} \tag{3.6}$$

The difficulty in solving this complicated nonlinear coupled boundary value problem can be ameliorated by incorporating the effect of the no-slip boundary condition as a finite forcing term in the momentum equation. This approach has several variants—Brinkmann penalization, Distributed Lagrange Multiplier, Direct Discrete forcing among others, out of which we choose the former for its ease of implementation, physical connection with flows over porous media and robustness in modeling arbitrarily shaped solids. This flow penalization should theoretically be effected only at the (Lagrangian) solid boundary points. However, for interfacing with the Eulerian fluid mesh, we model the solid using a fictitious domain approach wherein the solid is also considered a part of the fluid [187]. We then track the i^{th} solid body by its characteristic function χ^i, which is 1 inside the body and 0 outside (with suitable intermediate mollification for enforcing $\mathcal{C}^2$ continuity [186]). The fluid can then be *forced* to move with the body using a *penalization* term:

$$\begin{aligned} \boldsymbol{\nabla}\cdot\boldsymbol{u} &= 0 \quad , \quad \boldsymbol{x}\in\Sigma \\ \frac{\partial \boldsymbol{u}}{\partial t} + (\boldsymbol{u}\cdot\boldsymbol{\nabla})\,\boldsymbol{u} &= -\frac{1}{\rho}\nabla P + \boldsymbol{g} + \nu\boldsymbol{\nabla}^2\boldsymbol{u} + \sum_{i=1}^{m} \underbrace{\lambda\chi^i\left(\boldsymbol{u}_s^i - \boldsymbol{u}\right)}_{\text{Penalization}} \quad , \quad \boldsymbol{x}\in\Sigma \end{aligned} \tag{3.7}$$

where $\lambda \gg 1$ is the penalization factor [185, 186], with the above equations now valid throughout the entire domain. The introduction of χ^i also leads to the redefinition of the density field, as follows

$$\rho = \sum_{i=1}^{m}\left[\left(1-\chi^i\right)\rho_f + \chi^i\rho_s^i\right] \tag{3.8}$$

With the above changes, we finally write the equations for solving the one–way fluid–structure dynamics in the $\boldsymbol{u}$–ω form (once again, for the $\hat{e}_z$ component)

$$\frac{\partial\omega}{\partial t} + (\boldsymbol{u}\cdot\nabla)\,\omega = \nu\nabla^2\omega - \frac{\nabla\rho}{\rho}\times\left(\frac{\partial\boldsymbol{u}}{\partial t} + (\boldsymbol{u}\cdot\boldsymbol{\nabla})\,\boldsymbol{u} - \boldsymbol{g} - \nu\boldsymbol{\nabla}^2\boldsymbol{u}\right) + \lambda\sum_{i=1}^{m}\left[\boldsymbol{\nabla}\times\chi^i\left(\boldsymbol{u}_s^i - \boldsymbol{u}\right)\right] \tag{3.9}$$

The feedback from the fluid to the i^{th} body is described by Newton's equation of motions in two-

dimensions

$$m^i \ddot{\boldsymbol{x}}^i = \boldsymbol{F}_H^i$$
$$I^i \ddot{\theta}^i = M_H^i \tag{3.10}$$

where $\boldsymbol{x}^i$, θ^i, m^i, I^i, $\boldsymbol{F}_H^i$ and M_H^i are, respectively, the position of the center of mass, angular orientation, mass, $\hat{e}_z$ component of the moment of inertia, hydrodynamic force and moment. We solve equations (3.9) and (3.10) numerically using the algorithm described in the following section.

3.1.2 Remeshed Vortex Methods on uniform resolution grids

We briefly describe the numerical algorithm used to solve the above set of equations here. The interested reader is referred to Gazzola et al. [185], Gazzola [186], and Rees [188] for detailed numerical analysis and other implementation details. The key simplification involves employing first order Godunov time–splitting on equation (3.9), thereby decomposing the problem into simpler problems of field-reconstruction, poisson-solve, projection, penalization, baroclinic-update, diffusion, advection and body-update respectively, at the n^{th} time-step (henceforth denoted as a superscript).

Field-reconstruction involves (re)generating the χ^n and thus ρ^n (3.8) fields, based on past dynamics. The χ^n field is either imposed kinematically (such as a body moving with prescribed motion) or determined from integrating Netwon's laws (3.10). Any divergence in the velocity caused by body deformations can also be calculated in this step, and accounted for in later steps [185, 186].

We then solve the streamfunction *Poisson* equation $\nabla^2 \psi^n = \omega^n$, either with unbounded or periodic boundary conditions on a stationary uniform Eulerian grid. The uniform grid permits the use of fast solvers (FFT) based on convolution with the fundamental solution kernel, using the Discrete Fourier Transform (DFT). We can also recover the flow velocity using the Helmholtz decomposition $\boldsymbol{u}^n = \boldsymbol{\nabla} \times (\psi^n \hat{e}_z)$.

The translational and rotational velocity fed back from the fluid to the solid is computed directly using a *projection* approach [189]. This is done to eliminate computation of (noisy) surface stresses and thus the resulting integrated forces and moments (3.10). $\dot{\boldsymbol{x}}^i, \dot{\theta}^i$ are then directly computed by projecting them to the space of stress-free rigid body actuations, while conserving the total (fluid + solid) linear and angular momentum instantaneously.

We then *penalize* the flow on the uniform Eulerian grid to (instantaneously) match the no-slip condition of the solid object, according to the time-split equation below

$$\frac{\partial \boldsymbol{u}}{\partial t} = \sum_{i=1}^{m} \lambda \chi^{i,n} \left(\boldsymbol{u}_s^i - \boldsymbol{u} \right) \tag{3.11}$$

Discretizing the same with the implicitly stable (for real, positive λ such as this case) first-order Euler backward scheme with a time–step Δt leads to the following update for the velocity

$$\boldsymbol{u}^n \longleftarrow \frac{\boldsymbol{u}^n + \lambda \Delta t \sum_{i=1}^{m} \chi^{i,n} \boldsymbol{u}_s^{i,n}}{1 + \lambda \Delta t \sum_{i=1}^{m} \chi^{i,n}} \tag{3.12}$$

Consequently, we update the vorticity to

$$\omega^n \longleftarrow \boldsymbol{\nabla} \times \boldsymbol{u}^n \tag{3.13}$$

We take into account the *baroclinic* contribution seen in its time-split form below

$$\frac{\partial \omega}{\partial t} = -\frac{\nabla \rho}{\rho} \times \left(\frac{\partial \boldsymbol{u}}{\partial t} + (\boldsymbol{u} \cdot \boldsymbol{\nabla}) \boldsymbol{u} - \boldsymbol{g} - \nu \boldsymbol{\nabla}^2 \boldsymbol{u} \right) \tag{3.14}$$

All temporal derivatives in the above equation are done using a first-order accurate (explicit) forward Euler scheme, with the evaluation of the RHS quantities and the subsequent vorticity update done on the Eulerian grid. The $\nabla \rho$, $\boldsymbol{\nabla} \boldsymbol{u}$ and $\boldsymbol{\nabla}^2 \boldsymbol{u}$ terms are evaluated using the second-order accurate centered finite difference scheme. The update step is then

$$\omega^n \longleftarrow \omega^n + \Delta t \left[-\frac{\nabla \rho^n}{\rho^n} \times \left(\frac{\boldsymbol{u}^n - \boldsymbol{u}^{n-1}}{\Delta t} + (\boldsymbol{u}^n \cdot \boldsymbol{\nabla}) \boldsymbol{u}^n - \boldsymbol{g} - \nu \boldsymbol{\nabla}^2 \boldsymbol{u}^n \right) \right] \tag{3.15}$$

The *diffusion* equation for the vorticity given below is then solved using the explicit second-order mid-point Runge–Kutta scheme, with the Laplacian evaluated on the grid using the second-order accurate centered finite difference stencil. The split version and the update steps are given below.

$$\frac{\partial \omega}{\partial t} = \nu \nabla^2 \omega \tag{3.16}$$

$$\omega^n \longleftarrow \omega^n + \nu \Delta t \left(\nabla^2 \left[\omega^n + \frac{\nu \Delta t}{2} \nabla^2 \omega^n \right] \right) \tag{3.17}$$

We note that the use of an explicit time integrator here necessitates restricted time steps $\Delta t \leq \mathcal{O}\left((\Delta x)^2 / 2\nu\right)$.

The *advection* of vorticity is done, following equation (3.18), using Lagrangian vortex particles.

$$\frac{\partial \omega}{\partial t} + (\boldsymbol{u} \cdot \nabla) \omega = \boldsymbol{0} \tag{3.18}$$

The vorticity lying on the grid after the last sub-step is first distributed among particles using the M_4'

interpolation kernel, then advected with the (consistent) velocity field in accord with the midpoint second order Runge–Kutta scheme. At the end of this substep, the particles are remeshed onto the uniform regular grid using the same kernel. This particle–based advection also burdens the step-size that can be effectively taken by any explicit time–stepper, in the interest of preventing Lagrangian (particle) distortion. In this case, the restriction is based on the maximum strain rate and is given by $\left\|\boldsymbol{\nabla u}^{n-1}\right\|_{\infty} \Delta t^n \leq \text{LCFL}$, the Lagrangian CFL condition. The LCFL condition is less stringent than the CFL condition in cases of our interest, as we do not deal with high-deformation velocity fields. Once advection is done, any solid body *position/angle update* is performed and the simulation marches on to the next time-step.

3.1.3 Tracing streaming dynamics

To investigate/visualize dynamics over long time scales, we average the $\boldsymbol{u}$, ω and ψ fields over one oscillation cycle and obtain the time-averaged fields $\overline{\boldsymbol{u}}$, $\overline{\omega}$ and $\overline{\psi}$. This operation is described mathematically as follows

$$\overline{\zeta}\left(\boldsymbol{x}\right) \int_{T^n}^{T^{n+1}} dt = \int_{T^n}^{T^{n+1}} \zeta\left(\boldsymbol{x}, t\right)\ dt \tag{3.19}$$

where $\zeta\left(\boldsymbol{x}, t\right)$ refers to any of the aforesaid fields and $T^k = kT = \dfrac{2\pi k}{\omega}$. Numerically, the integration of the fields with time (RHS of equation (3.19)) is done by the (midpoint) trapezoidal scheme. This choice is motivated by the underlying physics—if one plausibly assumes that all oscillatory modes (of frequency ω and its harmonics) are periodic with period T (their fundamental periods may be different!), then the said scheme is spectrally accurate in time (and $\mathcal{O}\left(\Delta x^2\right)$ in space, following discussions from the prior section).

However over large time scales, a fluid particle does not travel with velocity $\overline{\boldsymbol{u}}$ or along isocontours of $\overline{\psi}$. Indeed, our computations calculate the average Eulerian fields while the fluid particle follows the Lagrangian fields, a fact recognized by prior works [33, 34, 42, 50, 118]. The velocity $\boldsymbol{U}$ experienced by a fluid particle starting at $\boldsymbol{x}$ at $t = 0$ is

$$\boldsymbol{U}(\boldsymbol{x}, t) = \boldsymbol{u}\left(\boldsymbol{x} + \int_0^t \boldsymbol{U}(\boldsymbol{x}, \tau) d\tau, t\right) \tag{3.20}$$

If the displacement of the fluid particle from its initial position $\boldsymbol{x}$ over one cycle is *small*, we can perform a Taylor expansion of the velocity field about $\boldsymbol{x}$ to obtain

$$\boldsymbol{U}(\boldsymbol{x}, t) = \boldsymbol{u}\left(\boldsymbol{x}, t\right) + \int_0^t \boldsymbol{U}(\boldsymbol{x}, \tau) d\tau \cdot \boldsymbol{\nabla u}\left(\boldsymbol{x}, t\right) \tag{3.21}$$

Performing the time average of the particle trajectory over one cycle allows us to calculate the *Stokes–drift*

correction to our Eulerian velocity field

$$\underbrace{\boldsymbol{u}_L^{\boldsymbol{x}_0=\boldsymbol{x}}(\boldsymbol{x})}_{\text{Lagrangian field}} = \underbrace{\overline{\boldsymbol{u}}(\boldsymbol{x})}_{\text{Eulerian field}} + \underbrace{\overline{\int_0^t \boldsymbol{U}(\boldsymbol{x},\tau)d\tau \cdot \boldsymbol{\nabla}\boldsymbol{u}(\boldsymbol{x},t)}}_{\text{Lagrangian correction}} \tag{3.22}$$

which leads to the following correction to our streamfunction field in the (r,θ) coordinate attached to our cylinder [118]

$$\underbrace{\psi_L(\boldsymbol{x})}_{\text{Lagrangian field}} = \underbrace{\overline{\psi}(\boldsymbol{x})}_{\text{Eulerian field}} + \underbrace{\overline{\frac{1}{r^2}\int_0^t \frac{\partial\psi}{\partial r}(\boldsymbol{x},\tau)d\tau \frac{\partial\psi}{\partial\cos\theta}(\boldsymbol{x},t)}}_{\text{Lagrangian correction}} \tag{3.23}$$

From literature (refer to the previous chapter), we estimate that $\boldsymbol{u} \sim \mathcal{O}(1), \overline{\boldsymbol{u}} \sim \mathcal{O}(\epsilon)$ and $\overline{\int \boldsymbol{U}(\tau)d\tau \cdot \boldsymbol{\nabla}\boldsymbol{u}(\boldsymbol{x},t)} \sim \mathcal{O}(\epsilon^2)$, with $\epsilon \ll 1$. We make an *ad hoc assumption* that this second order correction term can be neglected in calculating $\overline{\boldsymbol{u}}$, $\overline{\omega}$ and $\overline{\psi}$ (we advise caution in adopting this assumption as in general the Eulerian and Lagrangian streamlines can be quite different quantitatively, see [41, 50, 118]). We add that while we lose some physical meaning in adopting such an approximation, the Eulerian fields are still relevant as they are first-order approximations of the corresponding Lagrangian fields.

By neglecting this Lagrangian (Stokes drift) correction to the Eulerian streamfunction, we also notice that the averaging process involves no additional calculations (such as additional advection or Poisson-solve steps), except for the field cumulation. This also improves the time to solution (TTS), while retaining meaningful dynamics. Hence any visualization/calculation henceforth is done only using these averaged Eulerian fields.

3.1.4 Simulation parameters

Throughout this work, we choose a domain of physical size $[0\,\text{m}, 1\,\text{m}]^2$ with grid size 2048×2048, $\lambda = 10^4$, χ mollification length $\epsilon_{moll} = 2\sqrt{2}h$ (h being the grid spacing) and LCFL 0.01 to simulate the flow with unbounded boundary conditions, unless specified otherwise. This parameter set is chosen to strike an acceptable balance between computational speed and accuracy. A typical simulation with these parameters is run in single precision* for 24–48 hours on a single Cray XE6 node with two AMD 6276 Interlagos processors (sharing 32 hardware cores in between them) in the Blue Waters supercomputing cluster, over which $\sim \mathcal{O}(100)$ oscillation cycles are completed.

We note that the RVM algorithm with the aforementioned parameter set has been thoroughly validated for flow–structure interaction problems [185, 190, 191], with proven rigorous convergence properties [186]. We extend this validation and show that the algorithm can accurately capture streaming dynamics.

We employ SP (Single Precision) floating point numbers in the calculation of all fields to improve TTS. While there is no difference in the time taken to perform operations on a SP/DP (Double Precision) floating point number, the time taken by the Poisson-solve/advection routines are significantly longer in the case of the latter due to memory bandwidths stifling parallelism. The concomitant loss in precision was seen to only have a trivial effect, upon running some numerical streaming experiments.

3.2 Validation of streaming dynamics

We present multiple setups for validation in this section, each testing a different aspect of the physics that needs to be captured. To prevent monotony in our exposition, we give some physical insight into these cases in text snippets starting with  . These snippets offer additional information, but can be skipped in a cursory reading.

3.2.1 Lateral oscillations of a circular cylinder

For clarity of exposition, we once again present the physical setup and scaling parameters for the study of viscous streaming here. We consider a right circular cylinder of radius R, oscillating in-plane sinusoidally along one axis in a fluid of kinematic viscosity ν. The displacement of the cylinder center is then $x^{\mathrm{COM}}(t) = \epsilon R \sin(\omega t)$, where ϵ is the non-dimensional amplitude and ω is the frequency of oscillation. The oscillations

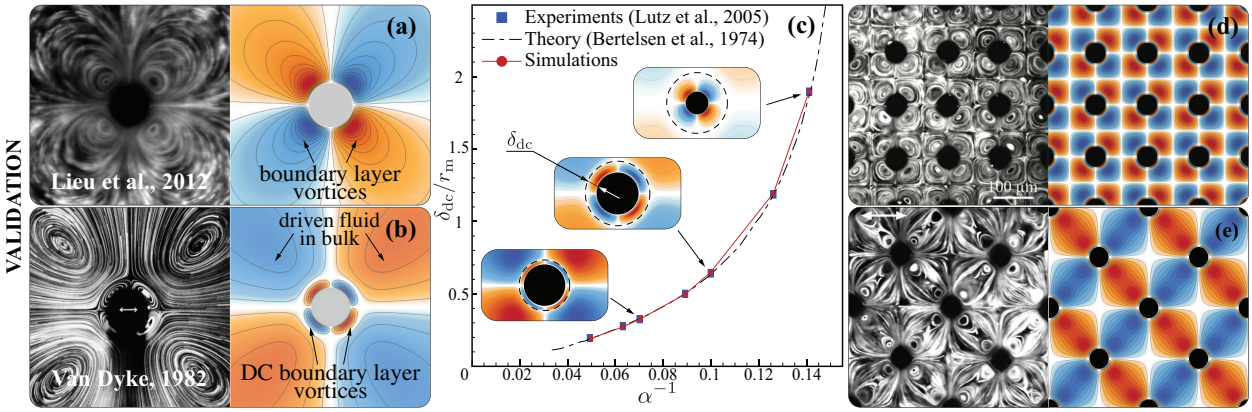

Figure 3.1: Validation: Comparison of $\overline{\psi}$ pattern in (a) single boundary layer ($R_o = 0.8, R_s = 0.04$) and (b) double boundary layer ($R_o = 6.28, R_s = 0.314$) regimes against the experiments of Lieu et al. [48] and Van Dyke and Van Dyke [63], respectively. (c) Normalized DC boundary layer thickness δ_{dc}/R vs. α^{-1} against experiments [46] and theory [41] in the DBL regime. (d,e) Comparison of streaming from multiple cylinders against the experiments of House et al. [49], wherein we employ a periodic boundary condition.

lead to a shear layer or a Stokes boundary layer near the cylinder surface with characteristic thickness $\delta_{\text{ac}} = \sqrt{\nu/\omega}$. We define the Womerseley number $\alpha = R/\delta_{\text{ac}}$. With characteristic oscillation velocity $U_{\text{o}} = \epsilon R\omega$, we define the oscillatory Reynolds number $R_{\text{o}}\left(= \dfrac{U_{\text{o}}R}{\nu} = \dfrac{\epsilon R^2\omega}{\nu} = \epsilon\alpha^2\right)$ determining oscillatory (periodic, fast time scale) dynamics. The streaming Reynolds number $R_{\text{s}}\left(= \dfrac{U_{\text{o}}^2}{\omega\nu} = \dfrac{(\epsilon R)^2\omega}{\nu} = \epsilon^2\alpha^2 = \epsilon R_{\text{o}}\right)$ characterizes the long term (steady) fluid response and associated flow structures.

Figure 3.1(a,b) illustrates these structures by plotting $\overline{\psi}$ and is seen to have distinct regions with clockwise (blue) and counter-clockwise (orange) rotating vortical fluid. Figure 3.1(a) depicts a case with $R_{\text{s}} \ll 1$ in the *single boundary layer* regime, where viscous effects dominate and the steady streaming flow is Stokes-like [37]. Figure 3.1(b) is representative of a case in the *double boundary layer* regime, with R_{s} spanning $O(1)$–$O(10)$, where both inertial and viscous effects are comparable. This leads to the *outer* DC boundary layer for the streaming flow, which has a finite thickness depending only on $\alpha = r_{\text{m}}\sqrt{\omega/\nu}$ as seen in figure 3.1(c). The DC boundary layer then '*drives*' the fluid in the bulk (from its outer surface) to set up long range streaming forces. We note that for a fixed $\epsilon = 0.05$, as in this work, we can use R_{o} alone to characterize streaming flows (as $R_{\text{o}} = R_{\text{s}}/\epsilon$). Finally, we scale up the simulations to predict streaming from multiple cylinders oscillating with the same frequency and no phase lag, in the (d) regular and (e) staggered lattices of figure 3.1. Overall, we observe good agreement with analytical and experimental studies involving individual and multiple cylinders.

We briefly explain the physics seen in figure 3.1. Steady streaming arises due to a drift of momentum/vorticity from the AC boundary layer into the exterior. This drift is usually represented as arising from a steady slip velocity at the edge of AC layer, with magnitude $\overline{U} = -\dfrac{3}{8\omega}\left(\dfrac{dA^2}{dx} + 2A^2\dfrac{d\gamma}{dx}\right)$, where U is the time independent coefficient of the external potential flow over the object, represented as $A(x)e^{\iota\gamma(x)}$, A being amplitude, γ being the phase and x is the wall-tangential coordinate. In our case of oscillatory flow past a circular cylinder, $U = A \cdot e^{\iota\cdot 0} = 2U_{\text{o}}\sin(x)$, leading to a steady slip of $\overline{U}_{\text{cylinder}} = -\dfrac{3U_{\text{o}}^2}{2\omega R}\sin(2x)$. This in turn *leaks* momentum/vorticity, which takes place predominantly by diffusion in figure 3.1(a) and by convection in figure 3.1(b), except close to the walls in the DC boundary layer wherein diffusion dominates. The latter is seen for small α^{-1} on the left part of figure 3.1(c), whereas increasing α^{-1} makes the DC boundary layer grow until it explodes at $\alpha \sim 0.14$—this leads to figure 3.1(a). This behavior is seemingly retained for multiple bodies with sufficient separation(figure 3.1(d,e)). We remark that the oscillating cylinder streaming structure is quadrupolar because of the $\sin(2x)$ term in the steady slip velocity $\overline{U}_{\text{cylinder}}$.

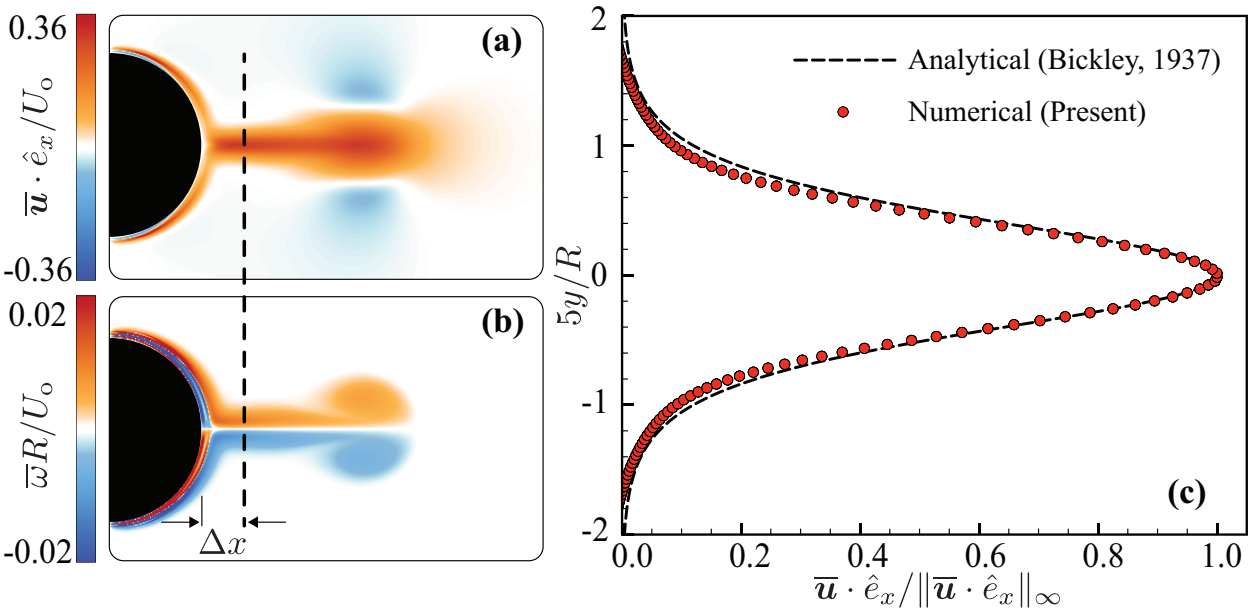

Figure 3.2: Validation: Viscous streaming fields simulated in the $R_s \gg 1$ limit ($R_o = 2000, R_s = 100$) and colored by (a) non-dimensional average axial velocity $\overline{\boldsymbol{u}} \cdot \hat{e}_x$, ($b$) non-dimensional average vorticity $\overline{\omega}$, clearly exhibits a jet. We measure the former at a cross–section (marked by black, dashed lines) at $\Delta x = 0.14R$ away from the surface. A comparison against the Bickley jet [106] in (c) shows good agreement.

We then increase R_o (and thus R_s) till we reach the jetting limit ($R_s \gg 1$). The boundary layers seen earlier now collide [36] and eject as a jet along the oscillation axis [39, 40, 42]. This is clearly seen in figure 3.2(a) and (b), wherein the $\overline{\boldsymbol{u}}$ and $\overline{\omega}$ fields are depicted respectively. Following [39] we compare the axial velocity profile of the jet to the theoretical planar jet in figure 3.2(c). We note that in this case the average quantities are not time-invariant, owing to the fluid's inability to satisfactorily dissipate the momentum added by body oscillations.

When R_o is increased, we have more vorticity confinement (due to high steady slip) across a smaller AC layer (due to increased R_o). Once *enough* vorticity has accumulated, it advects with its associated momentum and collides symmetrically along the axis. In this setting, the built–up momentum is leaked into the bulk flow as an unsteady jet.

3.2.2 Other actuations

Within this framework, it is also possible to simulate non-harmonic lateral oscillations (done trivially by changing the body actuation) or more complicated types of actuation. To test the validity of our simulation approach for the latter, we first simulate the cases of a torsionally oscillating cylinder and a cylinder with ra-

dial monopolar volume-changing oscillations. Both these cases *do not* exhibit streaming (section 2.3), which should reflect in our simulations as well. Computationally, we assess this question of streaming–*existence* by calculating the kinetic energy $\overline{K} = \frac{1}{2}\int |\overline{\boldsymbol{u}}(\boldsymbol{x})|^2 \boldsymbol{dx}$ of the stationary averaged flow $\overline{\boldsymbol{u}}$ for dynamically equivalent simulations (same peak velocities and length scales). Comparing the cases of lateral and torsional/radial oscillations, the latter cases have $\overline{K}_{\text{torsional/radial}}$ approximately $0.1 - 1\%$ of the former. Hence we correctly capture the *no-streaming behavior* within some margin of computational error.

The former case involving *torsional oscillations*, when combined with isochronous lateral oscillations leads to interesting physics, especially in the jetting limit. We consider such a laterally oscillating cylinder with superposed torsional oscillations of the form $\theta(t) = 2\pi\epsilon_{\text{t}} \sin(\omega t + \phi_{\text{t}})$, the subscript t indicating torsion. Introduction of the torsional peak velocity $U_{\text{t}} = 2\pi\epsilon_{\text{t}} a\omega$ and the phase difference between the modes $\gamma = \phi_{\text{t}} - 0$ further helps characterize relevant physics. Drawing from a prior work [90], we define $\lambda = U_{\text{t}}/U_{\text{o}}$ and the characteristic non-dimensional B parameter that equals $5\lambda \sin\gamma + 3\lambda\cos\gamma$. Riley [90] predicted that one

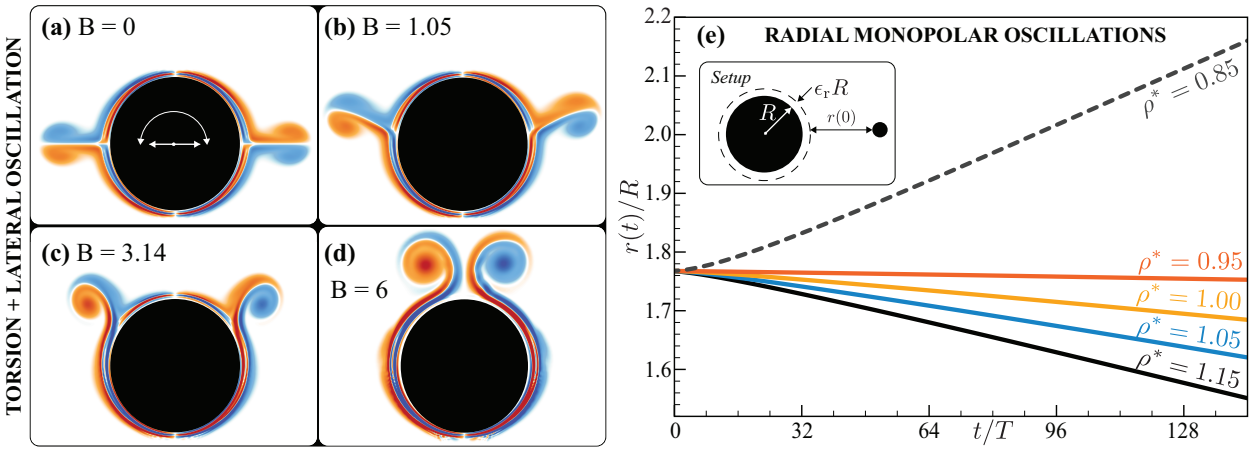

Figure 3.3: Validation: Adding torsional oscillations to a laterally oscillating cylinder ($R_{\text{o}} = 2000, R_{\text{s}} = 100$) leads to different directions (from equatorial to polar) of ejection of the jet (colored by $\overline{\omega}$) based on the magnitude of B: (a) 0, (b) 1.05, (c) 3.14, (d) 6, thus agreeing with the theoretical predictions of Riley [90]. We keep γ invariant throughout and effect the change in B only via changes in λ. If we instead consider an active cylinder undergoing monopolar radial oscillations and place passive density-mismatched finite-sized inertial cylinders closeby, we expect a behavior inversion in the trajectories of these cylinders. (e) shows this inversion for passive cylinders of different density contrasts $\rho^* \in [0.85, 1.15]$, with denser cylinders being attracted towards the active oscillating cylinder.

can control the direction of jet ejection by changing this parameter alone (with $B = 0$ indicating no torsion and hence a symmetric equatorial jet and the asymptotic case of $B = 6$ indicating one, strong polar jet). Upon reproducing this setup in figure 3.3(a–d), we notice that our computations qualitatively reproduce the predicted behavior for different values of $B \in [0, 6]$. One interesting application of these oriented jets lie in self-propulsion [92, 113–116].

The interaction of the torsional and translational components are captured exclusively by the wall-boundary conditions. While in the case of lateral oscillations, the slip velocity at the edge of the AC layer is $\overline{U} = -6k\cos(x)\sin(x) = -3k\sin(2x)$ as seen earlier (k is an unimportant proportionality factor), the torsional + lateral case has slip velocity $\overline{U} = k\cos(x)\left(-6\sin(x) + B\right)$. In both the cases, the boundary layer attaches (originates)/separates at the stagnation point, i.e. when the slip velocity is zero, the type of the stagnation point (attachment/separation point) depending on its local behavior (the slope of $\overline{U}$ around the point). Owing to the $\cos(x)$ factor in both the slips, the boundary layer always originates at $x = \pm\dfrac{\pi}{2}$ i.e. at the poles. However the point of separation—where we see the ejection of the jet—is different. In the former, this point is at $x = 0,\ \pi$ leading to an axis-oriented jet. In the latter, this point occurs at $x = \sin^{-1}(B/6),\ \pi - \sin^{-1}(B/6)$, leading to an oriented jet. If $B \geq 6$ however, the layer originating at $x = -\dfrac{\pi}{2}$ encircles the cylinder and collides at $x = \dfrac{\pi}{2}$, owing to its higher momentum flux. As we have seen in the validation above, this leads to a single jet at the top.

The latter case involving *radial monopolar oscillations* of the cylinder is quite similar to standard microbubble streaming experiments [25, 61, 62] and has been used for effecting density–based particle sorting/differential transport [120]. In the interest of particle transport over long time scales and to authenticate our modeling of the baroclinic force term in the differential momentum equation (3.9) arising from fluid–solid density contrast, we consider such a cylinder with a fixed center undergoing monopolar radial oscillations of the form $\underline{\mathrm{R}}(t) = R\left(1 + \epsilon_{\mathrm{r}}\sin(\omega_{\mathrm{r}}t)\right)$, with the subscript r denoting radial oscillations. The characteristic velocity and length scales for this problem are $\epsilon_{\mathrm{r}}R\omega_{\mathrm{r}}$ and R respectively, following which the usual dynamic parameters are defined. We then consider small passive inertial cylinders of radius $R/5$, which are free to respond to the flow generated by the motion of the oscillating cylinder. A popular result pertaining to this setting corresponds to these passive bodies being attracted to/repelled from the oscillating cylinder based on its density contrast with the surrounding fluid [192]. In five separate experiments, we place particles of contrasts $\rho^* = \rho_{\mathrm{s}}/\rho_{\mathrm{f}} = 0.85, 0.95, 1.00, 1.05, 1.15$ at an initial radial position of $r(0)/R = 1.767$, seen in the inset of figure 3.3(e). We track the radial positions of these particles as the cylinder oscillates and notice, in accordance with theory, a qualitative inversion in the particle behavior (attraction/repulsion) (figure 3.3(e)). This further vindicates our modeling approach in the context of multiple bodies with mismatched densities.

The trajectory of an inertial particle in a viscous flow is still a topic of interest. In the two–dimensional case presented above, the widely used Maxey–Riley equations for calculating inertial particle trajectory can not be employed, as the fundamental assumption concerning the negligibility of flow-disturbances induced by the particles in the flow is violated. While a quantitative comparison with theory is impossible in this case, we observe the predicted inversion behavior seen in other three dimensional experiments.

A related deforming (and volume-changing) actuation is the two-dimensional *squirming motion* proposed by Blake [121]. Such squirming motions are characteristic propulsion generating mechanisms of microscale organisms, and may generate complicated streaming fields, as hypothesized in section 2.2. Squirming involves prescribing spatially varying radial and torsional oscillations on the surface of the form

$$\begin{aligned} \tilde{R}(\theta,t) &= R\left[1+\sum_{i=1}^{n}\{\epsilon_i^{\mathrm{r}}\sin(\omega_i t)\}\cos(i\theta)\right] \\ \tilde{\theta}(\theta,t) &= \theta+2\pi\left[\sum_{i=1}^{n}\{\epsilon_i^{\theta}\sin(\Omega_i t)\}\sin(i\theta)\right] \end{aligned} \tag{3.24}$$

where $\tilde{R}(\theta,t)$ and $\tilde{\theta}(\theta,t)$ are the radial and angular positions of the Lagrangian point (R,θ) in the initial configuration; $\epsilon_i^{\mathrm{r}},\omega_i$ refer to the amplitude and frequency parameters of the mode i radial deformation; $\epsilon_i^{\theta},\omega_i$ refer to the amplitude and frequency parameters of the mode i angular deformation and n is the total number of shape modes. We constrain $\epsilon_i^{\mathrm{r}} \ll 1$ and $\epsilon_i^{\theta} < 0.125$ to prevent non-physical solutions for the solid surface. Thus every point on the surface, due to this imposed motion, has a spatially varying normal and tangential velocity. As our fluid quantities are calculated on the Eulerian mesh, corresponding to some value of the $\left(\tilde{R}(\theta,t),\tilde{\theta}(\theta,t)\right)$ tuple, we first solve for θ given the Eulerian $\tilde{\theta}$ using Brent's non-linear root finding algorithm.

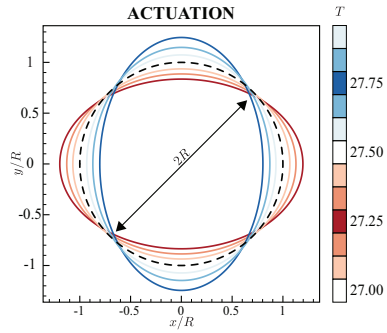

Figure 3.4: Deformations (exaggerated, $\epsilon_2^{\mathrm{r}} = 0.2$) associated with the second mode squirming motion.

We first test the capability of our solver to handle such complicated actuations. We consider the simplest possible non-trivial (i.e. spatially varying) actuation, with $\epsilon_2^{\mathrm{r}} = 0.02, \epsilon_2^{\theta} = 0.02, \omega = \omega_2 = \Omega_2 = 4\pi$ and all other coefficients set to 0. The resulting cylinder deformation is shown in figure 3.4.

Following [64], we characterize the Reynolds number $Re = 4\omega R^2/\nu$ using the non-dimensional time $T = 2\pi t/\omega$, distance r/R and velocity ωR. This low-amplitude case has an analytical and numerical solution [64], which we validate against. Figure 3.5 exhibits the $\boldsymbol{u}$, ω field validation at four different times from $T = 27.00 - 27.75$. The validation indicates that RVM can accurately capture squirming-dynamics.

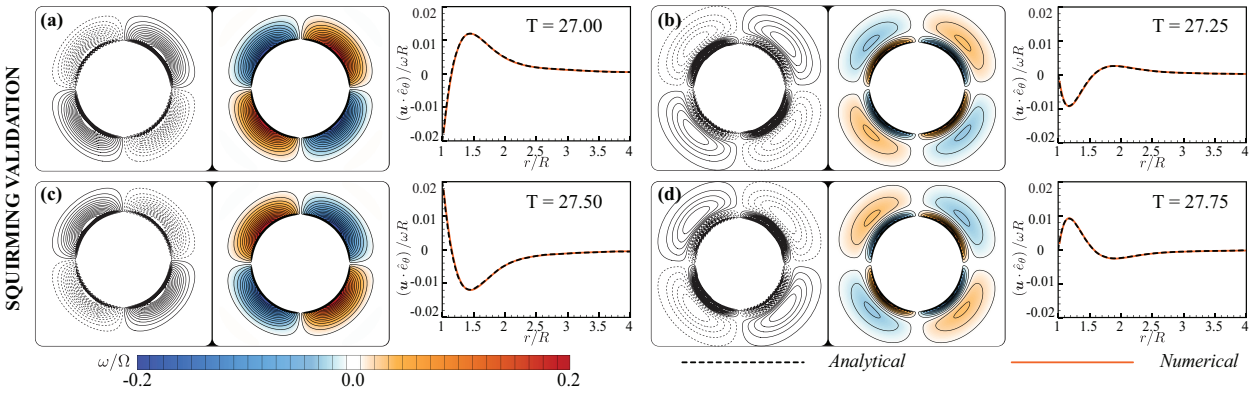

Figure 3.5: Squirming validation: By incorporating the kinematic deformations of a second mode squirmer, we enable comparison against analytical solutions for non-trivial deformations (including imposed slip on the surface). For the case of $Re = 100$ and at time (a) $T = 27.00$, we first show the vorticity fields computed using a viscous vortex particle method [64] (solid and dashed lines indicate positive and negative values respectively) against which we compare our vorticity fields (colored, with 32 equi-spaced contour lines). We then plot the analytical and our numerical circumferential velocity profile with r/R at $\theta = 45°$. This process is repeated at other times: (b) $T = 27.25$, (c) $T = 27.50$, (d) $T = 27.75$. Our calculations are in agreement with analytical and other numerical results.

With the fluid dynamics instigated by arbitrary squirming motion validated, we now visualize the engendered streaming fields for specific modes. We show this in figure 3.6, where streaming in the DBL regime and jetting limit are displayed alongside one another for the same actuation (with α^{-1} alone indicating the streaming regime). Because of inherent symmetries in the modes, the streaming field is no longer quadrupolar in the DBL regime (as in the case of lateral oscillations), but has several *segmented* eddies with *varying strengths* across the polar direction, which collide with one another as the α^{-1} decreases to form multiple jets. Indeed, such behavior is not too different from flow fields generated by the ciliated, squirming starfish larvae, first observed by Gilpin et al. [80], which are utilized by the organism to regulate/switch between locomotion and feeding phases.

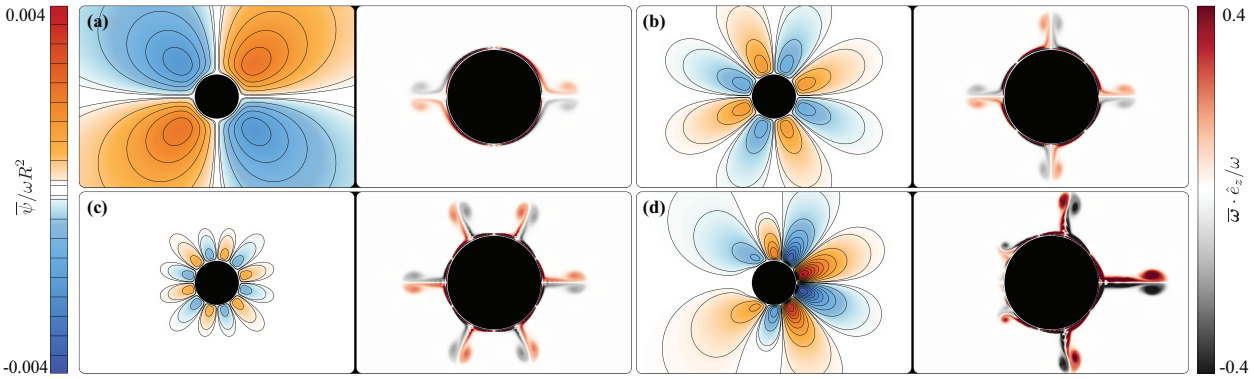

Figure 3.6: Streaming fields generated by squirming motions in the DBL regime (left, with $\alpha^{-1} = 0.0398$) and jetting limit (right, with $\alpha^{-1} = 0.00398$), visualized respectively by non-dimensional $\overline{\psi}$ amd $\overline{\omega}$ respectively. (a) exhibits the case of a mode 1 squirmer with $\epsilon_1^{\mathrm{r}} = 0.0, \epsilon_1^{\theta} = \frac{1}{120}$, (b) exhibits the case of a mode 2 squirmer with $\epsilon_2^{\mathrm{r}} = 0.0, \epsilon_2^{\theta} = \frac{1}{120}$, (c) exhibits the case of a mode 3 squirmer with $\epsilon_3^{\mathrm{r}} = 0.0, \epsilon_3^{\theta} = \frac{1}{120}$. Comparing these three dynamically equivalent but kinematically different cases, we observe more segmentation in the polar direction but faster radial field decay as the mode number increases, a response which might be useful in regulating/effecting local flow control. (d) exhibits the case with all the above modes combined, with the same parameters for the individual modes as the cases of (a,b,c). Such a combination leads to a preferential direction in which the streaming fields are relatively *stronger*.

The patterns seen in the case of an angular mode squirmer can be understood from the slip-velocity relation. In this case, we can equivalently think of an oscillatory flow past a squirming cylinder with the time-independent coefficient $U = 2U_o \sin(ix)$, i being the mode of the squirmer. This leads to a steady slip velocity of the form $\overline{U} = k \sin(2ix)$. This results in additional stagnation points (numbering $4i$ for the i^{th} mode squirmer), half of which are attachment points and the other half being points of *boundary layer* separation. The effect of the $\sin(2ix)$ term is also seen in the number of segments of the $\overline{\psi}$ fields in the DBL regime, and subsequently in the number of jets at higher R_{o}.

3.2.3 Lateral oscillations of arbitrarily shaped cylinders

The squirming modes shown above consider only angular (slip) deformations, but not radial deformations. Radial deformations are associated with *changes in shape*, making their simulation non-trivial. While we showed that the dynamics originating from shape perturbations to a circular cylinder are captured correctly (the squirming validation done prior, a mode 2 radial deformation case shown in the left panel of figure 3.7(a) and the bean shape in the right panel of figure 3.7(a)), arbitrary shapes (including shapes with sharp corners, such as a square) can still pose an issue numerically. We then proceed to compare our streaming fields against previous experiments concerning different shapes, which in-

clude a square (figure 3.7(b)), triangle (figure 3.7(c)) and a diamond (figure 3.7(d)). We also performed such comparisons across different dynamic regimes but do not present it here for the sake of brevity.

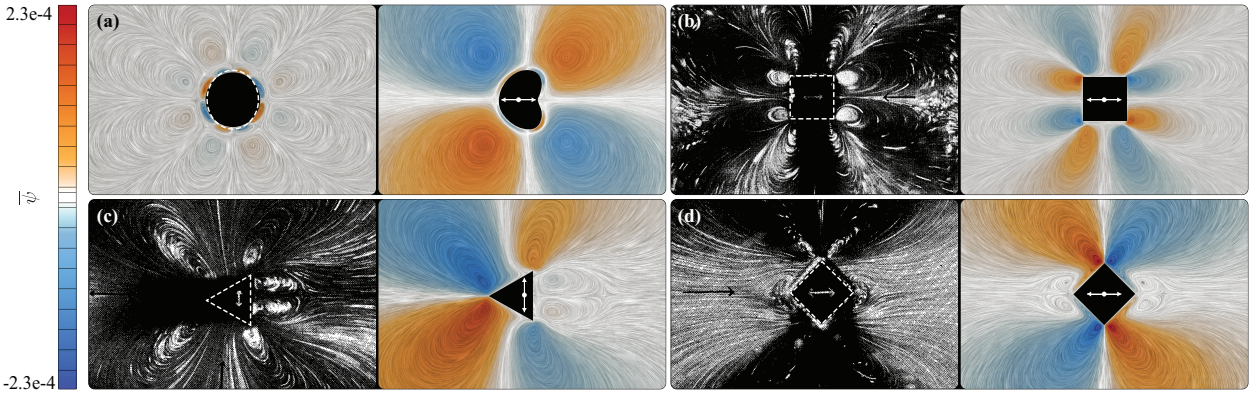

Figure 3.7: Validation: Streaming from arbitrary shapes, visualized by the Line Integral Convolution (LIC) of $\overline{\boldsymbol{u}}$ field and colored by $\overline{\psi}$. The actuations are indicated by solid white lines. Starting from (*a*, left) a radially deforming mode 2 squirmer $\left(\epsilon_2^{\mathrm{r}} = 0.1, \epsilon_2^{\theta} = 0.0, \alpha^{-1} = 0.0398\right)$ and (*a*, right) a laterally oscillating bean with $\epsilon = 0.05, \alpha^{-1} = 0.0498$, we proceed to compare streaming for different shapes against experiments: (*b*) a square $\left(\epsilon = 0.0752, \alpha^{-1} = 0.084\right)$ compared against Tatsuno [54], (*c*) a triangle $\left(\epsilon = 0.101, \alpha^{-1} = 0.1792\right)$ compared against Tatsuno [55] and finally (*d*) a diamond $\left(\epsilon = 0.0584, \alpha^{-1} = 0.09615\right)$ compared against Tatsuno [54]. We add that only a qualitative comparison is feasible owing to the lack of quantitative studies in literature. In spite of this limitation, we observe good agreement with experiments. The shape parameters used to construct the bean is given in the Appendix.

A plausible way to think about streaming from different shapes is in terms of its curvature κ—while all parts of the shape move with the same amplitude A, regions of higher curvature $\kappa^{\mathrm{loc}} = 1/R^{\mathrm{loc}}$ see a higher non-dimensional amplitude $A/R^{\mathrm{loc}} = \kappa^{\mathrm{loc}} A$ than the rest of the shape. Such high ϵ usually changes the dynamics, as we will see in the next section. This change in the dynamics can be confirmed by taking a glance at figure 3.7, wherein corners/tips in the shape lead to very different streaming profiles compared to the cylinder. These corners/tips are usually regions of very high curvatures.

Armed with a holistic yet rigorous validation, we are now confident of tackling streaming problems involving multiple, active/passive, arbitrarily-shaped bodies with complex actuations and density variations. We now extend this validation to streaming's unsteady counterpart—the Keulegan–Carpenter (KC) flows—in the next section.

3.3 Validation of KC dynamics

We perform two sets of validation studies to predict KC dynamics—one quantitative and another qualitative. The qualitative validation showcases a number of flow *regimes*, some of which are of interest to us in the context of flow and particle control in $R_o \in \mathcal{O}(1) - \mathcal{O}(100)$—which motivates the need for this section. The choice of parameters to describe the dynamics in this section are $\mathrm{KC} = \pi\epsilon$ and $\beta = \dfrac{2\omega a^2}{\pi\nu}$, such a choice motivated by our intention to maintain relevance to KC flow literature. They are related to the $R_o - R_s$ parameter set by the relation $\mathrm{KC} = \pi\dfrac{R_s}{R_o}$ and $\beta = \dfrac{2R_o^2}{\pi R_s}$.

The *quantitative validation* involves comparison of our fields against the experiments and simulations of Dütsch et al. [166]. To this extent, we simulate an oscillating cylinder in a quiescent fluid with $\mathrm{KC} = 5$ and $\beta = 20$ (for context, this case has $\epsilon = \dfrac{5}{\pi}$, $R_o \sim 50$, $R_s \sim 80$). Here, effects associated with flow separation predominate and the resulting flow is non-stationary. However, close to the cylinder-path the leading order dynamics are still oscillatory (including *higher order* oscillatory components). Figure 3.8(a) displays the vorticity and velocity fields associated with this flow, along with designated stations (marked with dashed lines), at which we compare the $\overline{\boldsymbol{u}} \cdot \hat{e}_x$ and $\overline{\boldsymbol{u}} \cdot \hat{e}_y$ components at some time $t = kT = \dfrac{2\pi k}{\omega}$ (figure 3.8(b,c)).

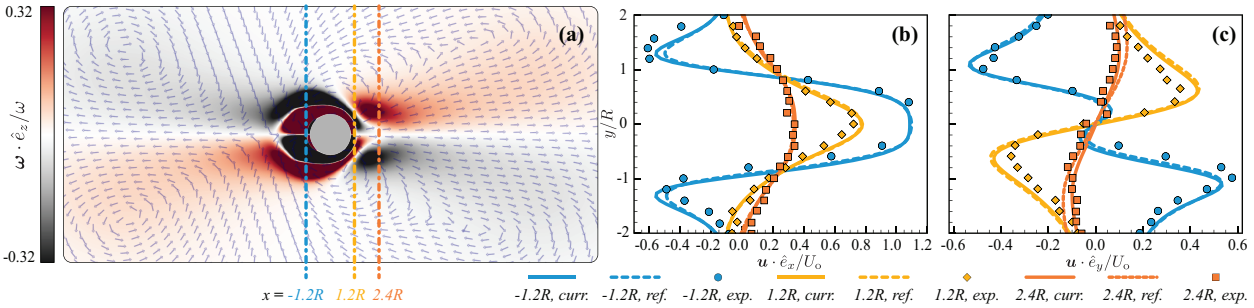

Figure 3.8: Validation: Simulation of the unsteady flow associated with $\mathrm{KC} = 5$ and $\beta = 20$ results in the $\boldsymbol{\omega} \cdot \hat{e}_z$ pattern shown in (a), alongside vectors of $\boldsymbol{u}$. Such a pattern evolved over a complicated trajectory involving vortex generation in half cycles, vortex-mixing, destruction and advection. Drawing samples of the velocity components at stations $x = -1.2R,\ 1.2R,\ 2.4R$ marked in (a) enables (b,c) comparison of our fields (*curr.*) against reference simulations (*ref.*) and experiments (*exp.*) of Dütsch et al. [166]. Our calculations agree with these simulations and experiments.

With some degree of confidence in our ability to predict KC dynamics, we change the amplitude (ϵ) and R_o to map out a phase space. In this phase space, we correlate the dynamics at different parameters by monitoring the time-dependent vorticity field and the integrated streakline patterns [65]. The latter involves seeding tracer particles azimuthally around the cylinder (close to its surface) and observe their evolution in time. We color these tracers based on its initial (seeded) position (from blue at initial azimuthal position $\theta = -\dfrac{3\pi}{2}$ to red at $\theta = \dfrac{\pi}{2}$). The phase space, along with the different flow regimes, is shown in figure 3.9.

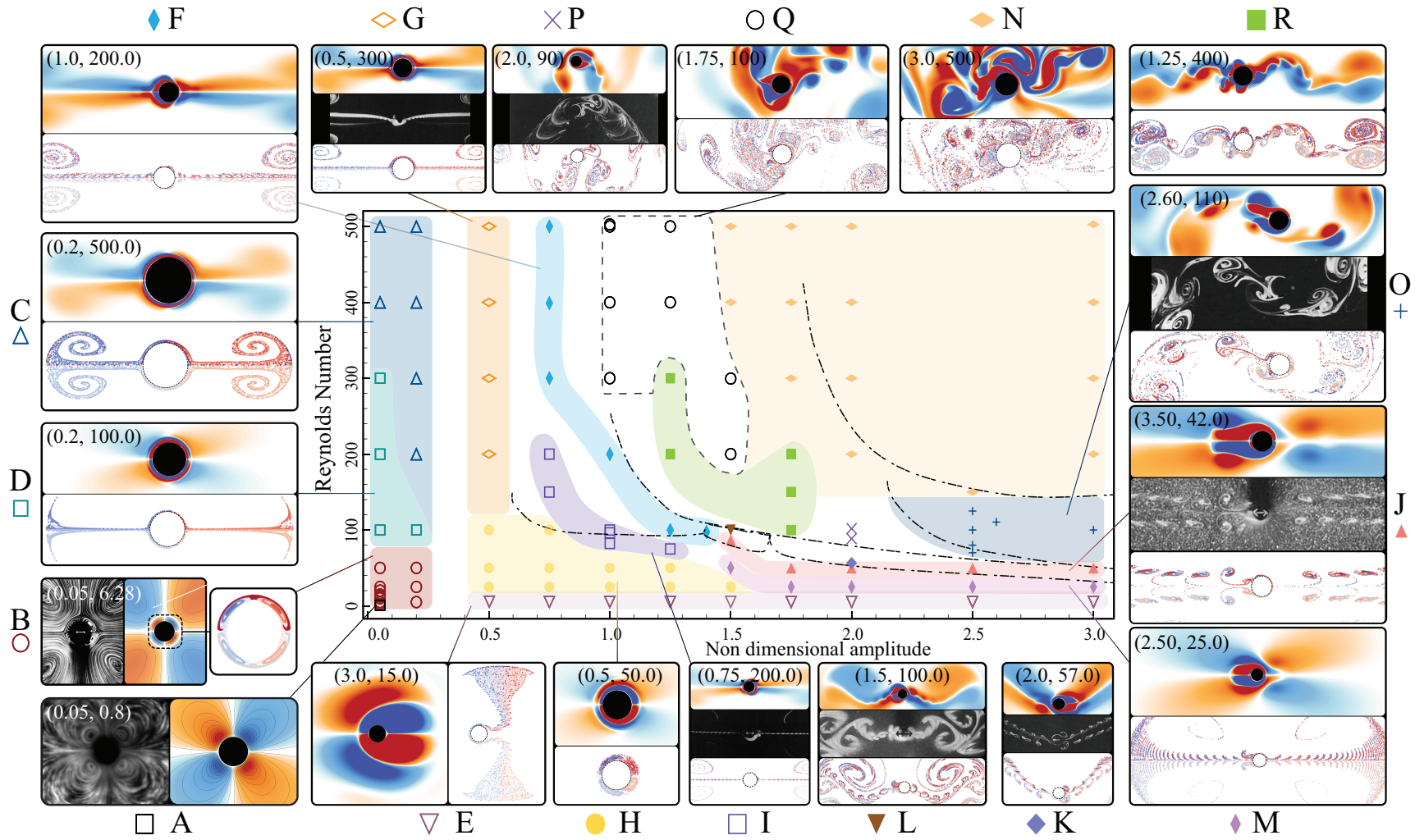

Figure 3.9: Validation: The phase space of vortex dynamics and streakline patterns plotted against the non-dimensional amplitude ϵ on the x–axis and the oscillatory Reynolds number R_o on the y–axis. Simulated values are marked with a symbol. Similar symbols are grouped together to form the boundaries of a regime, which are then demarcated with different colors. The name corresponding to a regime is specified below its representative image along with the aforementioned symbol. The (ϵ, R_o) parameters used in an image are mentioned on the top-left corner of the image. To enable qualitative comparison against equivalent experiments whenever possible, we also affix reference experimental images (pathlines from Lieu et al. [48] for A, pathlines from Van Dyke and Van Dyke [63] for B and integrated streaklines from Tatsuno and Bearman [65] for all the other regimes) along with our fields. We additionally plot, with dashed-dotted black lines, the regime demarcation lines from Tatsuno and Bearman [65]. Our regime demarcations and integrated streakline snapshots are consistent with their experimental findings.

Regime	Features
A	Single boundary layer streaming.
B	Double boundary layer streaming, streaklines are contained within the DBL.
C	Small amplitude jetting limit, no up-down or fore-aft particle mixing.
D	Transitional regime between B, C with intermediate features of both.
E	High amplitude flow that quickly diffuses vorticity and particles in the perpendicular direction. Integrated streaklines analogous to regime A.
F	Medium amplitude jetting with significant flow separation and cross-interaction, fore-aft particle mixing.
G	Medium amplitude jetting but only due to BL collision—hence no fore-aft particle mixing.
H	Medium amplitude oscillations that leaks (and does not shed) vorticity into the bulk. Particles *stick* to the cylinder without any mixing, similar to regime B.
I	Medium amplitude oscillations that jets without shedding—similar to F—but is shaped differently due to effects of higher viscosity. Particles exhibit significant fore-aft mixing.
J	Symmetric vortices shed and pushed downstream by the momentum flux emanating from the cylinder and is accompanied by mixing.
K	Shed vortices are convected obliquely w.r.t the oscillation axis, carrying the mixed particles with it.
L	Shed vortices now *roll up* symmetrically and form a vortex-street, thoroughly mixing the particles.
M	Similar to regime J, but with the streakline patterns manifesting differently owing to higher coherence within a shed vortex, possible due to lower R_o.
N	Chaotic asymmetric vortex shedding.
O	Asymmetric vortex shedding leads to diagonal vortex streets, with well-mixed particles.
P	Vortex shedding with irregular switch in the direction of vortex and mixed-particle convection.
Q	Transition between regimes F and N, that starts as a jet that eventually breaks down into chaos.
R	Similar to regime Q, but with the stability of the jet preserved for longer times, which also reflect in the particles not experiencing top-bottom mixing.

Table 3.1: Principal features of the regimes shown in figure 3.9

The evolution of tracer particles in time is achieved by temporal integration of the ODE

$$\frac{\mathrm{d}\boldsymbol{x}^p(t)}{\mathrm{d}t} = \boldsymbol{u}\left(\boldsymbol{x}^p(t), t\right), \quad \boldsymbol{x}^p(0) = \boldsymbol{x}_0^p$$

where $\boldsymbol{x}^p(t)$ is the position of the tracer particle at time t and $\boldsymbol{u}\left(\boldsymbol{x}^p(t), t\right)$ is the corresponding fluid velocity. This step is blended into our algorithm naturally by performing an additional particle-advection step.

The phase-space diagram of figure 3.9 shows rich dynamics, even when limited to the range $\mathcal{O}\left(1 - 100\right)$ of R_o that we are typically interested in. In this setting, the integrated streakline visualization using particles is doubly illuminating as it (i) clearly highlights the underlying dynamics, drawing attention to any differences between the regimes and (ii) lays the foundation for directing the trajectory of a small particle using only oscillatory motions. The latter is especially important as a preliminary, albeit crude, tool in facilitating potential applications involving *inertial* particle manipulations such as directed drug delivery. In this context of particle manipulation, we apply our findings and utilize the tools validated from this chapter to enable transport across long distances. This is elaborated upon in the next chapter.

Chapter 4

Inertial particle transport via viscous streaming[1]

In this chapter, we investigate the capability of an active body (master) to manipulate a passive object (slave) purely via contactless flow-mediated mechanisms, motivated by potential applications in microfluidic devices and medicine (drug delivery purposes). We extend prior works on active–passive cylinder pairs by superimposing periodic oscillations to the master's linear motion. Such oscillations produce an additional viscous streaming field, which is leveraged for enhancing slave transport. We see that superimposing oscillations robustly improves transport across a range of Reynolds numbers. Comparison with results without oscillations highlights the flow mechanisms at work, which we capitalize on to design (master) geometries for augmented transport.

4.1 Introduction

Here, we consider two-dimensional flow-mediated transport systems operating in flow regimes characterized by finite, moderate Reynolds numbers ($1 \leq Re \leq 100$). In particular, we explore strategies based on viscous streaming effects discussed thus far to enhance the capability of an active leading object to transport, trap and manipulate passive trailing ones.

We are once again motivated by the accelerated pace of development of artificial and biohybrid [77, 78, 194] mini-bots enabled by recent simulation [100, 195] and fabrication advances [194]. This new breed of mini-bots predominantly operates in fluids, and brings within reach a range of novel high-impact applications in medicine and manufacturing (drug delivery and particle transport, chemical mixing and *in-situ* contactless manipulation, among many others). Fluid-mediated interactions can then be leveraged to enhance these capabilities or enable new ones [194].

In general flow-mediated interactions play an important role in a number of physical and biological phenomena, from fish schooling [196] and suspension of microorganisms [11, 197] to cloud particle sedimentation [198] and cluster formation [57]. Thus, hydrodynamically-coupled systems have been investigated

[1]This chapter is adapted from the preprint Parthasarathy et al. [193], for which my contributions were implementing the numerical method, running all simulations, analyzing them and being the primary author of the article.

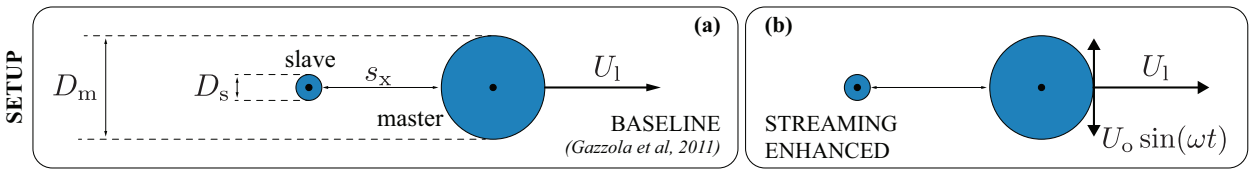

Figure 4.1: System setup: (a) baseline [215] vs. (b) current configuration.

for different flow regimes, including Stokes ($Re \to 0$, [199, 200]), Oseen ($Re \sim O(1)$, [201]) and inviscid ($Re \to \infty$, [202–204]). Moreover, interest in fish schooling also prompted a number of such studies ($Re > 100$, [205–213]) including attempts to bridge viscous and inviscid descriptions [214].

There has been instead little effort in characterizing flow coupling mechanisms in the range $1 \leq Re \leq 100$, typical of the emergent technologies highlighted above [194]. Yet, in this regime, systems of moving objects exhibit rich dynamics characterized by sharp transitions [48, 215, 216], leading to drastically different behaviours (transport vs. non transport, attraction vs. repulsion) depending on the ratio between viscous and inertial effects. Given the sharpness of these transitions, we hypothesize that controlled perturbations or second-order effects such as viscous streaming can be leveraged to shift the boundaries between qualitatively different system responses in a rational, regulated fashion.

In this work we characterize the impact of viscous streaming in the context of passive two- and three-dimensional particle transport by capitalizing on the setup of a previous work [215] (figure 4.1(a)), and drawing inspiration from previous studies [50, 204]. We thus consider the simple yet representative setting of figure 4.1, characterized by a larger cylindrical bot (master) propelling at a constant forward speed and oscillating transversely, and a smaller, passive, trailing cargo (slave). By means of this idealized experiment, we investigate the slave's response, dissect the mechanisms at play and challenge our insights to design master geometries that improve transport.

4.2 Physical framework and streaming definitions

We adopt the setup of figure 4.1(a) with master and slave cylinders of diameter D_m (and radius r_m) and $D_s = \frac{1}{4}D_m$, respectively. The slave is initially at rest, located at a separation distance $0.1D_m$ behind the master, which impulsively starts translating horizontally with a constant speed U_l, spanning $1 \leq Re \leq 100$. We refer to this system setup as the 'baseline' throughout, chosen for its minimal complexity and consistency with prior works [204, 215], thus aiding analysis and comparison. In figure 4.1(b) we superpose to the linear motion of the master a transverse low-amplitude sinusoidal oscillation defined by $y^m(t) = y^m(0) + \epsilon r_m \sin(\omega t)$ with characteristic velocity $U_o = \epsilon \omega r_m$, where ω is the angular frequency and $\epsilon = A/r_m = 0.1$ is the non-

dimensional amplitude (A denotes amplitude). Oscillations elicit a viscous streaming response which can exert small but non-negligible forces, when compared against wake forces (back of the envelope calculations of which are detailed at the end of this section). We claim that this contribution, when properly directed, can significantly alter transport behaviour in a flow regime characterized by sharp transitions [215], through constructive effects between wake and streaming components as hinted to in literature [111].

For reproducibility, we summarize the parameters used henceforth and their values below:

Symbol	Parameter	Value
L_x	Length of the domain along x axis	$1\,\mathrm{m}$
L_y	Length of the domain along y axis	$1\,\mathrm{m}$
Grid size	Grid size along x and y axis	2048
D_m	Diameter of the master	$0.111\,\mathrm{m}$
$\boldsymbol{x}_\mathrm{m}^0$	Initial location of master	$[0.104, 0.5]\,\mathrm{m}$
U_l	Constant lateral velocity of the master	$\lvert D_\mathrm{m}\rvert\,\mathrm{m\,s^{-1}}$
N_m	Average grid points across master	226
D_s	Diameter of the slave	$0.028\,\mathrm{m}$
$s_\mathrm{x}(0)$	Initial separation of slave	$0.011\,\mathrm{m}$
$\boldsymbol{x}_\mathrm{s}^0$	Initial location of slave	$[0.023, 0.5]\,\mathrm{m}$
N_s	Average grid points across slave	56
ρ	Density of fluid, master and slave	$1\,\mathrm{kg/m^3}$

Table 4.1: Physical simulation parameters

We choose the diameters and initial locations for the cylinders to maximize the resolution across both master and slave for a given simulation, for the non-dimensionless end time $T = 2U_\mathrm{l}t/D_\mathrm{m} = 15$.

We characterize the linear motion dynamics by $Re = U_\mathrm{l}D_\mathrm{m}/\nu$ and the oscillatory dynamics by $R_\mathrm{o} = U_\mathrm{o}r_\mathrm{m}/\nu$, where ν is the kinematic viscosity. As usual, streaming dynamics is characterized by the streaming Reynolds number $R_\mathrm{s} = U_\mathrm{o}^2/\omega\nu$. We further define $\zeta = R_\mathrm{o}/Re$ as the non-dimensional quantity that encodes

the relative time scales of oscillatory and linear motion. As our ϵ is fixed, we once again use R_o alone to characterize streaming flows ($R_o = R_s/\epsilon = \epsilon\alpha^2 = \epsilon\omega r_m^2/\nu$). Having introduced the relevant dynamic parameters, we proceed to study the case of figure 4.1(b), through numerical simulations via our method section 3.1, which has been thoroughly validated for fluid–structure interaction [185, 190, 191] and streaming section 3.2 problems.

Estimating the magnitude of streaming-generated forces : We estimate that streaming generated forces for typical parameters are small, but not negligible—varying between $0.1 - 10\%$ of the wake-induced forces. An estimate of relevant forces per unit length induced by fluid flow past a static cylinder is given by $F = \frac{1}{2}C_D(Re)\rho u^2$, the coefficient C_D being a function of only Re [217]. Thus the force contribution from the wake is roughly $F^w = \frac{1}{2}C_D(Re)\rho U_l^2$ while streaming forces contribute forces on the order of $F^s = \frac{1}{2}C_D(R_s)\rho U_s^2$ (the implicit assumption of streaming flow being similar to a free-stream flow is justified as their time–scales are comparable). By definition, we have $U_s = 2\epsilon\zeta U_l$ and thus $R_s = \epsilon\zeta Re$. Then the ratio of these forces couched in terms of ζ and Re for a fixed $\epsilon = 0.1$ is

$$\frac{F^s}{F^w} \sim \frac{0.04\zeta^2 C_D(0.2\zeta Re)}{C_D(Re)}$$

We now consider only $Re = 100$ for the purpose of exposition. With $\zeta = 0.25$ and with $C_D(100) \approx 1.1, C_D(5) \approx 3$ [217], the ratio of forces is $\sim 0.2\%$. Considering a higher streaming intensity characterized by $\zeta = 2$, we have $C_D(40) \approx 1.2$ [217], leading to a force ratio of $\sim 17.4\%$. The order of the streaming forces are thus suspected to be in the range of 0.1–10%, justifying their non-negligible contribution to the system dynamics.

4.3 Transport in two dimensions

We now assess the impact of streaming on slave transport and quantify it by defining the non-dimensional surface-to-surface separation distance $s_x(T)/D_m$ (figure 4.1) in the x direction.

4.3.1 Comparison with baseline

We reproduce the results of the baseline cases of [215] in figure 4.2(a) for clarity. As we increase Re, we observe two distinct, sharp transitions (at $Re \approx 17$ and $Re \approx 82$), between which the slave gets trapped

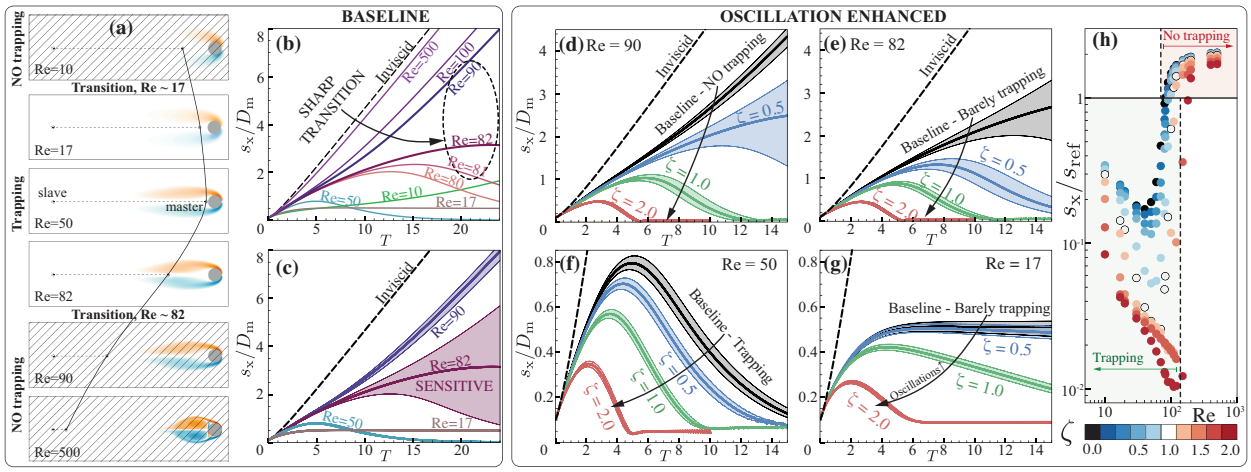

Figure 4.2: Baseline cases: *(a)* We observe a clear range of Re between which trapping and transport is achievable through linear motion. *(b)* Plotting $s_x(t)/D_m$ against $T = 2U_l t/D_m$ reveals that transport is achieved between $Re \approx 17$ and $Re \approx 82$, which then represent transitions between transport and non-transport regimes. At $Re \approx 82$, this transition is sharp (i.e. the system is unstable) and small changes in the Re lead to very different transport responses. *(c)* Perturbing the initial slave location and observing $s_x(t)$ reveals high sensitivity (shaded) of the system around $Re \approx 82$ (the top and bottom envelopes of the shaded region represent the characteristics for slaves with a $\pm 2\%$ perturbation to the initial separation distance). Oscillation enhanced cases: *(d,e,f,g)* enabling oscillations enhances the ability of the system to transport the slave, across different Re. *(h)* We plot s_x/s_{ref} at $T = 10$ for a number of $(Re - \zeta)$ configurations to illustrate how transport–enhancement translates across a wider range of Re.

and transported by the master due to linear motion (and associated wake) alone. This is quantified in figure 4.2(b) across a range of Re, where we plot the normalized master–slave distance s_x/D_m against the non-dimensional time $T = 2U_l t/D_m$. In this plot, a plateauing s_x or $s_x \to 0$ indicates transport and is characteristic of $17 \lessapprox Re \lessapprox 82$. For cases with $Re \lessapprox 17$ and $Re \gtrapprox 82$, s_x increases with time indicating that the slave is left behind as the master moves forward and hence it is not transported. At $Re \approx 17$ and $Re \approx 82$, s_x plateaus with increasing T, indicating that the slave is trapped at a fixed distance from the master (and thus travels with the same speed). These two Re then denote the boundaries of transition between trapping and non-trapping regimes. Moreover, at $Re \approx 82$, this transition is sharp, as small changes in Re (from 80 to 82 to 90) lead to large changes in the transport characteristics. Drawing from prior works [216], we expect the system to be sensitive to changes in the initial master–slave separation $s_x(0)$. We then use this as a proxy to quantify the system sensitivity by perturbing $s_x(0)/D_m$ by $\pm 2\%$ and observing the resulting transport characteristics. We depict this for a few key Re in figure 4.2(c), wherein the shaded regions highlight deviations associated with the perturbation. As expected, the system response is seen to be very sensitive at the transitional $Re \approx 82$, relative to larger and smaller Re. We consider this as an opportunity to enhance transport. Indeed a carefully constructed flow perturbation can *pull* the system from the non-transport regime into the sensitive region and make it *jump over*, enabling transport.

We choose to control the system by perturbing the flow via viscous streaming, by oscillating the master at different levels of intensity $\zeta = R_o/Re$, and report our observations in figure 4.2(d-g). For $Re = 90 > 82$ (above transition, no baseline transport) shown in figure 4.2(d), mild oscillations ($\zeta = 0.5$, blue bands) assist transport and bring the system into the sensitive region. Increasing ζ further pushes the system well beyond the transition, enabling (and quickening) slave transport (green and red bands). Figure 4.2(e-g) shows the oscillation-enabled characteristics for $Re = 82,\ 50$ and 17, where we consistently observe a similar behaviour. We then undertake a parametric investigation to further characterize the effect of superimposing oscillations, systematically spanning Re between 10–500 and ζ between 0–2. We depict this in figure 4.2(h), where we plot s_x/s_{ref} (at $T = 10$) against Re, for different ζ. Here s_{ref} is the separation distance (at the same time $T = 10$) of the reference baseline at $Re \approx 82$, i.e. at the transition between transport and non-transport simulations when oscillations are not active (i.e. $\zeta = 0$). This qualitatively means that cases in figure 4.2(h) with $s_x/s_{ref} < 1$ transport the slave. We then observe that while oscillations always assist transport, higher ζ values are necessary for trapping at higher Re, and beyond $Re \approx 200$ oscillations are no longer able to drive the system into the transport regime, and the slave is then left behind. The system still retains its inherent sensitivity to Re, apparent from the sharp jump between trapping/non-trapping cases across $100 \lessapprox Re \lessapprox 200$, for any fixed ζ. We conclude that introducing oscillations, modulated by ζ, enhances inertial particle transport across a wide range of Re. The causal mechanism, be it viscous streaming or other wake-oscillation interactions, is ascertained in the next sections.

Before probing further for the causal mechanism, we first diagnose whether the leading order effect is indeed viscous in nature, and not an inviscid mechanism. To this extent, we investigate the transport characteristics arising from inviscid effects of the translation–oscillation strategy using a potential-flow boundary-element solver (detailed in the Appendix). We show these characteristics in figure 4.3(a), for various ζ. The system is initially insensitive to oscillations (and thus to perturbations in initial positions), while at high (> 5) ζ we are able to trap and transport the slave due to potential effects alone. We realize that while the primary transport enhancement mechanism observed in our studies can not be attributed to inviscid interactions, these effects are non-negligible at higher ζ values. This is reflected in the viscous transport characteristics as well—at $Re = 500$ (with behavior close to inviscid, seen from the baseline of figure 4.2(b)), we see insensitivity to changes in ζ in figure 4.3(b). Comparing this to the characteristics of $Re = 90$, shown in the same figure, clearly indicates the moderating effect of viscosity (via both wake and oscillation-related mechanisms) in transport of inertial particles.

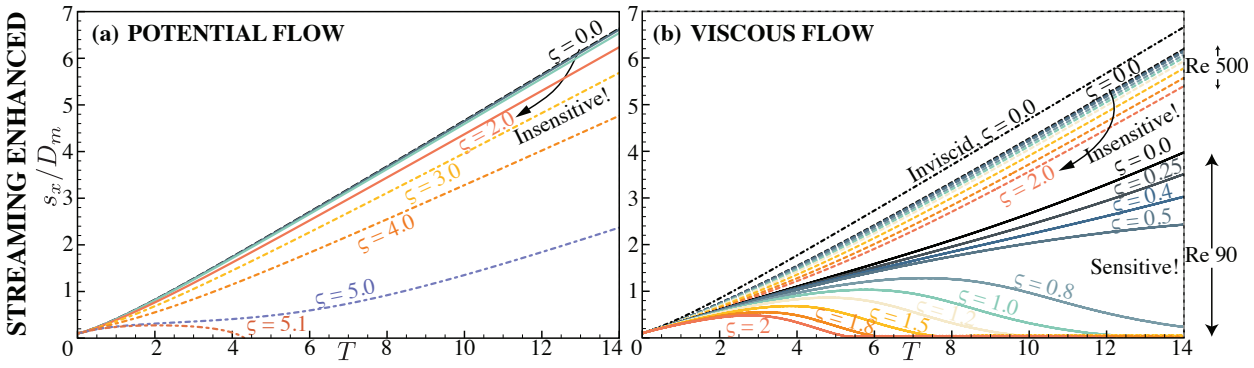

Figure 4.3: Streaming enhanced transport: (a) Enhancement in transport from pure potential effects is minimal and high ($\zeta \to 5$) values are required for trapping, while enhancement in the (b) viscous case is appreciably more for finite Re.

4.3.2 Robustness

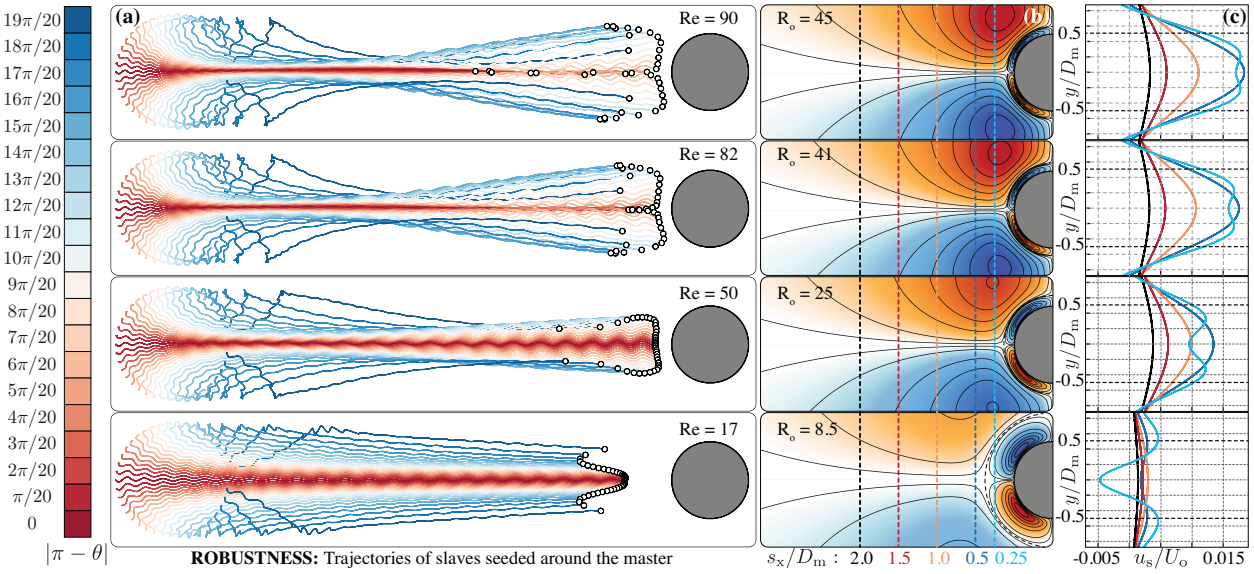

ROBUSTNESS: Trajectories of slaves seeded around the master

Figure 4.4: Robustness: (a) Seeding slaves azimuthally around the master (with $\zeta = 0.5$) and plotting their trajectories (till $T = 14$) reveals that all slaves get transported for different $Re \in [17, 82]$, lending to the robustness of this transport enhancement strategy. The trajectories can be correlated to (b) the associated pure streaming fields (colored by streamfunction with the solid lines indicating streamlines). Dashed lines indicate different stations at which we plot (c) streaming-induced velocities. We do not consider slaves in the comparison against pure streaming fields, with the implicit assumption that they do not drastically perturb the flow.

Given the sensitivity of the system, seen in figure 4.2(c), to initial horizontal slave separation, it is important to further characterize the spatial robustness of the proposed transport strategy. Increasing ζ aids transport, but so far we tested only slaves initially located directly behind the master (figure 4.2(h)). We then initialize slaves (diameter $D_s = \frac{1}{4}D_m$) at the same surface-to-surface distance ($0.1D_m$), but at different

azimuthal positions θ around the master, in separate simulations. We choose a representative $\zeta = 0.5$ and vary only the Re. Figure 4.4(a) illustrates the slave trajectories at $T = 14$ for representative Re, colored by their initial azimuthal position. We observe that almost all slaves get transported, irrespective of their initial azimuthal positions (and initial radial position perturbations, shown at the end of the section). However we notice differences between the slave trajectories at different Re.

These differences can be comprehended by analyzing the corresponding pure streaming (figure 4.4(b,c)) flow fields. Figure 4.4(b) shows the time-averaged streamlines, where we also depict the stations at which the corresponding streaming velocities (figure 4.4(c)) are portrayed. At $Re = 17$, a thicker DC layer (with reverse flow, blue line in figure 4.4(c)) *cushions* the master and prevents the slaves from attaining close proximity. All the other cases have a DC layer of almost constant thickness, thus lending to qualitative differences, highlighted by slaves closely surrounding the master's posterior. Comparing $Re = 50$ and $Re = 82$, we notice that in the latter slaves with initial positions $|\pi - \theta| \gtrsim 15\pi/20$ (figure 4.4(a), colorbar) are transported further, due to more favourable upstream velocity profiles. Additionally, slaves almost directly behind the master (with initial positions $|\pi - \theta| \lesssim \pi/5$) trail for $Re = 90$ as compared to $Re = 82$ and $Re = 50$. This is explained by the fact that $Re = 90$ is characterized by a baseline that cannot trap. Mild oscillations ($\zeta = 0.5$) are then just barely capable of *pulling* the slaves close enough to be trapped and transported. We conclude that oscillation-based transport strategy is robust overall. Moreover the resulting slave trajectories are found to be consistent with streaming-induced velocities, suggesting that this is the responsible transport enhancement mechanism at play.

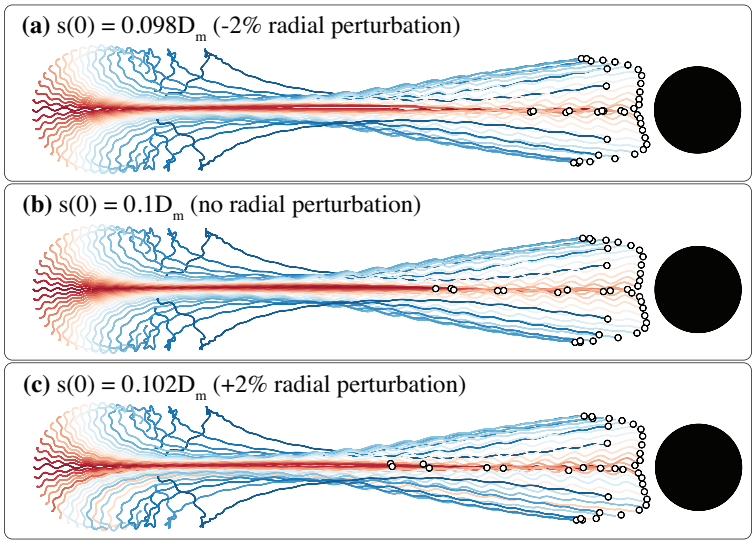

Figure 4.5: Robustness of the streaming strategy to changes in the initial radial positions of seeded slaves, shown for cases with $(a)-2\%$, (b) no and (c) 2% perturbation at $Re = 90, \zeta = 0.5$.

To demonstrate robustness to perturbations in the radial direction we consider the same setup, restricting the investigation to $Re = 90, \zeta = 0.5$ while adding a $\pm 2\%$ (radial) perturbation in the initial surface–surface distance between the master and the slave. The results are shown in figure 4.5, which demonstrates robustness to radial perturbations. The only significant difference is seen in the trajectories of cases with $|\pi - \theta| \lesssim \pi/5$, due to the transitional nature of the baseline.

4.3.3 Flow analysis at the transport/non-transport boundary

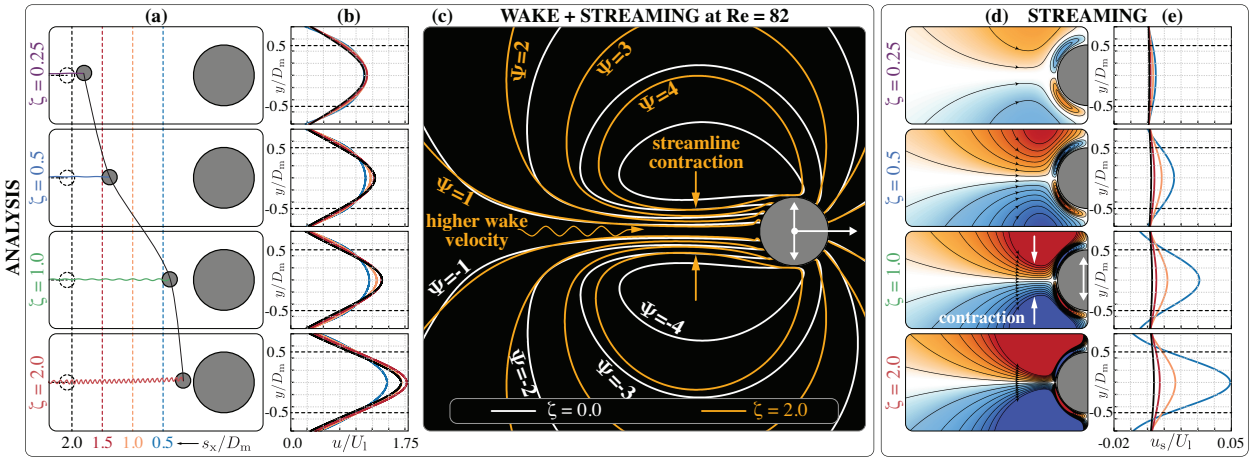

Figure 4.6: Analysis: Fixing $Re = 82$ and increasing ζ leads to (a) better transport due to flow acceleration in the wake. The trajectories are drawn till $T = 14$ with the dashed black lines representing the baseline case. (b) Time-averaged velocity profiles (over 20 oscillation cycles) at the marked stations of (a). The observed accelerations are due to streamline-contraction in the wake, visualized in (c) for representative cases without $(\zeta = 0$, white streamlines) and with $(\zeta = 2$, orange streamlines) streaming. Corresponding streaming-only fields—(d) streamlines and (e) velocities at the same stations as (a,b)—explain the behaviour of (a,b,c).

Here, we further focus on the fluid mechanisms at play, by drawing parallels between the system at the transitional $Re = 82$ with different ζ and corresponding pure streaming cases. Figure 4.6(a) pictures the slave trajectories for increasing ζ, highlighting improvement in transport. This is due to a corresponding increase in the wake velocities as seen in figure 4.6(b), where we plot the time-averaged velocities, at the different stations marked in figure 4.6(a). The averaged streamlines (streamfunction iso-contours) of figure 4.6(c) for cases with $(\zeta = 2)$ and without $(\zeta = 0)$ oscillations explain this increase in wake velocity. Oscillations *tilt* the streamlines backwards, simultaneously compressing them directly behind the master, thus locally increasing upstream flow velocities. The degree of this contraction increases with ζ. This behaviour is consistent with the corresponding streaming-only patterns of figure 4.6(d) where larger oscillation intensities increasingly push the outer eddies towards the mid-plane, causing streamline contraction and increasing flow velocities,

as further quantified in figure 4.6(e). We thus identify streamline contraction as the primary cause for transport enhancement, with the viscous streaming mechanism driving this contraction.

4.3.4 Design

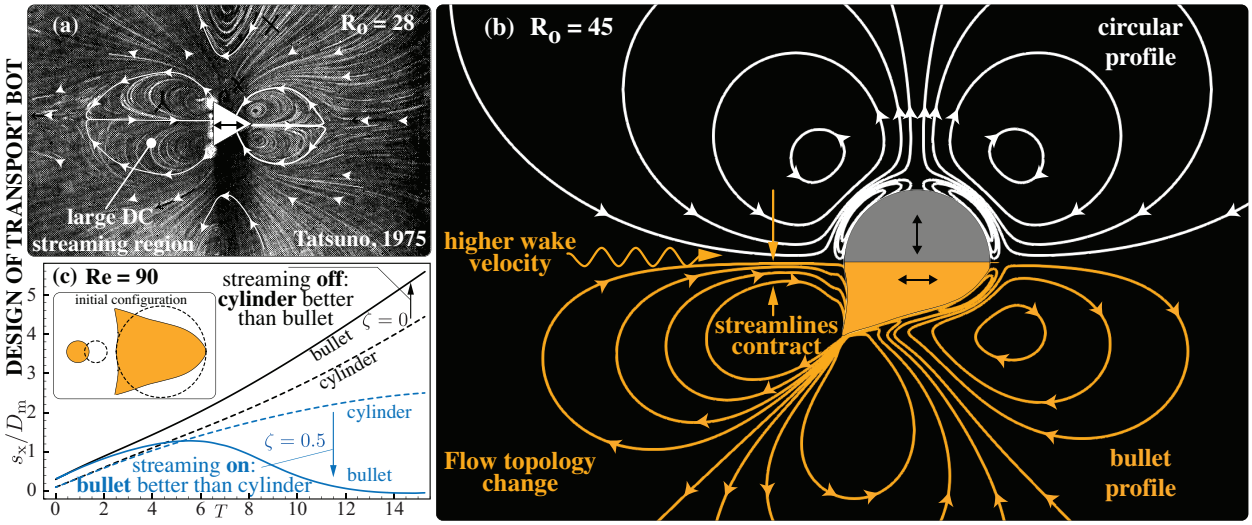

Figure 4.7: Design: (a) Inspired by streaming from triangles [55], we design the 'bullet' shape of (b) to induce a more favourable streaming field (more streamline contraction at $R_o = 45$) which is reflected in better (c) transport characteristics (at $Re = 90$) relative to a simple circular cylinder. This is in spite of our initial configuration (inset) that penalizes the bullet by placing the slave further away.

If streaming is indeed the responsible agent for transport enhancement, we should be able to design new geometries that produce more favourable streaming fields that actually translate in improved slave transport once tested in our setup of figure 4.1(b). We start by considering streaming only, and draw inspiration from the visual investigation of Tatsuno [55] on streaming triangles. These are shown to produce a large DC recirculation region (figure 4.7(a)), which can be leveraged to trap and carry along passive cargoes. We then 'borrow' two key components of this geometry—rear high-curvature tips and fore-aft symmetry breaking—to design a master with a 'bullet' cross-section (figure 4.7(c), inset—refer to the Appendix for shape parametrization). This geometry is chosen to facilitate its comparison with the circular cylinder. Additionally, consistent with Tatsuno [55] and differently from our calculations prior to this section, we change the direction of oscillation, from transverse (vertical) to longitudinal (horizontal), to produce the large posterior DC streaming layer observed in figure 4.7(a). In figure 4.7(b), we show that our new design constricts the streamlines further than a transversely-oscillating circle. This is reflected in its transport characteristics (figure 4.7(c)): while the circular cylinder performs better than the bullet when streaming is not active (no oscillations, pure master linear motion), the bullet outperforms its circular counterpart when

streaming is enabled, even for mild oscillation intensities ($\zeta = 0.5$).

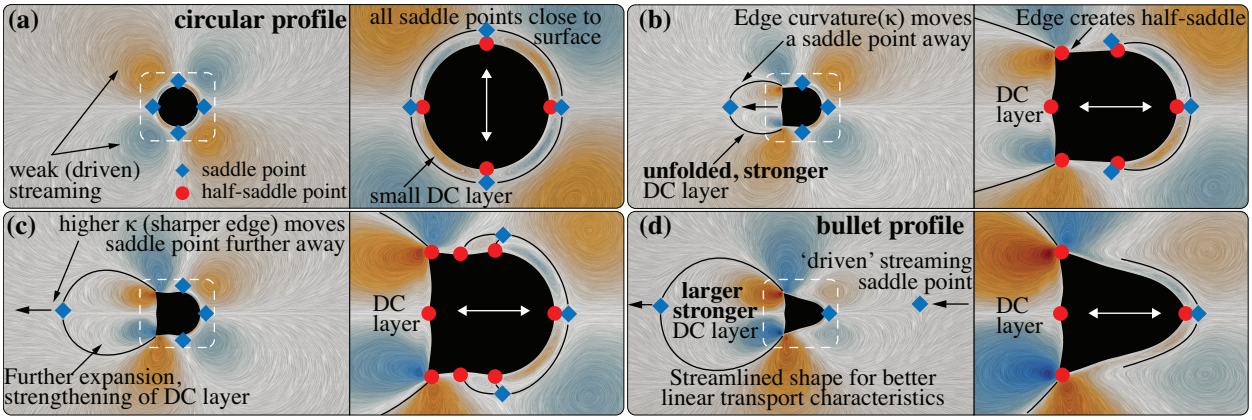

Figure 4.8: Topology: We study the flow topological response to incremental shape changes (from the *(a)* circle to the *(d)* bullet) via Line Integral Convolution (LIC) of the streaming velocity field at $R_o = 45$. This reveals a route for the rational design of streaming-based transport devices. The key idea involves introducing rear high-curvature points and fore-aft symmetry breaking to enlarge/strengthen DC layer streaming, the extent of which is indicated by the saddle points and marked by solid black lines. *(b,c)* are intermediate shapes that illustrate the process.

The reason for the increased streamline contraction above lies in the flow topology change associated with the introduction of multiple curvatures and asymmetry in the master geometry (figure 4.7(b)). To understand how this topological transition occurs, we progressively morph (figure 4.8) the circular cylinder into the bullet, and track the behaviour of critical points in the flow (these are saddle and half-saddle points [218], which are sparse yet complete representations of the global field [219]). In the context of streaming, saddle points indicate the physical extent of the DC layer, marked by solid black lines in figure 4.8. Morphing may create, destroy, merge or displace saddle and half-saddle points, which we leverage to manipulate the DC layer. Introducing high rear curvature points to the circle in figure 4.8(b) creates two new half-saddles, which allows the rear saddle point to move away from the surface, thus 'unfolding' the DC layer. The extent of this offset and the corresponding strength of the DC streaming region is related to the magnitude of the tip curvature. This is seen in figure 4.8(c) where tip curvature increase enlarges the DC layer. Streamlining the master geometry further strengthens the DC layer and gives rise to our final bullet design shown in figure 4.7(d). Thus by manipulating the shape (and the oscillation direction) of the master—which dictates the streaming flow topological response—we can rationally design configurations that improve slave transport.

In this chapter, we have shown that oscillations can be utilized to robustly improve transport in an idealized two-dimensional master–slave setting across $1 \leq Re \leq 100$. The analysis of flow features identifies viscous

streaming as the catalyst for this improvement. Leveraging this information, we designed geometries exhibiting more favourable streaming patterns, which resulted in improved slave transport. To that extent, we demonstrated a rational design approach by modifying the classic circular cylinder via the introduction of multiple curvatures and fore-aft symmetry breaking. We have thus highlighted viscous streaming as a robust mechanism for achieving flow and passive particle control in a regime associated with emerging miniaturized robotic applications, such as, for example, drug delivery.

Chapter 5

Conclusions

The primary focus of this work was to establish viscous streaming as a viable mechanism to effect transport, mixing and even locomotion in a complicated and uncertain fluid environment across a range of scales. Previous works in this field have been predominantly experimental (or) theoretical and have focused on streaming in simplified settings—mostly from an individual circular cylinder. While experiments involving complex streaming settings have been plentiful and successful, they are usually either (i) limited in their analysis of the fundamental streaming mechanism or (ii) have limited applicability in terms of their utility (or) scale of operation (or) underlying assumptions (or) turnaround times. Numerics, being the other alternative, has so far fallen short in this goal because of the complexity associated with capturing the second-order, long time-scale streaming effect. In this context, we

- Established numerical FSI simulations based on RVM as a reliable tool to capture streaming dynamics. This included streaming from arbitrary shapes in different dynamic regimes, from multitudes and even from actuations that are hard to achieve experimentally (or) analyze theoretically. An extension to KC flows was also presented in the premise of attaining distinct yet regulated fluidic responses in a logical manner.

- Developed an array of tools to analyze the flows simulated by our algorithm above. This included relating our results back to asymptotic theory, correlating and contrasting simulations of different dynamical setups, analyzing flow properties (velocity, streamfunction and particle trace fields), flow topology and preliminary mode decompositions (DMD/POD) of flow data.

- Demonstrated the utility of streaming in the transport of passive inertial objects in the flow robustly across $Re \in \mathcal{O}(1) - \mathcal{O}(100)$, despite the presence of other wake effects and in spite of its second-order nature. This was achieved by correlating transport and pure streaming flow fields, across many settings.

- Rationally designed geometries capable of improving inertial particle transport by modifying body curvature and breaking symmetry, armed with insights gained from the prior steps.

5.1 Perspectives

Potential avenues for future work are listed below, concerning numerics, physics and applications of streaming.

- *Curvature*: While we have shown the extent to which *curvature modifies streaming*, the fundamental causal mechanism remains elusive and needs to be the focus of a detailed study.
- *3-D effects*: How do *three-dimensional effects* affect streaming? While streaming from simple shapes such as a sphere have been the subject of intense scrutiny, more complex shapes (such as a torus—a different entity from both a geometric and topological perspective) have not been paid attention to.
- *Multitudes*: How can we constructively leverage streaming generated by the oscillations of *multiple bodies*? Can we *design* streaming–mazes and guide particles along it?
- *Actuation*: Biological organisms, such as the *starfish larvae*, seem to utilize streaming generated from a complicated, *multi-modal actuation* of their cilia. Can this process be understood, much less channeled towards engineering applications?
- *Scaling*: Is there a possibility of *scaling* streaming and KC flows logically by the same non-dimensional parameter set? Indeed from the phase space of figure 3.8, several regimes demonstrate common features indicating a shared time and length scale parameter. While we explored this aspect in a different study [220], more work needs to be done.
- *Analysis*: Are there better *numerical/data-driven tools for analysis* of such streaming (and even KC) flows to help us better understand these systems? We attempted to decompose the data using POD/DMD (not shown in the thesis), but this works only for pure streaming flows. Streaming flows with other effects (say shear layers) have entangled time- and length-scales, making the results produced by such data driven tools non-intuitive. Furthermore higher amplitude oscillations (encountered frequently in KC flows) in an Eulerian–immersed boundary framework, such as our method, frequently corrupts the flow-data next to the solid boundaries. This leads to unphysical flow artifacts.
- *Inverse-design*: Can we *coherently engineer* streaming configurations (with multitudes of arbitrarily shaped oscillating objects) to optimally achieve a series of tasks at the micro-scale, say mixing (or) separating (or) transport of scalar species? This involves embedding our FSI framework into an inverse-design cycle, an approach which has enjoyed success in the past across many configurations [190, 191, 212, 221, 222].

- *Better solvers*: To entertain the possibility of integrating our FSI framework into an inverse-design cycle, we need *faster yet accurate simulations*, to simulate $\sim \mathcal{O}(1000)$ cycles efficiently. This calls for improved FSI algorithms based on vortex methods (shown to succesfully capture streaming), such as [223], which may necessitate higher-order (accurate) solvers.

- *Stokes solvers*: The utility of streaming is expected to be immense in the characteristically linear Stokes regime. This calls for efficient, optimal (in terms of algorithmic complexity), robust, scalable and higher-order accurate solvers for the *Stokes PDE*.

Appendix A

Appendix

A.1 Two dimensional inviscid flow mediated interactions–Algorithm

We discuss the numerical strategy used for the potential flow simulations used in transport and validate it against two benchmark problems. We once again consider two-dimensional incompressible flow in an unbounded domain (Σ), in which n moving rigid bodies are immersed. We denote with Ω_i & $\partial\Omega_i$, $i = 1, \cdots n$ the support and boundaries of the solids, which are assumed to be of the same density of the fluid ($\rho_i = \rho = 1\,\mathrm{kg/m^3}$). We further define $\partial\Omega := \bigcup_{i=1}^{n} \partial\Omega_i$. The definitions and symbols used to present the RVM algorithm in the main text are also adopted here. The algorithm presented below is the same as [224], with minor modifications to simulate our master–slave cylinder pairs.

A.1.1 Governing equations

The governing equations for the fluid in the inviscid limit are the Euler equations coupled with the incompressibility constraint:

$$\frac{\partial \boldsymbol{u}}{\partial t} + (\boldsymbol{u} \cdot \boldsymbol{\nabla})\,\boldsymbol{u} = -\frac{1}{\rho}\nabla P \qquad \boldsymbol{x} \in \Sigma \setminus \Omega \tag{A.1}$$

$$\boldsymbol{\nabla} \cdot \boldsymbol{u} = 0 \qquad \boldsymbol{x} \in \Sigma \setminus \Omega \tag{A.2}$$

The rigid solid body dynamics can be obtained by solving the Newton's equations of motion concurrently:

$$m_i \ddot{\boldsymbol{x}}_i = \boldsymbol{F}_i^H \tag{A.3}$$

$$\frac{d(I_i \dot{\theta}_i)}{dt} = \boldsymbol{M}_i^H \tag{A.4}$$

The causal force and moments in equations (A.3) and (A.4) on the body result from the boundary conditions that couple the fluid–solid dynamics:

$$\boldsymbol{u} \cdot \boldsymbol{n}(\boldsymbol{x}) = \boldsymbol{u}_i \cdot \boldsymbol{n}(\boldsymbol{x}) \qquad \boldsymbol{x} \in \partial\Omega_i \tag{A.5}$$

where $\boldsymbol{n}$ is the unit normal pointing towards the fluid and $\boldsymbol{u_i}$ is the velocity of the rigid body i, respectively. This encodes the no-through flow boundary condition.

To solve the above problem numerically we encompass the solids and fluid system into an larger one and solve for the total dynamics. This bypasses the need to calculate pressure and surface forces on the body as they are internal forces in the bigger system. As shown by Lamb [225], one can adopt a Lagrangian perspective and solve for the total dynamics using the principle of minimal work, resulting in Euler–Lagrange equations. The dynamics (an initial value problem) then evolve in time according to the coupling between the solids and fluid (a boundary value problem). For the purpose of exposition we focus first on this coupling and then on evolving the system in time.

The idea is to simplify the non-linear problem, given in equation (A.1), in the absence of initial ($t = 0$) vorticity using Helmholtz's theorem—which guarantees that vorticity remains absent in the flow at all times $t > 0$. We can then represent the conservative velocity vector as the gradient of a scalar potential function $\phi(\boldsymbol{x})$, i.e. $\nabla\phi(\boldsymbol{x}) = \boldsymbol{u}(\boldsymbol{x})$. As the velocity vector is always solenoidal (from equation (A.2))—the problem of solving equations (A.1) and (A.2) is equivalently cast to solving the following Laplace equation.

$$\nabla^2\phi(\boldsymbol{x}) = 0 \qquad \boldsymbol{x} \in \Sigma \setminus \Omega \tag{A.6}$$

with the boundary conditions

$$\nabla\phi(\boldsymbol{x}) \cdot \boldsymbol{n}(\boldsymbol{x}) = (\boldsymbol{u}_i + \dot{\theta}_i \times (\boldsymbol{x} - \boldsymbol{x}_i) \cdot \boldsymbol{n}(\boldsymbol{x}), \qquad \boldsymbol{x} \in \partial\Omega_i \tag{A.7}$$

$$\nabla\phi(\boldsymbol{x}) = 0, \qquad \boldsymbol{x} \to \infty \tag{A.8}$$

where $\dot{\theta}_i, \boldsymbol{x}_i$ represent the angular velocity and the center of the rigid body i. We thus solve an exterior Neumann Boundary Value Problem (NBVP), with equation (A.8) necessitating the flow decay at large distances. Following [225], we decompose the potential field $\phi(\boldsymbol{x})$ into elementary Kirchhoff potentials

$\mathcal{X}_i(\boldsymbol{x})$, $\boldsymbol{\varphi_i}(\boldsymbol{x})$ such that

$$\phi(\boldsymbol{x}) = \sum_{i=1}^{n} (\dot{\theta}_i \cdot \mathcal{X}_i(\boldsymbol{x}) + \boldsymbol{u}_i \cdot \boldsymbol{\varphi_i}(\boldsymbol{x})) \tag{A.9}$$

While this linear decomposition increases the algorithmic complexity of the problem, it enables us to separate the individual contribution from every rigid body velocity component in the flow. This is useful in calculating the added mass contributions resulting from the adjacent fluid being accelerated by the motion of the immersed solid bodies. The inertia (or) the mass matrix for the system $\mathbf{M}$ thus consists of the solid body inertia and added mass (fluid) contributions. $\mathbf{M}$ is a block matrix with the blocks $\mathbf{M}_{ij}$ given by

$$\mathbf{M}_{ij} = \begin{bmatrix} \int_{\Sigma\setminus\Omega} \nabla\mathcal{X}_i \cdot \nabla\mathcal{X}_j & \int_{\Sigma\setminus\Omega} \nabla\mathcal{X}_i \cdot \nabla\varphi_j^1 & \int_{\Sigma\setminus\Omega} \nabla\mathcal{X}_i \cdot \nabla\varphi_j^2 \\ \int_{\Sigma\setminus\Omega} \nabla\varphi_i^1 \cdot \nabla\mathcal{X}_j & \int_{\Sigma\setminus\Omega} \nabla\varphi_i^1 \cdot \nabla\varphi_j^1 & \int_{\Sigma\setminus\Omega} \nabla\varphi_i^1 \cdot \nabla\varphi_j^2 \\ \int_{\Sigma\setminus\Omega} \nabla\varphi_i^2 \cdot \nabla\mathcal{X}_j & \int_{\Sigma\setminus\Omega} \nabla\varphi_i^2 \cdot \nabla\varphi_j^1 & \int_{\Sigma\setminus\Omega} \nabla\varphi_i^2 \cdot \nabla\varphi_j^2 \end{bmatrix} + \begin{bmatrix} I_j\delta_{ij} & 0 & 0 \\ 0 & m_j\delta_{ij} & 0 \\ 0 & 0 & m_j\delta_{ij} \end{bmatrix} \tag{A.10}$$

where $i, j \in \{1, \cdots, n\}$ represent the i^{th} and j^{th} body contributions, $\boldsymbol{\varphi}$ has $[\varphi^1, \varphi^2]$ as its components, δ_{ij} represents the Kronecker-delta function and the $\boldsymbol{x}$ dependence on the integrands is implicit. This block captures the total finite inertia resulting from the presence and motion of both the moving bodies i, j and the fluid surrounding them, thus rendering it important for the collective dynamics of the system.

This dynamics evolve according to the Euler–Lagrange formula, where we consider the total system energy functional as the Lagrangian function to minimize. The kinematic energy of the i^{th} solid body is $K_i = \frac{1}{2}m_i|\boldsymbol{u}_i|^2 + \frac{1}{2}I_i\dot{\theta}_i^2$. The total kinematic energy of the fluid is $K_f = \frac{1}{2}\rho\int_{\Sigma\setminus\Omega_i} |\nabla\phi|^2(\boldsymbol{x})d\boldsymbol{x}$. In this work we do not consider conservative barotropic forces and so the potential energy contribution is identically zero. The total system energy functional is thus $L(\boldsymbol{q}, \dot{\boldsymbol{q}}) = K_f + K_1 + K_2 = \frac{1}{2}\dot{\boldsymbol{q}}^T\mathbf{M}(\boldsymbol{q})\dot{\boldsymbol{q}}$—a function of the state $\boldsymbol{q}$ and its derivative $\dot{\boldsymbol{q}}$. Here $\boldsymbol{q}$ represents the degrees of freedom for the system i.e. the angular and Cartesian positions of all the bodies (i.e. $\boldsymbol{q} = [\boldsymbol{q}_1, \cdots, \boldsymbol{q}_n]$ with $\boldsymbol{q}_i = [\theta_i \quad x_i^1 \quad x_i^2], i \in \{1, \cdots, n\}$). Using this Lagrangian function L we derive the Euler Lagrange equation for the state $\boldsymbol{q}$

$$\frac{d}{dt}\frac{\partial L}{\partial \dot{\boldsymbol{q}}} - \frac{\partial L}{\partial \boldsymbol{q}} = 0 \tag{A.11}$$

which equivalently results in

$$\mathbf{M}\ddot{\boldsymbol{q}} + \langle\, (\boldsymbol{q}), \dot{\boldsymbol{q}}, \dot{\boldsymbol{q}}\rangle = 0 \tag{A.12}$$

where $(\boldsymbol{q})$ is a rank-3 tensor identified as the Christoffel symbol [224] and $\langle\, (\boldsymbol{q}), \dot{\boldsymbol{q}}, \dot{\boldsymbol{q}}\rangle$ is shorthand for $(\boldsymbol{q})^k_{ij}\dot{q}_j\dot{q}_k$. If M_{ij} denotes the (i, j) entry of $\mathbf{M}$ $(i, j \in \{1, \cdots, 3n\})$ and q_i denotes the entries of $\boldsymbol{q}$ $(i \in$

$\{1, \cdots, 3n\}$), then we define the Christoffel symbol Γ^k_{ij} by

$$\Gamma^k_{ij} = \frac{1}{2}\left(\frac{\partial M_{ki}}{\partial q_j} + \frac{\partial M_{kj}}{\partial q_i} - \frac{\partial M_{ij}}{\partial q_k}\right) \tag{A.13}$$

These 'shape derivative' $\frac{\partial M}{\partial q}$ terms are calculated efficiently according to the formulation in Munnier and Pinçon [224]. With all the above manipulations that follow from [202, 224, 225], we have reduced the governing nonlinear PDEs (A.1,A.2) to a system of nonlinear ODEs (A.12) which can be integrated efficiently in time.

A.1.2 Representation

To solve the NBVP equations (A.6), (A.7) and (A.8) at every timestep, we use Boundary Element Methods (BEMs) based on integral formulations of the Laplace equation. BEMs for the Laplace equation only need to be discretized on the surface—making them fast and efficient—thus eluding the problem of remeshing at every time step. The conversion of equations (A.6) to (A.8), to a formulation convenient for BEM is carried out by using Green's theorem, that reduces all volume integrals in equation (A.10) to surface integrals:

$$\int_{\Sigma\setminus\Omega} \nabla\mathcal{T}_i \cdot \nabla\mathcal{T}_j d\boldsymbol{x} = \tfrac{1}{2}\int_{\partial\Omega_j} \mathcal{T}_i \partial_{\boldsymbol{n}}\mathcal{T}_j d\sigma_j + \tfrac{1}{2}\int_{\partial\Omega_i} \mathcal{T}_j \partial_{\boldsymbol{n}}\mathcal{T}_i d\sigma_i \tag{A.14}$$

where $\mathcal{T}$ is a proxy for any of $\mathcal{X}, \varphi^1, \varphi^2$. Having transformed the volume Laplace problem to the equivalent boundary integral form, we realize that we only need the elementary Kirchhoff potentials on the boundaries $\partial\Omega_i$ (that is the Dirichlet data), given its normal derivatives (the Neumann data, from equation (A.7)). We then represent, discretize and solve for $\mathcal{T}$ on the boundaries only. The representation of elementary potentials of body i is done using finite terms (with cardinality m) of a Fourier series on $\partial\Omega_i$—the choice of the basis reflects the compact support and periodicity (with period 2π) of $\partial\Omega_i$.

We obtain the Dirichlet data (and its tangential derivatives) on the boundary using the Neumann-to-Dirichlet operator [226] for the 2D Laplace kernel $G(\boldsymbol{x}, \boldsymbol{y}) = \frac{1}{2\pi}\int_{\partial\Omega_i} \log|\boldsymbol{x} - \boldsymbol{y}| d\sigma_{\boldsymbol{y}}$. This reads for $i \in \{1, \cdots n\}$ and $\boldsymbol{x} \in \partial\Omega$

$$\mathcal{T}_i(\boldsymbol{x}) - \frac{1}{\pi}\int_{\partial\Omega} \frac{(\boldsymbol{y}-\boldsymbol{x})}{|\boldsymbol{y}-\boldsymbol{x}|^2} \cdot \boldsymbol{n}(\boldsymbol{y})\mathcal{T}_i(\boldsymbol{y}) d\sigma_{\boldsymbol{y}} = -\frac{1}{\pi}\int_{\partial\Omega_i} \log|\boldsymbol{y}-\boldsymbol{x}| N_i(\boldsymbol{y}) d\sigma_{\boldsymbol{y}} \tag{A.15}$$

where we have prescribed $N_i(\boldsymbol{y})$—the Neumann data from equation (A.7). The tangential derivatives of $\mathcal{T}_i$ are necessary to calculate the shape derivatives. This is trivially done as once $\mathcal{T}_i \in C^\infty$ is known, we can take its derivative in the tangential direction efficiently by using the spectral equivalent of the standard

differentiation operator.

A.1.3 Discretization

To solve the integral equation (A.15), we use Nyström discretization coupled with the (spectrally accurate) trapezoidal quadrature rule. To numerically evaluate the integrals, we split the integrand into singular and non-singular contributions and use the scheme suggested in Atkinson [226] to evaluate the former—the latter is trivial to integrate numerically. The interested reader is referred to Atkinson [226] for the theoretical and Munnier and Pinçon [224] for the implementation details. We discretize the boundary $\partial\omega_i$ by $\upsilon_i = 2m_i + 1$ points, where m_i is the finite number of Fourier modes represented on the boundary. We represent equation (A.15) in the discrete form by the equation $\mathbf{A}\boldsymbol{t} = \boldsymbol{r}$, where $\boldsymbol{t}, \boldsymbol{r}$ are the discrete equivalents of $\mathcal{T}$ and the right hand side being solved for. We factorize $\mathbf{A}$ by standard LU-decomposition for the reasons listed in Munnier and Pinçon [224]. Having evaluated the elementary potential on $\partial\Omega_i$, we proceed to evaluate the mass matrix (A.10) and the Christoffel symbols $\boldsymbol{\Gamma}$ (A.13) at these boundaries. The acceleration in equation (A.12) is then evaluated and the whole system can be marched forward in time.

We now deal with the time-marching scheme used in solving equation (A.12), which we rewrite as

$$\frac{d}{dt}\begin{bmatrix} \dot{\boldsymbol{q}} \\ \\ \boldsymbol{q} \end{bmatrix} = \begin{bmatrix} -\mathbf{M}^{-1}\langle\, (\boldsymbol{q}), \dot{\boldsymbol{q}}, \dot{\boldsymbol{q}}\rangle \\ \\ \dot{\boldsymbol{q}} \end{bmatrix} \tag{A.16}$$

As the boundaries of the solids $\partial\Omega$ are assumed to be infinitely differentiable C^∞, parametrized with respect to a boundary tangent variable $t \in [0, 2\pi]$, we can infer that the RHS is then also C^∞. The above problem is then well posed and infinitely differentiable in time—making it a candidate for higher-order time stepping schemes. We use the `LSODA` function from `ODEPACK` that uses upto 13^{th} order accurate non-stiff (Adams) or stiff (BDF) method adaptively based on the data. We fix the absolute and relative tolerances of our ODE solver to 1.49×10^{-8}, unless stated otherwise.

A.1.4 Validation

Here we consider two validation cases for our algorithm. The first benchmark case is the slave (radius b) motion due to pure sinusoidal oscillations of the master (radius a) in one direction, wherein we have a closed form governing ODE at large master–slave distances [202] for an inertialess master–slave pair. The slave transport is then purely due to the added-mass terms arising from the presence of the intermediate fluid. The nonlinear analytical ODE governing the slave position x_s for the case with $a = b = \frac{1}{\sqrt{2}}$ m, $\rho = \frac{1}{\pi}$ kg/m^3

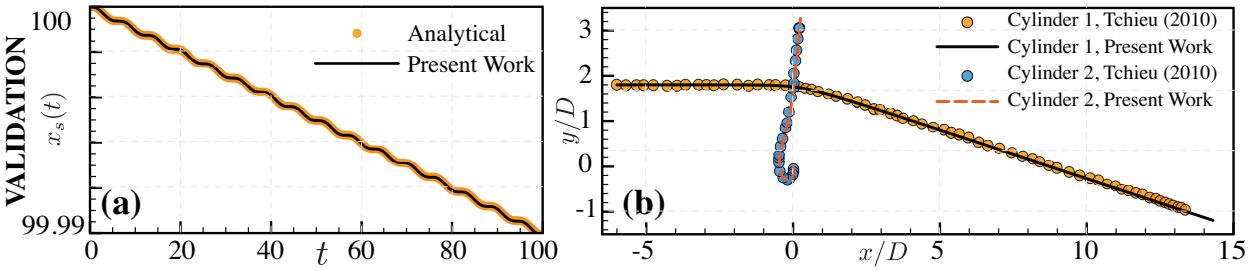

Figure A.1: Validation for the potential flow solver: *(a)* against a purely oscillating master–slave configuration and *(b)* against a near-collision event of two free cylinders

and for pure sinusoidal oscillations of the master $x_{\mathrm{m}} = \sin(t)$ is

$$\ddot{x}_{\mathrm{s}} = -\frac{\sin t}{(x_{\mathrm{s}} - \sin t)^2} + \frac{2\cos^2 t}{(x_{\mathrm{s}} - \sin t)^3} \tag{A.17}$$

We now consider the same setup in our numerical solver using $\upsilon_i = 121$ points or $m_i = 60$ modes spatially on each cylinder (of density $\rho = 1 \times 10^{-8} \sim 0$ each) and step forward in time with a constant $\Delta t = 0.002$s. The result from the solution of the closed form nonlinear ODE equation (A.17) and our numerical solution, for an impulsively started master, is shown in figure A.1(a). Our result matches the analytical result closely.

The second benchmark case is derived from Tchieu et al. [204] and considers the near collision event of two *free/passive* cylinders in the flow. In this case, two neutrally buoyant ($\rho_i = \rho = 1$ kg m^{-3}) cylinders, of diameter 1 m each are initially placed in the cartesian plane at $\boldsymbol{x}_1 = [-6.0 \quad 1.8]^T$ and $\boldsymbol{x}_2 = [0.0 \quad 0.0]^T$ respectively. The former is given an initial velocity of $\dot{\boldsymbol{x}}_1(0) = [1.0 \quad 0.0]^T$. It is noted that in the absence of the fluid both the cylinders will collide. The presence of the fluid acts as a *cushion*, and helps prevent collision between the cylinders. The cylinders then nearly kiss one another—and any singular effects associated with the near-contact event need to be well resolved, making this a rigorous benchmark. We simulate this setup with our algorithm for $\upsilon_i = 121$ points each on the cylinders and with a constant $\Delta t = 0.002$s. The computed trajectory for both the cylinders is plotted in figure A.1(b) against the one in Tchieu et al. [204]. The final velocity reported in Tchieu et al. [204] for both the cylinders are $\dot{\boldsymbol{x}}_1(\infty) = [0.954 \quad -0.205]^T$ and $\dot{\boldsymbol{x}}_2(\infty) = [0.030 \quad 0.216]^T$ upto three significant digits. With our solver we get $\dot{\boldsymbol{x}}_1(\infty) = [0.954 \quad -0.205]^T$ and $\dot{\boldsymbol{x}}_2(\infty) = [0.029 \quad 0.216]^T$ as the final velocities. Our results are thus in close agreement.

A.2 Two dimensional inviscid flow mediated interactions–Numerics

Using the above algorithm, we seek to replicate the two dimensional neutrally-buoyant master–slave configurations described in the main text in a potential flow context. For such simulations, we use a master cylinder of diameter $D_{\mathrm{m}} = 1\mathrm{m}$ and a slave of diameter $D_{\mathrm{s}} = 0.25\mathrm{m}$. The master is initially kept at $\boldsymbol{q}_{\mathrm{m}} = [0.0 \quad 0.0 \quad 0.0]^T$ and the slave is instantiated at $\boldsymbol{q}_{\mathrm{s}} = [0.0 \quad -0.725 \quad 0.0]^T$. The master is translated in the x direction and oscillated in the y direction. To avoid introducing impulse in the system (and thus eliminating bias) we ramp-up the motion of the master, as given by

$$x_{\mathrm{m}} = U_{\mathrm{l}} \left(t + \frac{1}{r} \ln \left(\frac{1 + e^{r(c-t)}}{1 + e^{rc}} \right) \right) \tag{A.18}$$

$$y_{\mathrm{m}} = \frac{\epsilon \omega D_{\mathrm{m}} \sin(\omega t)}{2\left(1 + e^{r(c-t)}\right)} \tag{A.19}$$

where $r = \frac{28\epsilon\omega}{3\zeta}$ and $c = \frac{15\zeta}{14\omega\epsilon}$ are ramping parameters. We set, for all cases, $\epsilon = 0.05, \omega = 5$ and choose $U_{\mathrm{l}} = \frac{U_{\mathrm{o}}}{2\zeta} = \frac{\epsilon\omega D_{\mathrm{m}}}{4\zeta}$. We then only vary the velocity ratio ζ in our formulation in the simulations shown further below.

Unless stated otherise, we run all simulations with a constant time step $\Delta t = (200\pi)^{-1}T$, where $T = \frac{2\pi}{\omega}$ is the time period of oscillation. We use $v_i = 121$ or $m_i = 60$ fourier modes to capture the master–slave interactions.

A.3 Spline parametrization

We construct the *bean* and *bullet* profile (presented in section 3.2 and section 4.3.4 respectively) of semi-major dimension R by using a spline-based shape parametrization, similar to Rossinelli et al. [227]. The piecewise-cubic spline (figure A.2) is fit in the polar coordinates (with restricted domain on $\theta \in [0, \pi]$), after choosing n control points and specifying their radial k_{i} and angular α_{i} positions. We enforce periodicity and top–bottom symmetry by specifying zero-slope (clamped) boundary conditions for the half-spline and mirroring it about its central axis. Our freedom in the choice of n and consequently the set of $\{k_{\mathrm{i}}, \alpha_{\mathrm{i}}\}$ (with cardinality/degrees of freedom $= 2n$) renders it possible to get desirable shapes with high curvatures.

We tabulate the parameters used for constructing the *bean*, *bullet* and other profiles used in table A.1. We note that across all splines, k_1 and k_n (the scaling lengths of the diametrically opposite points) are

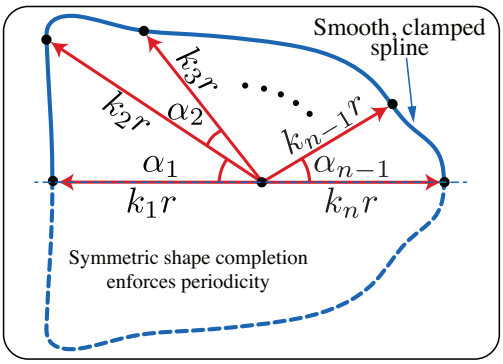

Figure A.2: Construction of the smooth,periodic piece-wise cubic spline with given inputs $\{k_i, \alpha_i\}$

Spline ref.	n	$\{k_i\}$	$\{\alpha_i\}$ (in °)
Bean	4	$\{1.00, 1.50, 1.20, 0.8\}$	$\{45.0, 45.0, 90.0\}$
Bullet	7	$\{1.00, 1.40, 1.42, 1.39, 0.72, 0.95, 1.00\}$	$\{43.0, 1.0, 1.0, 35.0, 90.0, 10.0\}$
figure 4.8(b)	6	$\{1.00, 1.28, 1.31, 1.29, 1.00, 1.00\}$	$\{41.5, 1.75, 1.75, 60.0, 75.0\}$
figure 4.8(c)	6	$\{1.00, 1.40, 1.42, 1.40, 0.99, 1.00\}$	$\{43.0, 1.0, 1.0, 45.0, 90.0\}$

Table A.1: Parameters for the splines used in the thesis

identically set to 1.0 to ensure invariance in the major dimensions of the shape. We then use this invariant dimension to define our *Re* and other quantities derived from it.

References

[1] Colin Gerald Caro, TJ Pedley, and RC Schroter. *The mechanics of the circulation*. Cambridge University Press, 2012 (cit. on pp. 1, 2).

[2] Paul G Falkowski. "The role of phytoplankton photosynthesis in global biogeochemical cycles". In: *Photosynthesis research* 39.3 (1994), pp. 235–258 (cit. on p. 1).

[3] Peter Gravesen, Jens Branebjerg, and O Søndergård Jensen. "Microfluidics-a review". In: *Journal of micromechanics and microengineering* 3.4 (1993), p. 168 (cit. on p. 1).

[4] Howard A Stone, Abraham D Stroock, and Armand Ajdari. "Engineering flows in small devices: microfluidics toward a lab-on-a-chip". In: *Annu. Rev. Fluid Mech.* 36 (2004), pp. 381–411 (cit. on p. 1).

[5] George M Whitesides. "The origins and the future of microfluidics". In: *Nature* 442.7101 (2006), p. 368 (cit. on p. 1).

[6] Eric K Sackmann, Anna L Fulton, and David J Beebe. "The present and future role of microfluidics in biomedical research". In: *Nature* 507.7491 (2014), p. 181 (cit. on p. 1).

[7] Bernhard Sebastian and Petra S Dittrich. "Microfluidics to Mimic Blood Flow in Health and Disease". In: *Annual review of fluid mechanics* 50 (2018), pp. 483–504 (cit. on p. 1).

[8] Maxine A McClain et al. "Microfluidic devices for the high-throughput chemical analysis of cells". In: *Analytical chemistry* 75.21 (2003), pp. 5646–5655 (cit. on p. 1).

[9] Katherine S Elvira, Xavier Casadevall i Solvas, Robert CR Wootton, et al. "The past, present and potential for microfluidic reactor technology in chemical synthesis". In: *Nature chemistry* 5.11 (2013), p. 905 (cit. on p. 1).

[10] Johan Pihl, Jon Sinclair, Mattias Karlsson, and Owe Orwar. "Microfluidics for cell-based assays". In: *Materials today* 8.12 (2005), pp. 46–51 (cit. on p. 1).

[11] Donald L Koch and Ganesh Subramanian. “Collective hydrodynamics of swimming microorganisms: living fluids”. In: *Annual Review of Fluid Mechanics* 43 (2011), pp. 637–659 (cit. on pp. 1, 36).

[12] Jeffrey S Guasto, Roberto Rusconi, and Roman Stocker. “Fluid mechanics of planktonic microorganisms”. In: *Annual Review of Fluid Mechanics* 44 (2012), pp. 373–400 (cit. on p. 1).

[13] Eric Lauga. “Bacterial hydrodynamics”. In: *Annual Review of Fluid Mechanics* 48 (2016), pp. 105–130 (cit. on p. 1).

[14] Henrik Bruus. *Theoretical microfluidics*. Vol. 18. Oxford university press Oxford, 2008 (cit. on p. 1).

[15] Xiujun James Li and Yu Zhou. *Microfluidic devices for biomedical applications*. Elsevier, 2013 (cit. on p. 1).

[16] William H Grover, Alison M Skelley, Chung N Liu, Eric T Lagally, and Richard A Mathies. “Monolithic membrane valves and diaphragm pumps for practical large-scale integration into glass microfluidic devices”. In: *Sensors and Actuators B: Chemical* 89.3 (2003), pp. 315–323 (cit. on p. 1).

[17] Todd M Squires and Martin Z Bazant. *Microfluidic pumps and mixers driven by induced-charge electro-osmosis*. US Patent 7,081,189. July 2006 (cit. on p. 1).

[18] Xiayan Wang, Chang Cheng, Shili Wang, and Shaorong Liu. “Electroosmotic pumps and their applications in microfluidic systems”. In: *Microfluidics and Nanofluidics* 6.2 (2009), pp. 145–162 (cit. on p. 1).

[19] Armando R Tovar, Maulik V Patel, and Abraham P Lee. “Lateral air cavities for microfluidic pumping with the use of acoustic energy”. In: *Microfluidics and Nanofluidics* 10.6 (2011), pp. 1269–1278 (cit. on pp. 1, 5, 13).

[20] Robin H Liu, Jianing Yang, Maciej Z Pindera, Mahesh Athavale, and Piotr Grodzinski. “Bubble-induced acoustic micromixing”. In: *Lab on a Chip* 2.3 (2002), pp. 151–157 (cit. on pp. 1, 2, 6, 13).

[21] Ian Glasgow and Nadine Aubry. “Enhancement of microfluidic mixing using time pulsing”. In: *Lab on a Chip* 3.2 (2003), pp. 114–120 (cit. on p. 1).

[22] Chia-Yen Lee, Chin-Lung Chang, Yao-Nan Wang, and Lung-Ming Fu. “Microfluidic mixing: a review”. In: *International journal of molecular sciences* 12.5 (2011), pp. 3263–3287 (cit. on p. 1).

[23] Philippe Marmottant and Sascha Hilgenfeldt. “Controlled vesicle deformation and lysis by single oscillating bubbles”. In: *Nature* 423.6936 (2003), pp. 153–156 (cit. on pp. 1, 13).

[24] Michael P MacDonald, Gabriel C Spalding, and Kishan Dholakia. “Microfluidic sorting in an optical lattice”. In: *Nature* 426.6965 (2003), p. 421 (cit. on p. 1).

[25] Cheng Wang, Shreyas V Jalikop, and Sascha Hilgenfeldt. "Size-sensitive sorting of microparticles through control of flow geometry". In: *Applied Physics Letters* 99.3 (2011), p. 034101 (cit. on pp. 1, 5, 11, 13, 27).

[26] Julio M Ottino. *The kinematics of mixing: stretching, chaos, and transport*. Vol. 3. Cambridge university press, 1989 (cit. on p. 2).

[27] Abraham D Stroock et al. "Chaotic mixer for microchannels". In: *Science* 295.5555 (2002), pp. 647–651 (cit. on p. 2).

[28] Kashan A Shaikh et al. "A modular microfluidic architecture for integrated biochemical analysis". In: *Proceedings of the National Academy of Sciences* 102.28 (2005), pp. 9745–9750 (cit. on p. 2).

[29] Po Ki Yuen. "SmartBuild–A truly plug-n-play modular microfluidic system". In: *Lab on a Chip* 8.8 (2008), pp. 1374–1378 (cit. on p. 2).

[30] Krisna C Bhargava, Bryant Thompson, and Noah Malmstadt. "Discrete elements for 3D microfluidics". In: *Proceedings of the National Academy of Sciences* 111.42 (2014), pp. 15013–15018 (cit. on p. 2).

[31] George Keith Batchelor. *An introduction to fluid dynamics*. Cambridge university press, 2000 (cit. on pp. 2, 3, 10).

[32] J Holtsmark, I Johnsen, To Sikkeland, and S Skavlem. "Boundary layer flow near a cylindrical obstacle in an oscillating, incompressible fluid". In: *The journal of the acoustical society of America* 26.1 (1954), pp. 26–39 (cit. on pp. 2, 6–8).

[33] WP Raney, JC Corelli, and PJ Westervelt. "Acoustical streaming in the vicinity of a cylinder". In: *The Journal Of The Acoustical Society of America* 26.6 (1954), pp. 1006–1014 (cit. on pp. 2, 6, 7, 21).

[34] S Skavlem and S Tjötta. "Steady rotational flow of an incompressible, viscous fluid enclosed between two coaxial cylinders". In: *The Journal of the Acoustical Society of America* 27.1 (1955), pp. 26–33 (cit. on pp. 2, 6, 7, 21).

[35] N Riley. "Oscillating viscous flows". In: *Mathematika* 12.02 (1965), pp. 161–175 (cit. on pp. 2, 3, 6, 7).

[36] JT Stuart. "Double boundary layers in oscillatory viscous flow". In: *Journal of Fluid Mechanics* 24.04 (1966), pp. 673–687 (cit. on pp. 2, 6, 7, 25).

[37] N Riley. "Oscillatory viscous flows. Review and extension". In: *IMA Journal of Applied Mathematics* 3.4 (1967), pp. 419–434 (cit. on pp. 2, 3, 6–8, 24).

[38] Chang-Yi Wang. "On high-frequency oscillatory viscous flows". In: *Journal of Fluid Mechanics* 32.1 (1968), pp. 55–68 (cit. on pp. 2, 5, 8).

[39] BJ Davidson and N Riley. "Jets induced by oscillatory motion". In: *Journal of Fluid Mechanics* 53.02 (1972), pp. 287–303 (cit. on pp. 2, 3, 6, 8–11, 25).

[40] N Riley. "The steady streaming induced by a vibrating cylinder". In: *Journal of Fluid Mechanics* 68.04 (1975), pp. 801–812 (cit. on pp. 2, 6, 9, 25).

[41] A Bertelsen, Aslak Svardal, and Sigve Tjøtta. "Nonlinear streaming effects associated with oscillating cylinders". In: *Journal of Fluid Mechanics* 59.03 (1973), pp. 493–511 (cit. on pp. 2, 3, 6, 7, 9, 22, 23).

[42] Arnold F Bertelsen. "An experimental investigation of high Reynolds number steady streaming generated by oscillating cylinders". In: *Journal of Fluid Mechanics* 64.03 (1974), pp. 589–598 (cit. on pp. 2, 3, 6, 9, 21, 25).

[43] R Vasantha and N Riley. "On the initiation of jets in oscillatory viscous flows". In: *Proceedings of the Royal Society of London A: Mathematical, Physical and Engineering Sciences*. Vol. 419. 1857. The Royal Society. 1988, pp. 363–378 (cit. on pp. 2, 6, 9).

[44] Michael Longuet-Higgins. "Particle Drift Near an Oscillating Cavity". In: *Sonochemistry and Sonoluminescence*. Ed. by Lawrence A. Crum, Timothy J. Mason, Jacques L. Reisse, and Kenneth S. Suslick. Dordrecht: Springer Netherlands, 1999, pp. 105–116. ISBN: 978-94-015-9215-4. DOI: 10.1007/978-94-015-9215-4_8 (cit. on pp. 2, 11).

[45] N Riley. "Steady streaming". In: *Annual Review of Fluid Mechanics* 33.1 (2001), pp. 43–65 (cit. on pp. 2, 6).

[46] Barry R Lutz, Jian Chen, and Daniel T Schwartz. "Microscopic steady streaming eddies created around short cylinders in a channel: Flow visualization and Stokes layer scaling". In: *Physics of Fluids (1994-present)* 17.2 (2005), p. 023601 (cit. on pp. 2, 3, 5, 6, 13, 23).

[47] Barry R Lutz, Jian Chen, and Daniel T Schwartz. "Hydrodynamic tweezers: 1. Noncontact trapping of single cells using steady streaming microeddies". In: *Analytical chemistry* 78.15 (2006), pp. 5429–5435 (cit. on pp. 2, 3, 5, 6, 13).

[48] Valerie H Lieu, Tyler A House, and Daniel T Schwartz. "Hydrodynamic tweezers: Impact of design geometry on flow and microparticle trapping". In: *Analytical chemistry* 84.4 (2012), pp. 1963–1968 (cit. on pp. 2, 3, 6, 12, 23, 33, 37).

[49] Tyler A House, Valerie H Lieu, and Daniel T Schwartz. "A model for inertial particle trapping locations in hydrodynamic tweezers arrays". In: *Journal of Micromechanics and Microengineering* 24.4 (2014), p. 045019. URL: http://stacks.iop.org/0960-1317/24/i=4/a=045019 (cit. on pp. 2, 3, 6, 12, 23).

[50] Kwitae Chong, Scott D Kelly, Stuart Smith, and Jeff D Eldredge. "Inertial particle trapping in viscous streaming". In: *Physics of Fluids* 25.3 (2013), p. 033602 (cit. on pp. 2, 5, 6, 21, 22, 37).

[51] Kwitae Chong, Scott D Kelly, Stuart T Smith, and Jeff D Eldredge. "Transport of inertial particles by viscous streaming in arrays of oscillating probes". In: *Physical Review E* 93.1 (2016), p. 013109 (cit. on pp. 2, 6, 12).

[52] Sadatoshi Taneda. "Visualization of steady flows induced by a circular cylinder performing a rotatory oscillation about an eccentric axis". In: *Journal of the Physical Society of Japan* 49.5 (1980), pp. 2038–2041 (cit. on pp. 2, 10).

[53] Masakazu Tatsuno. "Circulatory streaming around an oscillating circular cylinder at low Reynolds numbers". In: *Journal of the Physical Society of Japan* 35.3 (1973), pp. 915–920 (cit. on pp. 2, 3, 12).

[54] Masakazu Tatsuno. "Circulatory streaming in the vicinity of an oscillating square cylinder". In: *Journal of the Physical Society of Japan* 36.4 (1974), pp. 1185–1191 (cit. on pp. 2, 3, 11, 12, 31).

[55] Masakazu Tatsuno. "Circulatory streaming in the vicinity of an oscillating triangular cylinder". In: *Journal of the Physical Society of Japan* 38.1 (1975), pp. 257–264 (cit. on pp. 2, 3, 11, 31, 45).

[56] Tamsin A Spelman and Eric Lauga. "Arbitrary axisymmetric steady streaming: Flow, force and propulsion". In: *Journal of Engineering Mathematics* (2015), pp. 1–35 (cit. on pp. 2, 6, 11, 13).

[57] Greg A Voth et al. "Ordered clusters and dynamical states of particles in a vibrated fluid". In: *Physical review letters* 88.23 (2002), p. 234301 (cit. on pp. 2, 5, 13, 36).

[58] Daniel Ahmed, Xiaole Mao, Bala Krishna Juluri, and Tony Jun Huang. "A fast microfluidic mixer based on acoustically driven sidewall-trapped microbubbles". In: *Microfluidics and nanofluidics* 7.5 (2009), p. 727 (cit. on pp. 2, 6, 13).

[59] Sang Kug Chung and Sung Kwon Cho. "On-chip manipulation of objects using mobile oscillating bubbles". In: *Journal of Micromechanics and Microengineering* 18.12 (2008), p. 125024 (cit. on pp. 2, 5, 13).

[60] Jonathan Kao, Xiaolin Wang, John Warren, Jie Xu, and Daniel Attinger. "A bubble-powered micro-rotor: conception, manufacturing, assembly and characterization". In: *Journal of Micromechanics and Microengineering* 17.12 (2007), p. 2454 (cit. on pp. 2, 13).

[61] Raqeeb Thameem, Bhargav Rallabandi, and Sascha Hilgenfeldt. “Particle migration and sorting in microbubble streaming flows”. In: *Biomicrofluidics* 10.1 (2016), p. 014124 (cit. on pp. 2, 5, 11, 13, 27).

[62] Raqeeb Thameem, Bhargav Rallabandi, and Sascha Hilgenfeldt. “Fast inertial particle manipulation in oscillating flows”. In: *Physical Review Fluids* 2.5 (2017), p. 052001 (cit. on pp. 2, 6, 11, 27).

[63] Milton Van Dyke and Milton Van Dyke. “An album of fluid motion”. In: (1982) (cit. on pp. 3, 23, 33).

[64] Li Jeany Zhang and Jeff D Eldredge. “A viscous vortex particle method for deforming bodies with application to biolocomotion”. In: *International journal for numerical methods in fluids* 59.12 (2009), pp. 1299–1320 (cit. on pp. 3, 29).

[65] M Tatsuno and PW Bearman. “A visual study of the flow around an oscillating circular cylinder at low Keulegan–Carpenter numbers and low Stokes numbers”. In: *Journal of Fluid Mechanics* 211 (1990), pp. 157–182 (cit. on pp. 3, 15, 32, 33).

[66] Philip Hall. “On the stability of the unsteady boundary layer on a cylinder oscillating transversely in a viscous fluid”. In: *Journal of Fluid Mechanics* 146 (1984), pp. 347–367 (cit. on pp. 3, 15).

[67] CHK Williamson. “Sinusoidal flow relative to circular cylinders”. In: *Journal of Fluid Mechanics* 155 (1985), pp. 141–174 (cit. on pp. 3, 15).

[68] Peter Justesen. “A numerical study of oscillating flow around a circular cylinder”. In: *Journal of Fluid Mechanics* 222 (1991), pp. 157–196 (cit. on pp. 3, 15).

[69] XW Lin, PW Bearman, and JMR Graham. “A numerical study of oscillatory flow about a circular cylinder for low values of beta parameter”. In: *Journal of Fluids and Structures* 10.5 (1996), pp. 501–526 (cit. on pp. 3, 15).

[70] John R Elston, John Sheridan, and Hugh M Blackburn. “Two-dimensional Floquet stability analysis of the flow produced by an oscillating circular cylinder in quiescent fluid”. In: *European Journal of Mechanics-B/Fluids* 23.1 (2004), pp. 99–106 (cit. on pp. 3, 15).

[71] John R Elston, Hugh M Blackburn, and John Sheridan. “The primary and secondary instabilities of flow generated by an oscillating circular cylinder”. In: *Journal of Fluid Mechanics* 550 (2006), pp. 359–389 (cit. on pp. 3, 15).

[72] Turgut Sarpkaya. “Force on a circular cylinder in viscous oscillatory flow at low Keulegan—Carpenter numbers”. In: *Journal of Fluid Mechanics* 165 (1986), pp. 61–71 (cit. on pp. 5, 15).

[73] Guo Zhan Lum et al. “Shape-programmable magnetic soft matter”. In: *Proceedings of the National Academy of Sciences* 113.41 (2016), E6007–E6015 (cit. on p. 5).

[74] Li Zhang et al. “Characterizing the swimming properties of artificial bacterial flagella”. In: *Nano letters* 9.10 (2009), pp. 3663–3667 (cit. on p. 5).

[75] RJ Dijkink, JP Van Der Dennen, CD Ohl, and A Prosperetti. “The ‘acoustic scallop’: a bubble-powered actuator”. In: *Journal of Micromechanics and Microengineering* 16.8 (2006), p. 1653 (cit. on pp. 5, 13).

[76] Murat Kaynak et al. “Acoustic actuation of bioinspired microswimmers”. In: *Lab on a Chip* 17.3 (2017), pp. 395–400 (cit. on p. 5).

[77] Brian J Williams, Sandeep V Anand, Jagannathan Rajagopalan, and M Taher A Saif. “A self-propelled biohybrid swimmer at low Reynolds number”. In: *Nature communications* 5 (2014), p. 3081 (cit. on pp. 5, 6, 36).

[78] Sung-Jin Park et al. “Phototactic guidance of a tissue-engineered soft-robotic ray”. In: *Science* 353.6295 (2016), pp. 158–162 (cit. on pp. 5, 6, 36).

[79] Janna C Nawroth et al. “A tissue-engineered jellyfish with biomimetic propulsion”. In: *Nature biotechnology* 30.8 (2012), p. 792 (cit. on pp. 5, 6).

[80] William Gilpin, Vivek N Prakash, and Manu Prakash. “Vortex arrays and ciliary tangles underlie the feeding-swimming trade-off in starfish larvae”. In: *Nature Physics* (2016) (cit. on pp. 5, 6, 29).

[81] Kenta Ishimoto. “A spherical squirming swimmer in unsteady Stokes flow”. In: *Journal of Fluid Mechanics* 723 (2013), pp. 163–189 (cit. on p. 5).

[82] Kyungjoo Ryu, Sang Kug Chung, and Sung Kwon Cho. “Micropumping by an acoustically excited oscillating bubble for automated implantable microfluidic devices”. In: *JALA: Journal of the Association for Laboratory Automation* 15.3 (2010), pp. 163–171 (cit. on pp. 5, 13).

[83] Barry R Lutz, Jian Chen, and Daniel T Schwartz. “Characterizing homogeneous chemistry using well-mixed microeddies”. In: *Analytical chemistry* 78.5 (2006), pp. 1606–1612 (cit. on pp. 5, 13).

[84] Robin Hui Liu, Ralf Lenigk, Roberta L Druyor-Sanchez, Jianing Yang, and Piotr Grodzinski. “Hybridization enhancement using cavitation microstreaming”. In: *Analytical Chemistry* 75.8 (2003), pp. 1911–1917 (cit. on pp. 5, 6, 13).

[85] Philippe Marmottant and Sascha Hilgenfeldt. “A bubble-driven microfluidic transport element for bioengineering”. In: *Proceedings of the National Academy of Sciences of the United States of America* 101.26 (2004), pp. 9523–9527 (cit. on pp. 5, 13).

[86] Philppe Marmottant, JP Raven, HJGE Gardeniers, JG Bomer, and Sascha Hilgenfeldt. “Microfluidics with ultrasound-driven bubbles”. In: *Journal of Fluid Mechanics* 568 (2006), pp. 109–118 (cit. on pp. 5, 13).

[87] Sang Kug Chung and Sung Kwon Cho. “3-D manipulation of millimeter-and micro-sized objects using an acoustically excited oscillating bubble”. In: *Microfluidics and nanofluidics* 6.2 (2009), pp. 261–265 (cit. on pp. 5, 13).

[88] Barry R Lutz, Jian Chen, and Daniel T Schwartz. “Microfluidics without microfabrication”. In: *Proceedings of the National Academy of Sciences* 100.8 (2003), pp. 4395–4398 (cit. on pp. 5, 13).

[89] PW Duck and FT Smith. “Steady streaming induced between oscillating cylinders”. In: *Journal of Fluid Mechanics* 91.01 (1979), pp. 93–110 (cit. on p. 6).

[90] N Riley. “Oscillating viscous flows: II Superposed oscillations”. In: *Mathematika* 38.02 (1991), pp. 203–216 (cit. on pp. 6, 11, 26).

[91] N Riley and EJ Watson. “Eccentric oscillations of a circular cylinder in a viscous fluid”. In: *Mathematika* 40.02 (1993), pp. 187–202 (cit. on pp. 6, 10).

[92] Hugh M Blackburn, JR Elston, and J Sheridan. “Bluff-body propulsion produced by combined rotary and translational oscillation”. In: *Physics of Fluids* 11.1 (1999), pp. 4–6 (cit. on pp. 6, 11, 26).

[93] MF Wybrow, B Yan, and N Riley. “Oscillatory flow over a circular cylinder close to a plane boundary”. In: *Fluid dynamics research* 18.5 (1996), pp. 269–288 (cit. on pp. 6, 12, 13).

[94] W Coenen and N Riley. “Oscillatory flow about a cylinder pair”. In: *Quarterly journal of mechanics and applied mathematics* 62.1 (2008), pp. 53–66 (cit. on pp. 6, 12).

[95] W Coenen. “Oscillatory flow about a cylinder pair with unequal radii”. In: *Fluid Dynamics Research* 45.5 (2013), p. 055511 (cit. on pp. 6, 12).

[96] W Coenen. “Steady streaming around a cylinder pair”. In: *Proc. R. Soc. A*. Vol. 472. 2195. The Royal Society. 2016, p. 20160522 (cit. on pp. 6, 12).

[97] Sung Kyun Kim and Armin W Troesch. “Streaming flows generated by high-frequency small-amplitude oscillations of arbitrarily shaped cylinders”. In: *Physics of Fluids A: Fluid Dynamics* 1.6 (1989), pp. 975–985 (cit. on p. 6).

[98] B Yan, DB Ingham, and BR Morton. "The streaming flow initiated by oscillating cascades of cylinders and their stability". In: *Physics of Fluids* 6.4 (1994), pp. 1472–1481 (cit. on pp. 6, 12).

[99] Mikhail Ovchinnikov, Jianbo Zhou, and Satish Yalamanchili. "Acoustic streaming of a sharp edge". In: *The Journal of the Acoustical Society of America* 136.1 (2014), pp. 22–29 (cit. on pp. 6, 12).

[100] Gelson J Pagan-Diaz et al. "Simulation and Fabrication of Stronger, Larger, and Faster Walking Biohybrid Machines". In: *Advanced Functional Materials* 28.23 (2018), p. 1801145 (cit. on pp. 6, 36).

[101] Michael Faraday. "XVII. On a peculiar class of acoustical figures; and on certain forms assumed by groups of particles upon vibrating elastic surfaces". In: *Philosophical transactions of the Royal Society of London* 121 (1831), pp. 299–340 (cit. on p. 7).

[102] Lord Rayleigh. "On the Circulation of Air Observed in Kundt's Tubes, and on Some Allied Acoustical Problems". In: *Philosophical Transactions of the Royal Society* 175 (1883), pp. 1–21 (cit. on p. 7).

[103] Hermann Schlichting. "Berechnung ebener periodischer Grenzschichtstromungen". In: *Phys. z.* 33 (1932), pp. 327–335 (cit. on p. 7).

[104] Edward Neville Da Costa Andrade. "On the circulations caused by the vibration of air in a tube". In: *Proc. R. Soc. Lond. A* 134.824 (1931), pp. 445–470 (cit. on pp. 7, 13).

[105] SS Sadhal. "Acoustofluidics 13: Analysis of acoustic streaming by perturbation methods". In: *Lab on a Chip* 12.13 (2012), pp. 2292–2300 (cit. on p. 8).

[106] WG Bickley. "LXXIII. The plane jet". In: *The London, Edinburgh, and Dublin Philosophical Magazine and Journal of Science* 23.156 (1937), pp. 727–731 (cit. on pp. 9, 25).

[107] EW Haddon and N Riley. "The steady streaming induced between oscillating circular cylinders". In: *The Quarterly Journal of Mechanics and Applied Mathematics* 32.3 (1979), pp. 265–282 (cit. on p. 9).

[108] N Riley. "Streaming from a cylinder due to an acoustic source". In: *Journal of Fluid Mechanics* 180 (1987), pp. 319–326 (cit. on p. 9).

[109] Tosio Miyagi and Kazuhiro Nakahasi. "Secondary flow induced by an unharmonically oscillating circular cylinder". In: *Journal of the Physical Society of Japan* 39.2 (1975), pp. 519–526 (cit. on p. 10).

[110] Masakazu Tatsuno. "Secondary flow induced by a circular cylinder performing unharmonic oscillations". In: *Journal of the Physical Society of Japan* 50.1 (1981), pp. 330–337 (cit. on p. 10).

[111] Syozo Kubo and Yukio Kitano. “Secondary flow induced by a circular cylinder oscillating in two directions”. In: *Journal of the Physical Society of Japan* 49.5 (1980), pp. 2026–2037 (cit. on pp. 10, 38).

[112] Ken-ichi Kusukawa, Yô Shimizu, and Akira Shinoda. “The secondary flow about a circular cylinder oscillating rotationally around an eccentric axis”. In: *Journal of the Physical Society of Japan* 49.6 (1980), pp. 2400–2406 (cit. on p. 10).

[113] M Nazarinia, D Lo Jacono, MC Thompson, and J Sheridan. “Flow behind a cylinder forced by a combination of oscillatory translational and rotational motions”. In: *Physics of Fluids* 21.5 (2009), p. 051701 (cit. on pp. 11, 26).

[114] M Nazarinia, D Lo Jacono, MC Thompson, and J Sheridan. “The three-dimensional wake of a cylinder undergoing a combination of translational and rotational oscillation in a quiescent fluid”. In: *Physics of Fluids* 21.6 (2009), p. 064101 (cit. on pp. 11, 26).

[115] Mehdi Nazarinia, David Lo Jacono, Mark C Thompson, and John Sheridan. “Flow over a cylinder subjected to combined translational and rotational oscillations”. In: *Journal of Fluids and Structures* 32 (2012), pp. 135–145 (cit. on pp. 11, 26).

[116] Christopher Koehler, Philip Beran, Marcos Vanella, and Elias Balaras. “Flows produced by the combined oscillatory rotation and translation of a circular cylinder in a quiescent fluid”. In: *Journal of Fluid Mechanics* 764 (2015), pp. 148–170 (cit. on pp. 11, 26).

[117] Muhammad A. Sadiq and Hina Khan. “Steady streaming due to transverse vibration and torsional oscillation of a cylinder”. In: *Journal of the Physical Society of Japan* 81.4 (2012), p. 044402 (cit. on p. 11).

[118] Michael S. Longuet-Higgins. “Viscous streaming from an oscillating spherical bubble”. In: *Proceedings of the Royal Society of London A: Mathematical, Physical and Engineering Sciences* 454.1970 (1998), pp. 725–742. ISSN: 1364-5021. eprint: http://rspa.royalsocietypublishing.org/content/454/1970/725.full.pdf (cit. on pp. 11, 21, 22).

[119] Michael Longuet-Higgins. “Viscous Streaming Near an Oscillating and Pulsating Spherical Cavity”. In: *Sonochemistry and Sonoluminescence*. Springer, 1999, pp. 117–126 (cit. on p. 11).

[120] Siddhansh Agarwal, Bhargav Rallabandi, and Sascha Hilgenfeldt. “Inertial forces for particle manipulation near oscillating interfaces”. In: *Physical Review Fluids* 3.10 (2018), p. 104201 (cit. on pp. 11, 27).

[121] JR Blake. “Self propulsion due to oscillations on the surface of a cylinder at low Reynolds number”. In: *Bulletin of the Australian Mathematical Society* 5.2 (1971), pp. 255–264 (cit. on pp. 11, 28).

[122] JR Blake. “A spherical envelope approach to ciliary propulsion”. In: *Journal of Fluid Mechanics* 46.1 (1971), pp. 199–208 (cit. on p. 11).

[123] François Nadal and Eric Lauga. “Asymmetric steady streaming as a mechanism for acoustic propulsion of rigid bodies”. In: *Physics of Fluids* 26.8 (2014), p. 082001 (cit. on p. 11).

[124] Akira Yoshizawa. “Steady Streaming Induced by an Oscillating Flat Plate in a Viscous Fluid”. In: *Journal of the Physical Society of Japan* 37.2 (1974), pp. 524–528 (cit. on p. 11).

[125] Ko Tamada and Tosio Miyagi. “Secondary flow around an oscillating cylinder”. In: *Journal of the Physical Society of Japan* 37.1 (1974), pp. 249–253 (cit. on p. 11).

[126] Norman Riley. “Circular oscillations of a cylinder in a viscous fluid”. In: *Zeitschrift für Angewandte Mathematik und Physik (ZAMP)* 29.3 (1978), pp. 439–449 (cit. on p. 12).

[127] PW Duck. “Oscillatory flow inside a square cavity”. In: *Journal of Fluid Mechanics* 122 (1982), pp. 215–234 (cit. on p. 12).

[128] PG Pattani and MD Olson. “Periodic solutions of rigid body–viscous flow interaction”. In: *International journal for numerical methods in fluids* 7.7 (1987), pp. 653–695 (cit. on p. 12).

[129] PW Duck and RJ Bodonyi. “Oscillatory flow over a semi-infinite flat plate at low Reynolds numbers”. In: *Computers & fluids* 16.3 (1988), pp. 311–326 (cit. on p. 12).

[130] Muhammad A. Sadiq. “Steady streaming due to the vibrating wall in an infinite viscous incompressible fluid”. In: *Journal of the Physical Society of Japan* 80.3 (2011), p. 034404 (cit. on p. 12).

[131] Nitesh Nama, Po-Hsun Huang, Tony Jun Huang, and Francesco Costanzo. “Investigation of acoustic streaming patterns around oscillating sharp edges”. In: *Lab on a Chip* 14.15 (2014), pp. 2824–2836 (cit. on p. 12).

[132] N Riley and MF Wybrow. “The flow induced by the torsional oscillations of an elliptic cylinder”. In: *Journal of Fluid Mechanics* 290 (1995), pp. 279–298 (cit. on p. 12).

[133] B Yan, DB Ingham, and BR Morton. “Streaming flow induced by an oscillating cascade of circular cylinders”. In: *Journal of Fluid Mechanics* 252 (1993), pp. 147–171 (cit. on p. 12).

[134] C.Y. Wang. “The flow field induced by an oscillating sphere”. In: *Journal of Sound and Vibration* 2.3 (1965), pp. 257–269 (cit. on p. 13).

[135] N. Riley. “On a sphere oscillating in a viscous fluid”. In: *The Quarterly Journal of Mechanics and Applied Mathematics* 19.4 (1966), pp. 461–472 (cit. on p. 13).

[136] N. Dohara. “The unsteady flow around an oscillating sphere in a viscous fluid”. In: *Journal of the Physical Society of Japan* 51.12 (1982), pp. 4095–4103 (cit. on p. 13).

[137] C.Y. Wang. “Acoustic streaming of a sphere near an unsteady source”. In: *The Journal of the Acoustical Society of America* 71.3 (1982), pp. 580–584 (cit. on p. 13).

[138] N. Amin and N. Riley. “Streaming from a sphere due to a pulsating source”. In: *Journal of Fluid Mechanics* 210 (1990), pp. 459–473 (cit. on p. 13).

[139] R. Mei. “Flow due to an oscillating sphere and an expression for unsteady drag on the sphere at finite Reynolds number”. In: *Journal of Fluid Mechanics* 270 (1994), pp. 133–174 (cit. on p. 13).

[140] AY Rednikov and Satwindar S Sadhal. “Steady streaming from an oblate spheroid due to vibrations along its axis”. In: *Journal of fluid mechanics* 499 (2004), pp. 345–380 (cit. on p. 13).

[141] J Milton Andres and Uno Ingard. “Acoustic streaming at low Reynolds numbers”. In: *The Journal of the Acoustical Society of America* 25.5 (1953), pp. 932–938 (cit. on p. 13).

[142] C.A. Lane. “Acoustical streaming in the vicinity of a sphere”. In: *The Journal of the Acoustical Society of America* 27.6 (1955), pp. 1082–1086 (cit. on p. 13).

[143] S. Hassan, T.P. Lyubimova, D.V. Lyubimov, and M. Kawaji. “Effects of vibrations on particle motion near a wall: Existence of attraction force”. In: *International journal of multiphase flow* 32.9 (2006), pp. 1037–1054 (cit. on p. 13).

[144] F. Otto, E.K. Riegler, and G.A. Voth. “Measurements of the steady streaming flow around oscillating spheres using three dimensional particle tracking velocimetry”. In: *Physics of fluids* 20.9 (2008), p. 093304 (cit. on p. 13).

[145] D. Klotsa, M.R. Swift, R.M. Bowley, and P.J. King. “Interaction of spheres in oscillatory fluid flows”. In: *Physical Review E* 76.5 (2007), p. 056314 (cit. on p. 13).

[146] Charlotte W Kotas, Minami Yoda, and Peter H Rogers. “Visualization of steady streaming near oscillating spheroids”. In: *Experiments in fluids* 42.1 (2007), pp. 111–121 (cit. on p. 13).

[147] Charlotte W Kotas, Minami Yoda, and Peter H Rogers. “Steady streaming flows near spheroids oscillated at multiple frequencies”. In: *Experiments in Fluids* 45.2 (2008), pp. 295–307 (cit. on p. 13).

[148] C.K. Drummond and F.A. Lyman. “Mass transfer from a sphere in an oscillating flow with zero mean velocity”. In: *Computational Mechanics* 6.4 (1990), pp. 315–326 (cit. on p. 13).

[149] E.J. Chang and M.R. Maxey. “Unsteady flow about a sphere at low to moderate Reynolds number. Part 1. Oscillatory motion”. In: *Journal of Fluid Mechanics* 277 (1994), pp. 347–379 (cit. on p. 13).

[150] R.S. Alassar and H.M. Badr. “Oscillating viscous flow over a sphere”. In: *Computers and fluids* 26.7 (1997), pp. 661–682 (cit. on p. 13).

[151] RS Alassar and HM Badr. “Oscillating Flow over oblate spheroids”. In: *Acta mechanica* 137.3 (1999), pp. 237–254 (cit. on p. 13).

[152] H.M. Blackburn. “Mass and momentum transport from a sphere in steady and oscillatory flows”. In: *Physics of fluids* 14.11 (2002), pp. 3997–4011 (cit. on p. 13).

[153] Yun He et al. “Ultrasound microbubble-mediated delivery of the siRNAs targeting MDR1 reduces drug resistance of yolk sac carcinoma L2 cells”. In: *Journal of Experimental & Clinical Cancer Research* 30.1 (2011), p. 104 (cit. on p. 13).

[154] Yuhao Xu et al. “Microbubble array for on-chip worm processing”. In: *Applied Physics Letters* 102.2 (2013), p. 023702 (cit. on p. 13).

[155] Paul JA Kenis, Rustem F Ismagilov, and George M Whitesides. “Microfabrication inside capillaries using multiphase laminar flow patterning”. In: *Science* 285.5424 (1999), pp. 83–85 (cit. on p. 13).

[156] Shuichi Takayama et al. “Patterning cells and their environments using multiple laminar fluid flows in capillary networks”. In: *Proceedings of the National Academy of Sciences* 96.10 (1999), pp. 5545–5548 (cit. on p. 13).

[157] Alexandros P Papavasiliou, Dorian Liepmann, and Albert P Pisano. “Fabrication of a free floating silicon gate valve”. In: *Proceedings of the ASME MEMS Division*. 1999, pp. 435–440 (cit. on p. 13).

[158] Jung Min Won, Jeong Hyun Lee, Kyong Ho Lee, Kyehan Rhee, and Sang Kug Chung. “Propulsion of water-floating objects by acoustically oscillating microbubbles”. In: *International Journal of Precision Engineering and Manufacturing* 12.3 (2011), pp. 577–580 (cit. on p. 13).

[159] Jian Feng, Junqi Yuan, and Sung Kwon Cho. “2-D steering and propelling of acoustic bubble-powered microswimmers”. In: *Lab on a Chip* 16.12 (2016), pp. 2317–2325 (cit. on p. 13).

[160] Lloyd H Carpenter. *Forces on cylinders and plates in an oscillating fluid*. Vol. 4821. US Department of Commerce, National Bureau of Standards, 1956 (cit. on p. 15).

[161] ED Obasaju, PW Bearman, and JMR Graham. “A study of forces, circulation and vortex patterns around a circular cylinder in oscillating flow”. In: *Journal of Fluid Mechanics* 196 (1988), pp. 467–494 (cit. on p. 15).

[162] Hui-Liu Zhang and Xin Zhang. “Flow structure analysis around an oscillating circular cylinder at low KC number: a numerical study”. In: *Computers & fluids* 26.1 (1997), pp. 83–106 (cit. on p. 15).

[163] D Nehari, V Armenio, and F Ballio. “Three-dimensional analysis of the unidirectional oscillatory flow around a circular cylinder at low Keulegan–Carpenter and beta numbers”. In: *Journal of Fluid Mechanics* 520 (2004), pp. 157–186 (cit. on p. 15).

[164] PW Bearman, MJ Downie, JMR Graham, and ED Obasaju. “Forces on cylinders in viscous oscillatory flow at low Keulegan-Carpenter numbers”. In: *Journal of Fluid Mechanics* 154 (1985), pp. 337–356 (cit. on p. 15).

[165] HM Badr, SCR Dennis, S Kocabiyik, and P Nguyen. “Viscous oscillatory flow about a circular cylinder at small to moderate Strouhal number”. In: *Journal of Fluid Mechanics* 303 (1995), pp. 215–232 (cit. on p. 15).

[166] H Dütsch, F Durst, S Becker, and H Lienhart. “Low-Reynolds-number flow around an oscillating circular cylinder at low Keulegan–Carpenter numbers”. In: *Journal of Fluid Mechanics* 360 (1998), pp. 249–271 (cit. on pp. 15, 32).

[167] G Iliadis and P Anagnostopoulos. “Numerical visualization of oscillatory flow around a circular cylinder at Re= 200 and KC= 20—an aperiodic flow case”. In: *International Journal for Numerical Methods in Biomedical Engineering* 14.3 (1998), pp. 181–194 (cit. on p. 15).

[168] KM Lam and GQ Dai. “Formation of vortex street and vortex pair from a circular cylinder oscillating in water”. In: *Experimental Thermal and Fluid Science* 26.8 (2002), pp. 901–915 (cit. on p. 15).

[169] JR Elston, J Sheridan, and Hugh M Blackburn. “The transition to three-dimensionality in the flow produced by an oscillating circular cylinder”. In: *Transition* 10 (2001), p. 14 (cit. on p. 15).

[170] H Honji. “Streaked flow around an oscillating circular cylinder”. In: *Journal of Fluid Mechanics* 107 (1981), pp. 509–520 (cit. on p. 15).

[171] B Uzunoğlu, M Tan, and WG Price. “Low-Reynolds-number flow around an oscillating circular cylinder using a cell viscousboundary element method”. In: *International Journal for Numerical Methods in Engineering* 50.10 (2001), pp. 2317–2338 (cit. on p. 15).

[172] Lu Xi-yun and Ling Guo-can. “Three-dimensional instability of an oscillating viscous flow past a circular cylinder”. In: *Applied Mathematics and Mechanics* 24.7 (2003), pp. 791–800 (cit. on p. 15).

[173] Turgut Sarpkaya. “Experiments on the stability of sinusoidal flow over a circular cylinder”. In: *Journal of Fluid Mechanics* 457 (2002), pp. 157–180 (cit. on p. 15).

[174] T Sarpkaya and W Butterworth. "Separation points on a cylinder in oscillating flow". In: *ASME JOURNAL OF OFFSHORE MECHANICS AND ARCTIC ENGINEERING* 114 (1992), pp. 28–36 (cit. on p. 15).

[175] J-C Lin and D Rockwell. "Quantitative interpretation of vortices from a cylinder oscillating in quiescent fluid". In: *Experiments in Fluids* 23.2 (1997), pp. 99–104 (cit. on p. 15).

[176] Turgut Sarpkaya. "Structures of separation on a circular cylinder in periodic flow". In: *Journal of Fluid Mechanics* 567 (2006), pp. 281–297 (cit. on p. 15).

[177] Farah Rashid, Magnus Vartdal, and John Grue. "Oscillating cylinder in viscous fluid: calculation of flow patterns and forces". In: *Journal of Engineering Mathematics* 70.1-3 (2011), pp. 281–295 (cit. on p. 15).

[178] José P Gallardo, Helge I Andersson, and Bjørnar Pettersen. "Three-dimensional instabilities in oscillatory flow past elliptic cylinders". In: *Journal of Fluid Mechanics* 798 (2016), pp. 371–397 (cit. on p. 15).

[179] P Anagnostopoulos and Ch Dikarou. "Numerical simulation of viscous oscillatory flow past four cylinders in square arrangement". In: *Journal of Fluids and Structures* 27.2 (2011), pp. 212–232 (cit. on p. 15).

[180] Ming-Jyh Chern, Wei-Cheng Shiu, and Tzyy-Leng Horng. "Immersed boundary modeling for interaction of oscillatory flow with cylinder array under effects of flow direction and cylinder arrangement". In: *Journal of Fluids and Structures* 43 (2013), pp. 325–346 (cit. on p. 15).

[181] Ming Zhao and Liang Cheng. "Two-dimensional numerical study of vortex shedding regimes of oscillatory flow past two circular cylinders in side-by-side and tandem arrangements at low Reynolds numbers". In: *Journal of fluid mechanics* 751 (2014), pp. 1–37 (cit. on p. 15).

[182] Feifei Tong, Liang Cheng, Ming Zhao, and Hongwei An. "Oscillatory flow regimes around four cylinders in a square arrangement under small KCand Re conditions". In: *Journal of Fluid Mechanics* 769 (2015), pp. 298–336 (cit. on p. 15).

[183] Sid'Ahmed Daoud, Driss Nehari, Mohamed Aichouni, and Taieb Nehari. "Numerical Simulations of an Oscillating Flow Past an Elliptic Cylinder". In: *Journal of Offshore Mechanics and Arctic Engineering* 138.1 (2016), p. 011802 (cit. on p. 15).

[184] Feifei Tong et al. "Flow regimes for a square cross-section cylinder in oscillatory flow". In: *Journal of Fluid Mechanics* 813 (2017), pp. 85–109 (cit. on p. 15).

[185] Mattia Gazzola, Philippe Chatelain, Wim M Van Rees, and Petros Koumoutsakos. "Simulations of single and multiple swimmers with non-divergence free deforming geometries". In: *Journal of Computational Physics* 230.19 (2011), pp. 7093–7114 (cit. on pp. 16, 18, 19, 22, 39).

[186] Mattia Gazzola. "Simulation, optimization and learning of artificial swimmers". PhD thesis. ETH Zurich, 2013 (cit. on pp. 17–19, 22).

[187] Philippe Angot, Charles-Henri Bruneau, and Pierre Fabrie. "A penalization method to take into account obstacles in incompressible viscous flows". In: *Numerische Mathematik* 81.4 (1999), pp. 497–520 (cit. on p. 18).

[188] Willem M van Rees. "3D simulations of vortex dynamics and biolocomotion". PhD thesis. ETH Zurich, 2014 (cit. on p. 19).

[189] N.A. Patankar and N. Sharma. "A fast projection scheme for the direct numerical simulation of rigid particulate flows". In: *Communications in Numerical Methods in Engineering* 21.8 (2005), pp. 419–432 (cit. on p. 19).

[190] M. Gazzola, O.V. Vasilyev, and P. Koumoutsakos. "Shape optimization for drag reduction in linked bodies using evolution strategies". In: *Computers and Structures* 89.11-12 (2011), pp. 1224–1231 (cit. on pp. 22, 39, 49).

[191] M. Gazzola, W.M. van Rees, and P. Koumoutsakos. "C-start: optimal start of larval fish". In: *Journal of Fluid Mechanics* 698 (2012), pp. 5–18. DOI: 10.1017/jfm.2011.558 (cit. on pp. 22, 39, 49).

[192] Martin R Maxey and James J Riley. "Equation of motion for a small rigid sphere in a nonuniform flow". In: *The Physics of Fluids* 26.4 (1983), pp. 883–889 (cit. on p. 27).

[193] Tejaswin Parthasarathy, Fan Kiat Chan, and Mattia Gazzola. "Streaming enhanced flow-mediated transport". In: *arXiv preprint arXiv:1809.04566* (2018) (cit. on p. 36).

[194] Hakan Ceylan, Joshua Giltinan, Kristen Kozielski, and Metin Sitti. "Mobile microrobots for bioengineering applications". In: *Lab on a Chip* 17.10 (2017), pp. 1705–1724 (cit. on pp. 36, 37).

[195] M Gazzola, LH Dudte, AG McCormick, and L Mahadevan. "Forward and inverse problems in the mechanics of soft filaments". In: *Royal Society Open Science* 5.6 (2018), p. 171628 (cit. on p. 36).

[196] D. Weihs. "Hydromechanics of fish schooling". In: *Nature* 241.5387 (1973), pp. 290–291 (cit. on p. 36).

[197] Takuji Ishikawa, MP Simmonds, and TJ Pedley. "Hydrodynamic interaction of two swimming model micro-organisms". In: *Journal of Fluid Mechanics* 568 (2006), pp. 119–160 (cit. on p. 36).

[198] B. Metzger, M. Nicolas, and E. Guazzelli. “Falling clouds of particles in viscous fluids”. In: *Journal of Fluid Mechanics* 580 (2007), pp. 283–301 (cit. on p. 36).

[199] J.F. Brady and G. Bossis. “Stokesian dynamics”. In: *Annual Review of Fluid Mechanics* 20 (1988), pp. 111–157 (cit. on p. 37).

[200] E. Lauga and T.R. Powers. “The hydrodynamics of swimming microorganisms”. In: *Reports on Progress in Physics* 72.9 (2009), p. 096601 (cit. on p. 37).

[201] G Subramanian and Donald L Koch. “Evolution of clusters of sedimenting low-Reynolds-number particles with Oseen interactions”. In: *Journal of Fluid Mechanics* 603 (2008), pp. 63–100 (cit. on p. 37).

[202] Sujit Nair and Eva Kanso. “Hydrodynamically coupled rigid bodies”. In: *Journal of Fluid Mechanics* 592 (2007), pp. 393–411 (cit. on pp. 37, 54, 55).

[203] Silas Alben. “Wake-mediated synchronization and drafting in coupled flags”. In: *Journal of Fluid Mechanics* 641 (2009), pp. 489–496 (cit. on p. 37).

[204] AA Tchieu, D Crowdy, and A Leonard. “Fluid-structure interaction of two bodies in an inviscid fluid”. In: *Physics of Fluids* 22.10 (2010), p. 107101 (cit. on pp. 37, 56).

[205] J.C. Liao, D.N. Beal, G.V. Lauder, and M.S. Triantafyllou. “Fish exploiting vortices decrease muscle activity”. In: *Science* 302.5650 (2003), pp. 1566–1569 (cit. on p. 37).

[206] J.C. Liao. “A review of fish swimming mechanics and behaviour in altered flows”. In: *Philosophical Transactions of the Royal Society B-Biological Sciences* 362.1487 (2007), pp. 1973–1993 (cit. on p. 37).

[207] L. Ristroph and J. Zhang. “Anomalous hydrodynamic drafting of interacting flapping flags”. In: *Physical Review Letters* 101.19 (2008), p. 194502 (cit. on p. 37).

[208] I. Borazjani and F. Sotiropoulos. “Numerical investigation of the hydrodynamics of carangiform swimming in the transitional and inertial flow regimes”. In: *Journal of Experimental Biology* 211.10 (2008), pp. 1541–1558 (cit. on p. 37).

[209] M. Bergmann and A. Iollo. “Modeling and simulation of fish-like swimming”. In: *Journal of Computational Physics* 230.2 (2011), pp. 329–348 (cit. on p. 37).

[210] A.A. Tchieu, E. Kanso, and P.K. Newton. “The finite-dipole dynamical system”. In: *Proceedings of the Royal Society A: Mathematical, Physical and Engineering Science* 468.3006–3026 (2012) (cit. on p. 37).

[211] B.M. Boschitsch, P.A. Dewey, and A.J. Smits. "Propulsive performance of unsteady tandem hydrofoils in an in-line configuration". In: *Physics of Fluids* 26.5 (2014), p. 051901 (cit. on p. 37).

[212] M. Gazzola, B. Hejazialhosseini, and P. Koumoutsakos. "Reinforcement learning and wavelet adapted vortex methods for simulations of self-propelled swimmers". In: *SIAM Journal on Scientific Computing* 36.3 (2014), B622–B639. DOI: 10.1137/130943078 (cit. on pp. 37, 49).

[213] M. Gazzola, A.A. Tchieu, D. Alexeev, A. de Brauer, and P. Koumoutsakos. "Learning to school in the presence of hydrodynamic interactions". In: *Journal of Fluid Mechanics* 789 (2015), pp. 726–749. DOI: 10.1017/jfm.2015.686 (cit. on p. 37).

[214] J. Eldredge. "A reconciliation of viscous and inviscid approaches to computing locomotion of deforming bodies". In: *Experimental Mechanics* 50 (2010). 10.1007/s11340-009-9275-0, pp. 1349–1353 (cit. on p. 37).

[215] M. Gazzola, C. Mimeau, A.A. Tchieu, and P. Koumoutsakos. "Flow mediated interactions between two cylinders at finite Re numbers". In: *Physics of Fluids* 24.4 (2012), p. 043103. DOI: 10.1063/1.4704195 (cit. on pp. 37–39).

[216] Zhonglu Lin, Dongfang Liang, and Ming Zhao. "Effects of Damping on Flow-Mediated Interaction Between Two Cylinders". In: *Journal of Fluids Engineering* 140.9 (2018), p. 091106 (cit. on pp. 37, 40).

[217] Ronald L Panton. *Incompressible flow*. John Wiley & Sons, 2006 (cit. on p. 39).

[218] JCR Hunt, CJ Abell, JA Peterka, and H Woo. "Kinematical studies of the flows around free or surface-mounted obstacles; applying topology to flow visualization". In: *Journal of Fluid Mechanics* 86.1 (1978), pp. 179–200 (cit. on p. 46).

[219] Anthony E Perry and Min S Chong. "A description of eddying motions and flow patterns using critical-point concepts". In: *Annual Review of Fluid Mechanics* 19.1 (1987), pp. 125–155 (cit. on p. 46).

[220] Tejaswin Parthasarathy and Mattia Gazzola. "Scaling arguments for flows induced by oscillating cylinders". In: *APS Meeting Abstracts*. 2017 (cit. on p. 49).

[221] W.M. van Rees, M. Gazzola, and P. Koumoutsakos. "Optimal shapes for anguilliform swimmers at intermediate Reynolds numbers". In: *Journal of Fluid Mechanics* 722 (2013), R3. DOI: 10.1017/jfm.2013.157 (cit. on p. 49).

[222] Wim M. van Rees, Mattia Gazzola, and Petros Koumoutsakos. “Optimal morphokinematics for undulatory swimmers at intermediate Reynolds numbers”. In: *Journal of Fluid Mechanics* 775 (2015), pp. 178–188 (cit. on p. 49).

[223] Vedant Dubey. “A self corrective vortex fluxing method for viscous fluid structure interaction problems”. PhD thesis. 2018 (cit. on p. 50).

[224] Alexandre Munnier and Bruno Pinçon. “Locomotion of articulated bodies in an ideal fluid: 2d model with buoyancy, circulation and collisions”. In: *Mathematical Models and Methods in Applied Sciences* 20.10 (2010), pp. 1899–1940 (cit. on pp. 51, 53–55).

[225] Horace Lamb. *Hydrodynamics*. Cambridge university press, 1932 (cit. on pp. 52, 54).

[226] Kendall E Atkinson. “The numerical solution of Fredholm integral equations of the second kind”. In: *SIAM Journal on Numerical Analysis* 4.3 (1967), pp. 337–348 (cit. on pp. 54, 55).

[227] D. Rossinelli, L. Chatagny, and Petros Koumoutsakos. “Evolutionary optimization of scalar transport in cylinder arrays on multiGPU/multicore architectures”. In: *Evolutionary and Deterministic Methods for Design, Optimization and Control* (2011), pp. 773–784 (cit. on p. 57).